1996

Amorphization and Fracture in Silicon Selenium(2) Nanowires: Molecular-Dynamics Simulations on Parallel Computer Architectures.

Wei Li
Louisiana State University and Agricultural & Mechanical College

INFORMATION TO USERS

This manuscript has been reproduced from the microfilm master. UMI films the text directly from the original or copy submitted. Thus, some thesis and dissertation copies are in typewriter face, while others may be from any type of computer printer.

The quality of this reproduction is dependent upon the quality of the copy submitted. Broken or indistinct print, colored or poor quality illustrations and photographs, print bleedthrough, substandard margins, and improper alignment can adversely affect reproduction.

In the unlikely event that the author did not send UMI a complete manuscript and there are missing pages, these will be noted. Also, if unauthorized copyright material had to be removed, a note will indicate the deletion.

Oversize materials (e.g., maps, drawings, charts) are reproduced by sectioning the original, beginning at the upper left-hand corner and continuing from left to right in equal sections with small overlaps. Each original is also photographed in one exposure and is included in reduced form at the back of the book.

Photographs included in the original manuscript have been reproduced xerographically in this copy. Higher quality 6" x 9" black and white photographic prints are available for any photographs or illustrations appearing in this copy for an additional charge. Contact UMI directly to order.

UMI

A Bell & Howell Information Company
300 North Zeeb Road, Ann Arbor MI 48106-1346 USA
313/761-4700 800/521-0600

AMORPHIZATION AND FRACTURE IN $SiSe_2$ NANOWIRES: MOLECULAR-DYNAMICS SIMULATIONS ON PARALLEL COMPUTER ARCHITECTURES

A Dissertation

Submitted to the Graduate Faculty of the
Louisiana State University and
Agricultural and Mechanical College
in partial fulfillment of the
requirements for the degree of
Doctor of Philosophy

in

The Department of Physics and Astronomy

by
Wei Li
B.S., Beijing University, 1983
M.S., Institute of Biophysics, Academia Sinica, 1986
May 1996

DEDICATION

To Kenny, Daniel,

and my parents

ACKNOWLEDGMENTS

I would like to express my gratitude to my advisors, Drs. Rajiv K. Kalia and Priya Vashishta. They have been very supportive and encouraging during my time as a graduate student. They have taught me many things from basic skills in designing computer programs, seeking the essence of physics from simulation results, to writing qualified scientific papers, and making professional representations. Much of the work contained in this thesis is based on the application of molecular-dynamics (MD) simulation technique which I have learned from Dr. Kalia for the first time. His breadth of knowledge and rigorous research attitude have been a great benefit for me to work in this field. Dr. Vashishta introduced me the idea of constructing $SiSe_2$ nanowires using MD technique and encouraged me to study crack propagation and fracture in these systems. His wide experiences, professional guidance and great patience have led me to finish this thesis.

I am indebted to my colleagues and friends Drs. Aiichiro Nakano, Jinghan Wang, Kenji Tsuruta and Jin Yu for many helpful discussions, suggestions, and continued interest. I appreciate their time and effort in reading the first draft of this dissertation. I would like to thank the professors I have worked with, Drs. Donald Greenwell, Simon de Leeuw, José Pidro Rino and Ingvar Ebbsjö, for many interesting and informative discussions. My thank also goes to Timothy Campbell for reading part of this dissertation and providing interesting references. I would also like to thank other members and friends of the Concurrent Computing Laboratory for Materials Simulations (CCLMS), Drs. Martina E. Bachlechner and Guang-lin Zhao, Andrey Omeltchenko, Alok Chatterjee, Haiping Yan, and Gonzalo Gutierrez for their supports and friendship.

I wish to thank Professors Joel E. Tohline, Richard Kurtz, John Tyler, and Alexandar Skavantzos for serving on my thesis committee.

I would like to acknowledge the financial support I have received from the Teaching Assistantship from the Department of Physics and Astronomy, Research Assistantship from CCLMS, and NSF Graduate Research Traineeship (Grant No. GER9355007). Part of the work is done on Touchstone Delta machine at Caltech. The simulations of $SiSe_2$ nanowires are performed on the computational facilities in the CCLMS (see Appendix A) which are supported by the Louisiana Education Quality Support Fund (LEQSF).

I thank the systems managers Monika Lee and Hortensia Valdes for many helpful assistance. Many thanks also go to all the current and former secretaries and staff members: Julie Doncet, Arnell Johnson, Karla Lockwood, Beverly Rodriguez, Karen Richard, Cathy Mixon, Karen Cashio, Ophelia Dudley, and our previous business manager and now the Assistant Dean of the Graduate School Jim Fernandez for their assistance in many ways.

I am deeply indebted to my parents for their love, understanding, and patience throughout the years. Without their continuous support, this Ph.D. thesis project would not be possible. Most of all, I wish to express my deep appreciation to my husband Kenny and our son Daniel. Their selfless love and indispensable support have been constant sources of inspiration for me to go through this long and hard journey.

TABLE OF CONTENTS

LIST OF TABLES

LIST OF FIGURES

ABSTRACT

The primary goal of this dissertation is to investigate the structural and mechanical properties and dynamical fracture in $SiSe_2$ nanowires using the molecular-dynamics (MD) simulation technique. The present work is the first study of $SiSe_2$ nanowires.

Large-scale simulations reported in this thesis are carried out with parallel multiresolution schemes for the long-range Coulomb and the three-body covalent potentials. The multiresolution scheme reduces the computational complexity from $O(N^2)$ to O(N).

Using an effective interatomic potential containing both 2- and 3-body interactions, MD simulations are performed for $SiSe_2$ nanowires composed of finite (1-64) number of chains. Under small uniaxial strain, the nanowires are found to be highly crystalline and they remain in the elastic deformation regime. The macroscopic mechanical behavior is determined by intra-chain interactions. Under large uniaxial strain, we find local amorphization followed by fracture of nanowires. Initially broken edge-sharing bonds are found in the chains at the outermost layer. These broken bonds induce cross-linking among the neighboring chains and lead to the presence of corner-sharing tetrahedra. Results for the time evolution of amorphization and crack initiation and propagation are presented.

CHAPTER 1

INTRODUCTION

1.1 Background and Motivation

Understanding the microscopic processes which control fracture of materials is one of the most challenging problems in material science. The key issues in dynamical fracture relate to: 1) initiation of cracks; 2) propagation of cracks; 3) roughness of fractured surfaces; and 4) driving mechanism for fracture [1]. A great deal of recent theoretical and experimental research effort has been devoted to addressing these issues. Marder has studied instability in lattice fracture and dynamics of crack propagation [2-4]. First-principles studies of large scale defects and their implications for brittle-ductile transition have been carried out by Kaxiras and collaborators [5, 6]. Recent experiments have played a key role in our understanding of the dynamical fracture at the atomistic level [7-11]. Although detailed experimental studies have been carried out to determine dislocation emission from crack tips, crack branching, indentation fracture, and brittle-ductile transition, little attention has been paid to the phenomena of amorphization in materials prior to fracture.

There are two kinds of amorphization processes: solid-state and quench-melt amorphization. Solid-state amorphization is conceptually different from quench-melt amorphization [12, 13]. The material obtained by fast cooling of a liquid is expected to reflect the disorder in the liquid phase. The resulting amorphous solid is isotropic like the liquid from which it is formed. Solid-state amorphization, on the other hand, is a direct crystalline-to-amorphous transformation. Samples produced in this fashion have been found to have x-ray-diffraction patterns and vibrational spectra which are typical of amorphous structures. The nature of the amorphous state (local order, etc.) obtained

through a solid-state transformation is still a controversial issue. A number of experimental results have been interpreted as evidence that anisotropic structures have been found in the pressure-induced amorphous form of $AlPO_4$ and SiO_2 (α-quartz) [14-16]. MD simulations also reveal that the amorphous states depend on the experimental history of the transformation, which is not structurally related to melting [17-19]. However, other studies support the universal nature of the amorphous phase in the sense that it lacks long-range order and is isotropic [20].

Over the past few years, problems associated with dynamical fracture have been studied extensively with computer simulations involving the molecular dynamics (MD) method [21-24]. From conventional studies of simple defects to large-scale simulations of fracture, the MD method has made great contributions in bridging the gap between theory and experiment. With an increase in computing power and the development of advanced interatomic potential functions, molecular-dynamics simulations have become a unique research tool for physicists, chemists, materials scientists and engineers. MD method is totally deterministic and most suitable for classical many-body problems. Following the time evolution of a classical many-body system, MD offers a unique way to study both static and dynamic properties simultaneously. In the MD approach, phase space trajectories (time-dependent positions and momenta of particles) of a system are generated by direct numerical integration of the Newton's equations of motion [25-27]. The essential input to MD simulation is a specific interparticle interaction which is commonly expressed as a combination of one-body, two-body, three-body potential, etc. These potentials are often constructed on the basis of experimental information. The basic output of a MD simulation is the phase space trajectories of the system, from which a variety of physical properties – structural, thermodynamical, mechanical, vibrational, and transport properties – can be calculated.

Many advances have been made to augment the scope of MD simulations. These include constant-temperature simulations to study isothermal processes [28, 29] and constant-pressure/stress simulations to investigate isobaric phenomena [30-34] and structural transformations in solids [35]. Pioneering atomistic simulations of crack growth were performed by Ashurst et al. [36] and Sieradzki et al. [37, 38] on 2D lattices. Finite-temperature MD computations were carried out to study the behavior of materials under strain [39, 40]. A transition from brittle to ductile fracture was observed in α-Fe by Cheung and Yip [41]. Ochoa et al. [42] examined the effects of applied uniaxial strain rates on brittle failure of amorphous and crystalline SiO_2. Abraham et al. observed crack branching in simulations of crack motion for a 2-D system [43]. Belak et al. [44] investigated nanoscale indentation of metallic and ceramic surfaces using the MD method.

Molecular-dynamics simulations of complex phenomena like fracture require large system sizes (with the number of particles ranging from $N=10^5$ to 10^7) and long simulation times. The preparation of a well-thermalized MD configuration requires 10^4-10^6 time steps [45]. (Typically, a MD time step is 10^{-15} sec.) Clearly, it is not feasible to simulate large complex systems over long intervals of time on sequential machines. MD simulations for real systems require the use of massively parallel computer architectures [46]. Recently, Holian et al. implemented MD on a parallel machine to study brittle and ductile behavior [47-49]. Large-scale parallel MD simulations have also been performed to investigate crack propagation in a-Si_3N_4 films [50].

Over the years, efforts to parallelize MD scheme have focused on systems with short-range interparticle interactions. The calculation of long-range forces remains as one of the most prohibitive computational problems. The conventional evaluation of long-range interaction for an N particle system requires $O(N^2)$ operations. Recent research efforts have significantly reduced the computational complexity of the long

range interaction. For example, the Fast-Multipole-Method (FMM) involves only O(N) operations [51]. In this dissertation, we will describe the implementation of the FMM on a distributed-memory multiple instruction and multiple data (MIMD) machine.

Over the last decade, a great deal of research has focused on nanostructured materials. These materials are used in a variety of applications including turbine blade coatings, thin film devices, membranes, catalysts, sensors, biological and magnetic recording media, and so on. Various fabrication techniques have been developed over the past few years to produce nanostructures. A special filling mechanism is used to fill carbon nanotubes with metals and metallic compounds to obtain nanocomposite materials [52]. Nuclear track etching is applied to make nanosized pores. This technique is combined with electrochemical deposition to produce arrays of metallic nanowires [53]. Electron beam lithography has been used to define nanometer scale features on GaAs/AlGaAs heterostructure surfaces [54]. Experiments are also carried out to study electrical, mechanical, and optical properties of nanostructures [55, 56].

In the present work, we are interested in $SiSe_2$ nanowires. $SiSe_2$ is an important chalcogenide material. Crystalline $SiSe_2$ consists exclusively of edge-sharing tetrahedra, which lead to a one-dimensional chain structure [57]. Therefore, a nanowire containing a finite number of non-intersecting chains can be readily obtained theoretically from a crystalline structure, although $SiSe_2$ nanowires have not yet been experimentally synthesized. $SiSe_2$ is of great technological importance: because of fast ion conductivity of Ag and related ions in it, silver doped amorphous $SiSe_2$ is recognized as one of the basic solid electrolytes for advanced high-energy electrochemical cells [58].

The structure and vibrational spectra of crystalline and amorphous $SiSe_2$ have been well studied both theoretically and experimentally. The presence of edge-sharing $Si(Se_{1/2})_4$ tetrahedral units in $SiSe_2$ glass was first revealed by Tenhover et al. through Raman spectroscopy [59]. Additional experimental evidence was provided by more

detailed Raman and infrared measurements [60-62]. Griffiths et al. were the first to propose cross-linking of chain segments leading to corner-sharing $Si(Se_{1/2})_4$ tetrahedral units in $SiSe_2$ glass [63]. The assumption of random packing of linear or coiled isolated chains does not produce a satisfactory model of the amorphous state. The amorphous Si_xSe_{1-x} has been extensively investigated by Johnson, Susman and co-workers [64-69]. Structural correlations have also been determined from magic-angle spinning NMR by Tenhover and his coworkers [62]. As far as theoretical models are concerned [70, 71], Gladden et al. have used computer-generated configurations based on crystalline seeds to study the structure of g-$SiSe_2$ [72-74]. The nature of tetrahedral molecular fragments in glassy $SiSe_2$ has been investigated by MD simulations [75-77]. It is reported that edge-sharing tetrahedra are the building blocks of chain-like-molecular fragments of length 1-1.5 nm.

Research has also been carried out to investigate the elastic and thermodynamic properties of $SiSe_2$. The Brillouin scattering technique has been used to determine the phonon spectra of Si_xSe_{1-x} glasses over the composition range of 0.06 to 0.42 [78]. Enthalpy of formation of solid $SiSe_2$ has also been evaluated [79]. The Fluorine-combustion calorimetry technique has been used to obtain thermodynamic information on $SiSe_2$ glasses [80]. Recently, two new crystalline polymorphs of $SiSe_2$ have been synthesized and investigated by Raman and NMR spectroscopies [81]. These new polymorphs contain corner-sharing tetrahedra as well. However, to the best of our knowledge, very little information is available concerning the mechanical properties of this very interesting material.

1.2 Objectives

The goals of this dissertation are two-fold: (1) to design and implement a parallel MD algorithm for the long-range Coulomb interaction; and (2) to investigate the dynamical fracture in $SiSe_2$ nanowires using MD simulations. In the thesis, we present:

- Performance of FMM on distributed memory MIMD machines;
- Structural stability of $SiSe_2$ nanowires;
- Stress-strain behavior and critical strain for these nanowires;
- Flow initiation and dynamics of fracture in these nanowires.

This dissertation is organized as follows. We will start with a review of MD simulation techniques in Chapter 2; the computational techniques for force calculations are also discussed in this chapter. In Chapter 3, we present the implementation of the Fast Multipole Method on Intel's 512-node Touchstone Delta machine at Caltech. MD simulations of structural and mechanical properties of $SiSe_2$ nanowires under small uniaxial strain are described in Chapter 4. In Chapter 5, we present results for amorphization and dynamical fracture in $SiSe_2$ nanowires. Chapter 6 contains concluding remarks and a brief description of future work.

CHAPTER 2

MOLECULAR-DYNAMICS SIMULATION

2.1 Formalism of Molecular Dynamics

Molecular-dynamics is a simulation technique to compute the phase-space trajectories of particles. For an N-particle system, the phase-space is a 6N-dimensional hyperspace of positions and momenta of the particles. Conventional MD simulations are carried out in the microcanonical (NVE) ensemble. It is also possible to perform MD simulations in a canonical (NVT) ensemble where fictitious variables are introduced to allow thermal coupling to a heat reservoir. In simulations involving external stress/pressure, an isoenthalpic-isotension (HtN) ensemble and an isothermal-isobaric (NPT) ensemble are used. In the following sections, we will review the basic formalism of MD simulations in these ensembles.

2.1.1 Molecular-Dynamics in Microcanonical (NVE) Ensemble

For a system of N particles interacting via a potential $\mathcal{V}$, the Euler-Lagrangian equations are

$$\frac{d}{dt}\left(\frac{\partial \mathcal{L}}{\partial \dot{q}_k}\right) - \left(\frac{\partial \mathcal{L}}{\partial q_k}\right) = 0 \ , \tag{2.1}$$

where

$$\mathcal{L} = \mathcal{K} - \mathcal{V} \ , \tag{2.2}$$

$$\mathcal{K} = \sum_{i=1}^{N} \frac{m_i}{2} \dot{\vec{r}}_i^{\,2} \ , \tag{2.3}$$

$$\mathcal{V} = \sum_{i=1}^{N} v_1(\vec{r}_i) + \sum_{j>i}^{N} v_2(\vec{r}_i, \vec{r}_j) + \sum_{k>j>i}^{N} v_3(\vec{r}_i, \vec{r}_j, \vec{r}_k) + \ldots \ . \tag{2.4}$$

In Eq.(2.4), v_1, v_2 and v_3 represent one-body (external field), two-body and three-body interactions, respectively. Substituting (2.2)-(2.4) into (2.1), one obtains

$$m_i \ddot{\vec{r}}_i = -\nabla_{\vec{r}_i} \mathcal{V} , \qquad i=1, \ldots, N. \tag{2.5}$$

When the forces among atoms are conservative, the Hamiltonian is a constant of the motion. In the case of a microcanonical ensemble, the total energy is conserved:

$$\mathcal{H} = \mathcal{K} + \mathcal{V} = E. \tag{2.6}$$

2.1.2 Molecular-Dynamics in Canonical (NVT) Ensemble

To treat the dynamics of a system in contact with a heat reservoir, an additional degree of freedom, f, is introduced [29]. In this case, the Lagrangian is taken to be

$$\mathcal{L} = \sum_{i=1}^{N} \frac{m_i}{2} f^2 \dot{\vec{r}}_i^2 - \mathcal{V} + \frac{Q}{2}\dot{f}^2 - (3N+1)k_B T_{eq} \ln f , \tag{2.7}$$

where Q is the fictitious 'mass' of the heat reservoir (in unit of energy·(time)^2), T_{eq} is the desired equilibrium temperature, and k_B is Boltzmann's constant. The equations of motion for $\{\vec{r}_i\}$ and f are

$$m_i \ddot{\vec{r}}_i = -\frac{1}{f^2}\nabla_{\vec{r}_i}\mathcal{V} - 2m_i \dot{\vec{r}}_i \frac{\dot{f}}{f}, \qquad i=1, \ldots, N, \tag{2.8}$$

$$Q\ddot{f} = \sum_{i=1}^{N} m_i f \dot{\vec{r}}_i^2 - \frac{(3N+1)k_B T_{eq}}{f}. \tag{2.9}$$

By specifying a temperature, T_{eq}, the thermal coupling between particles and the heat reservoir will bring the total system to thermal equilibrium. The quantity

$$\mathcal{H} = \sum_{i=1}^{N} \frac{m_i}{2} f^2 \dot{\vec{r}}_i^2 + \mathcal{V} + \frac{Q}{2}\dot{f}^2 + (3N+1)k_B T_{eq} \ln f \tag{2.10}$$

is a constant of motion.

2.1.3 Molecular-Dynamics in Isoenthalpic-Isotension (HtN) Ensemble

To study phase transformations or other physical phenomena involving a change of volume, it is essential that the simulation box changes with time. Parrinello and

Rahman modified the MD technique to allow for variations in the shape of the MD cell at constant stress and/or hydrostatic pressure [35, 82-89]. They introduced a 3×3 matrix, **h**, included in the Lagrangian. The matrix **h** defines the shape of simulation box and is formed by the vectors ($\vec{a}$, $\vec{b}$, $\vec{c}$) that span the edges of the simulation box, see Figure 2.1. The 3-D Cartesian coordinate, $\vec{r}_i$, of the *i* th particle is related to its dimensionless coordinate, $\vec{s}_i$, through the relation

$$\vec{r}_i = \mathbf{h}\,\vec{s}_i, \qquad i = 1, 2, ..., N. \tag{2.11}$$

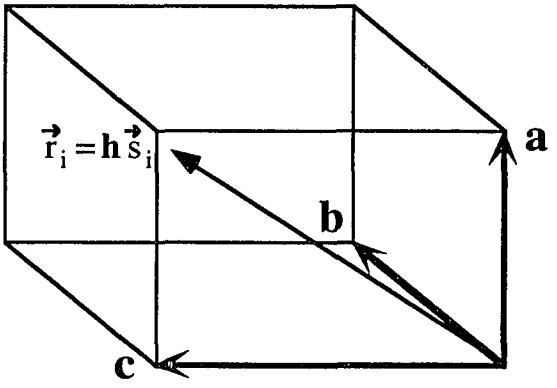

Figure 2.1 A MD box is formed by three vectors, $\vec{a}$, $\vec{b}$ and $\vec{c}$. The coordinates of particles are scaled by $\mathbf{h} = (\vec{a}, \vec{b}, \vec{c})$.

The Lagrangian of the system is taken to be:

$$\mathcal{L} = \sum_{i=1}^{N} \frac{m_i}{2} f^2 \dot{\vec{s}}_i' \mathbf{G}\, \dot{\vec{s}}_i - \mathcal{V} + \frac{Q}{2}\dot{f}^2 - (3N+1)k_B T_{eq} \ln f$$

$$+ \frac{W}{2} Tr(\dot{\mathbf{h}}'\dot{\mathbf{h}}) - V_0 Tr(\mathbf{t}\boldsymbol{\varepsilon}), \tag{2.12}$$

where

$$\mathbf{G} = \mathbf{h}'\mathbf{h}, \tag{2.13}$$

$$\boldsymbol{\varepsilon} = \frac{1}{2}(\mathbf{h}_0'^{-1}\mathbf{G}\mathbf{h}_0^{-1} - \mathbf{I}). \tag{2.14}$$

In the above equations, $\mathbf{h}'$ is the transpose of $\mathbf{h}$, $\boldsymbol{\varepsilon}$ is the strain tensor, $\mathbf{t}$ is an external stress tensor, W is the 'mass' of the simulation box (in units of mass), and V_0 is the reference volume of the simulation box:

$$V_0 = \det(\mathbf{h}_0). \tag{2.15}$$

The equations of motion for the Lagrangian in Eq.(2.12) are:

$$m_i \ddot{\vec{s}}_i = -\frac{1}{f^2}\mathbf{h}'^{-1}\nabla_{\vec{r}_i}\mathcal{V} - 2m_i\dot{\vec{s}}_i\frac{\dot{f}}{f} - m_i\mathbf{G}^{-1}\dot{\mathbf{G}}\dot{\vec{s}}_i, \qquad i=1,\ldots, N, \tag{2.16}$$

$$Q\ddot{f} = \sum_{i=1}^{N} m_i f \dot{\vec{s}}_i'\mathbf{G}\,\dot{\vec{s}}_i - \frac{(3N+1)k_B T_{eq}}{f}, \tag{2.17}$$

$$W\ddot{\mathbf{h}} = \mathcal{P}\mathbf{A} - \mathbf{h}\Gamma, \tag{2.18}$$

where

$$\mathcal{P} = \frac{1}{V}\sum_{i=1}^{N}[m_i f^2 \mathbf{h}\dot{\vec{s}}_i\dot{\vec{s}}_i'\mathbf{h}' - (\nabla_{\vec{r}_i}\mathcal{V})\vec{s}_i'\mathbf{h}'], \tag{2.19}$$

$$\mathbf{A} = V\mathbf{h}'^{-1}, \tag{2.20}$$

$$\Gamma = V_0\mathbf{h}_0^{-1}\mathbf{t}\mathbf{h}_0'^{-1}. \tag{2.21}$$

In these equations, $\mathcal{P}$ is an "instantaneous" internal stress tensor, $\mathbf{A}$ is the area tensor, Γ is a matrix related to the external stress, and V is the volume of the system $V = \det(\mathbf{h})$.

In a constant-stress ensemble the constant of motion is:

$$\mathcal{H} = \sum_{i=1}^{N}\frac{m_i}{2}f^2\dot{\vec{s}}_i'\mathbf{G}\,\dot{\vec{s}}_i + \mathcal{V} + \frac{Q}{2}\dot{f}^2 + (3N+1)k_B T_{eq}\ln f$$

$$+ \frac{W}{2}\mathrm{Tr}(\dot{\mathbf{h}}'\dot{\mathbf{h}}) + V_0\,\mathrm{Tr}(\mathbf{t}\boldsymbol{\varepsilon}). \tag{2.22}$$

2.2 Numerical Solution of Equations of motion

Newton's equations of motion are second-order, non-linear, coupled, ordinary differential equations. To solve them numerically, one needs to specify the initial

conditions as well as the boundary conditions. The basic idea behind the MD technique is: given positions and velocities at time t, integrate equations of motion to obtain new positions and velocities at time $t+\Delta t$. The central part of any MD program is the integration algorithm. (In general, the actual time one spends on integrating the equations of motion is negligible compared with the time it takes to compute the interatomic forces.) In the next subsections, we will discuss initial and boundary conditions for MD simulations. Then we introduce the 'Velocity Verlet' integration algorithm, followed by a discussion on force calculation.

2.2.1 Initial and Boundary Conditions

The initial positions and velocities can be chosen in a variety of ways. For solids, it is customary to initially place the particles at the equilibrium lattice positions. The simulation box is taken to be a multiple of unit cells. For liquids and glasses, the initial positions of particles and the MD box can be chosen in the same way. The system is then gradually heated to the desired temperature and the box variables are scaled to obtain the correct density of liquid or glass.

Usually the initial velocities are chosen randomly from the Maxwell-Boltzmann distribution. Initial velocities are scaled to obtain the desired temperature. The net linear and angular momenta are set equal to zero.

Bulk systems are simulated with the application of periodic boundary conditions (pbc). Pbc remove the surface effects in a mathematically well-defined manner. Under pbc, the simulation box of length L is taken as the basic unit. The whole space is filled by periodically repeating this basic unit in space. Each image cell contains N particles with the same relative positions and velocities as the particles in the central cell. When a particle leaves from one of the faces of the central cell, an image of that particle enters through the opposite face, see Figure 2.2.

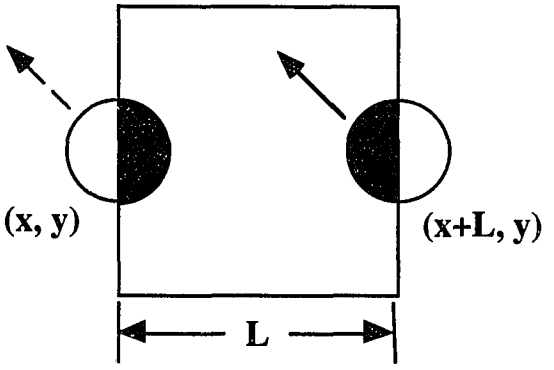

Figure 2.2 Periodic boundary conditions.

In principle, each particle interacts with all other particles in the same cell and with all the image particles. If the range of the forces is smaller than L/2, we only need to consider interactions with the closest images. In the case of long-range forces, we need to take into account interactions with all the images.

2.2.2 Integration algorithms

There are many integration algorithms for Newton's equations of motion. All of them convert the differential equations into finite-difference equations. The commonly used algorithms are Gear's predictor-corrector method; Verlet's algorithms; Beeman algorithms, etc..

Recently, Tuckerman and co-workers have generated reversible MD integrators from the Trotter factorization of the Liouville propagator [90]. Here we briefly describe their derivation of the Velocity-Verlet algorithm.

In Cartesian coordinates, the Liouville operator L for a system of N particles is

$$iL = \sum_{j=1}^{3N} \left[\dot{p}_j \frac{\partial}{\partial p_j} + \dot{x}_j \frac{\partial}{\partial x_j} \right] = iL_1 + iL_2 \ . \tag{2.23}$$

The corresponding classical propagators are $U(t) = e^{iLt}$, $U_1(t) = e^{iL_1 t}$, and $U_2(t) = e^{iL_2 t}$. These operators are reversible in time in the sense, $U(-t)=U^{-1}(t)$. The states of the

system at time t are given by $\Gamma(t,\Gamma(0)) = U(t)\Gamma(0)$, $\Gamma_1(t,\Gamma(0)) = U_1(t)\Gamma(0)$, and $\Gamma_2(t,\Gamma(0)) = U_2(t)\Gamma(0)$. For a small time interval Δt, the Trotter expansion yields

$$e^{i(L_1 + L_2)\Delta t} = e^{iL_1\Delta t/2}e^{iL_1\Delta t/2}e^{iL_2\Delta t}$$
$$= e^{iL_1\Delta t/2}e^{iL_2\Delta t}e^{iL_1\Delta t/2} + O(\Delta t^3). \tag{2.24}$$

Therefore

$$U(\Delta t) = U_1(\Delta t/2)U_2(\Delta t)U_1(\Delta t/2) + O(\Delta t^3). \tag{2.25}$$

Starting from the state $\Gamma(0)$, the above operator generates a new state at time Δt:

$$\Gamma(\Delta t,\Gamma(0)) = U(\Delta t)\Gamma(0)$$

$$= U_1(\Delta t/2)U_2(\Delta t)U_1(\Delta t/2)\Gamma(0) \tag{2.26}$$

$$= U_1(\Delta t/2)U_2(\Delta t)\Gamma_1(\Delta t/2,\Gamma(0)) \tag{2.27}$$

$$= U_1(\Delta t/2)\Gamma_2[\Delta t,\Gamma_1(\Delta t/2,\Gamma(0))] \tag{2.28}$$

$$= \Gamma_1\{\Delta t/2,\Gamma_2[\Delta t,\Gamma_1(\Delta t/2,\Gamma(0))]\}. \tag{2.29}$$

This general expression is simplified when we substitute L_1 and L_2 into the above equations. For an initial state described by positions and momenta, $\{x_j(0,p_j(0);$ $j=1,2,..,3N\}$, the sequence of operations (2.26)-(2-29) is equivalent to

$$x_j(\Delta t) = x_j(0) + \Delta t\frac{p_j(0)}{m} + \frac{(\Delta t)^2}{2}\frac{\dot{p}_j(0)}{m}, \tag{2.30}$$

$$p_j(\Delta t) = p_j(0) + \frac{\Delta t}{2}\dot{p}_j(0) + \frac{\Delta t}{2}\dot{p}_j(\Delta t). \tag{2.31}$$

There are three steps involved in this algorithm. At first the new positions at time Δt are calculated using Eq.(2.30). Then the velocities (momenta) at mid-step are computed using

$$p_j(\frac{\Delta t}{2}) = p_j(0) + \frac{\Delta t}{2}\dot{p}_j(0). \tag{2.32}$$

The forces $\dot{p}_j(\Delta t)$ at time Δt are then evaluated and finally the velocities (momenta) at Δt are completed from

$$p_j(\Delta t) = p_j(\frac{\Delta t}{2}) + \frac{\Delta t}{2}\dot{p}_j(\Delta t). \tag{2.33}$$

Note that $e^{iL_1\Delta t/2}e^{iL_2\Delta t}e^{iL_1\Delta t/2}$ ensures that the algorithm is time reversible.

2.2.3 Calculation of Interparticle Interactions

The most time-consuming part of any MD simulation is the calculation of forces and potential energy. For a system of N particles, the straightforward evaluation of two-body and three-body interactions require $O(N^2)$ and $O(N^3)$ operations, respectively. In recent years, algorithms have been designed to reduce the computational complexities of two-body and three-body interactions to O(N). In this section, we describe some of these algorithms for short-range and long-range potentials.

2.2.3.1 Two-body vs. Three-body potentials

Monatomic systems with close-packed structures can be described reasonably well by two-body interaction potentials. Usually two-body potentials depend only on the interparticle distances, r_{ij}. In many physical systems, these are short-range interactions. The Lennard-Jones potential is a typical pairwise potential [91]:

$$\mathcal{V}(r) = 4\,\varepsilon\,[(\frac{\sigma}{r})^{12} - (\frac{\sigma}{r})^{6}], \tag{2.34}$$

where ε represents the depth of the potential well and σ is a characteristic length.

For covalent systems, one needs to consider the interactions among triplets of particles. Usually the three-body interaction consists of bond stretching and bond bending terms. As an example, the Stillinger-Weber potential [92] has been used widely for systems such as Si and Ge [93]:

$$\mathcal{V}_3(r_{ij},r_{ik},\theta_{jik}) = \lambda \exp\left[\gamma (r_{ij}-a)^{-1} + \gamma (r_{ik}-a)^{-1}\right] \cdot (\cos\theta_{jik} + \cos\bar{\theta}_{jik})^2. \tag{2.35}$$

The systems we have investigated are of the type AX_2 (SiO_2, $SiSe_2$, and so on). In these systems, there are six different combinations of three-body forces: A-A-A; A-A-X; A-X-A; A-X-X; X-A-X; and X-X-X. The most important terms are A-X-A and X-A-X because A-X is the shortest bond with the strongest attractive energy. We therefore ignore other terms.

Let us consider a general form of three-body interaction:

$$\mathcal{V}_3 = \sum_{i<j<k}^{N} \mathcal{V}^{(3)}_{jik}, \tag{2.36}$$

where

$$\mathcal{V}^{(3)}_{jik} = B_{jik}\, f(r_{ij}, r_{ik})\, (\cos\theta_{jik} - \cos\bar{\theta}_{jik})^2, \qquad r_{ij},r_{ik} < r_{c3}. \tag{2.37}$$

Usually the bond stretching function is symmetric in the sense of $f(r_{ij}, r_{ik}) = f_{ij} \cdot f_{ik}$ and $f_{ij} = f_{ji}$, where $f_{ij} = f(r_{ij})$. If we consider only the terms A-X-A and X-A-X, then (2.36) can be rewritten as

$$\begin{aligned}\mathcal{V}_3 &= \sum_{i=1}^{N_A}\sum_{j=i+1}^{N_A}\sum_{k=1}^{N_X} \mathcal{V}^{(3)}_{A-X-A}(i,k,j) + \sum_{i=1}^{N_A}\sum_{j=1}^{N_X}\sum_{k=j+1}^{N_X} \mathcal{V}^{(3)}_{X-A-X}(j,i,k) \\ &= \mathcal{V}_3^A + \mathcal{V}_3^X,\end{aligned} \tag{2.38}$$

where

$$\mathcal{V}_3^A = \frac{1}{2}B_A \sum_{k=1}^{N_X}\sum_{i=1}^{N_A}\sum_{j=1}^{N_A} \mathcal{V}^{(3)}_{A-X-A}(i,k,j) - \frac{1}{2}B_A \sum_{k=1}^{N_X}\sum_{i=1}^{N_A} f_{ki}^2(1-\alpha_A)^2, \tag{2.39}$$

$$\mathcal{V}_3^X = \frac{1}{2}B_X \sum_{i=1}^{N_A}\sum_{j=1}^{N_X}\sum_{k=1}^{N_X} \mathcal{V}^{(3)}_{X-A-X}(j,i,k) - \frac{1}{2}B_X \sum_{i=1}^{N_A}\sum_{k=1}^{N_X} f_{ki}^2(1-\alpha_B)^2. \tag{2.40}$$

Here we denote α_A=cos $\bar{\theta}_{A-X-A}$ and α_X=cos $\bar{q}_{X-A-X}$. Since we have $\cos\theta_{jik} = \dfrac{\vec{r}_{ij}\cdot\vec{r}_{ik}}{r_{ij}r_{ik}}$ and $\vec{r}_{ij}\cdot\vec{r}_{ik} = x_{ij}x_{ik} + y_{ij}y_{ik} + z_{ij}z_{ik}$, let us define the following notations

$$(x^{(1)}, x^{(2)}, x^{(3)}) = (x, y, z), \tag{2.41}$$

$$g_n(r) = \frac{f(r)}{r^n}, \qquad n = 1, 2, 3, ..., \tag{2.42}$$

$$\bar{g}_1(r) = \frac{1}{r}\frac{df(r)}{dr}, \tag{2.43}$$

$$\bar{\gamma}_n(r) = \frac{1}{r}\frac{dg_n(r)}{dr}, \qquad n = 1, 2, 3, ..., \tag{2.44}$$

$$\varphi_1(\vec{r}_k) = \sum_{i=1}^{N_A} f_{ki}, \qquad k = 1, 2, ..., N_X, \tag{2.45}$$

$$\varphi_2(\vec{r}_k) = \sum_{i=1}^{N_A} (f_{ki})^2, \qquad k = 1, 2, ..., N_X, \tag{2.46}$$

$$C_\nu(\vec{r}_k) = \sum_{i=1}^{N_A} g_1(r_{ki}) x^{(\nu)}_{ki}, \qquad k = 1, 2, ..., N_X, \quad \nu = 1,2 \text{ and } 3 \tag{2.47}$$

$$D_{\nu\nu'}(\vec{r}_k) = \sum_{i=1}^{N_A} g_2(r_{ki}) x^{(\nu)}_{ki} x^{(\nu')}_{ki}, \qquad k = 1, 2, ..., N_X, \quad \nu, \nu' = 1,2 \text{ and } 3. \tag{2.48}$$

In the equations (2.45)-(2.48), if we replace N_X by N_A and exchange k and i, then we will get another set of functions with similar expression. Using these notations, it is easy to write down the following expressions for the three-body potential

$$\mathcal{V}_3^A = \frac{1}{2} B_A \sum_{k=1}^{N_X} \Big\{ \alpha_A^2 [\varphi_1(\vec{r}_k)]^2 - (1-\alpha_A)^2 \varphi_2(\vec{r}_k) - 2\alpha_A \sum_{\nu=1}^{3} [C_\nu(\vec{r}_k)]^2 + \sum_{\nu=1}^{3} \sum_{\nu'=1}^{3} [D_{\nu\nu'}(\vec{r}_k)]^2 \Big\}. \tag{2.49}$$

Again, by replacing k by i and exchanging A and X we can get a similar expression for $\mathcal{V}_3^X$. To calculate forces, we take the first derivative of $\mathcal{V}_3^A$ and $\mathcal{V}_3^X$, the three-body force acting on the *k*th particle of species X is written as

$$F_k = \sum_{i=1}^{N_A} \left[H^{(1)}_{ki,\mu} + H^{(2)}_{ki,\mu} + H^{(3)}_{ki,\mu} + H^{(4)}_{ki,\mu} \right], \qquad k=1, 2, ..., N_X, \tag{2.50}$$

where

$$H^{(1)}_{ki,\mu} = \bar{g}_1(r_{ki}) x^{(\nu)}_{ki} \left[B_A \alpha_A^2 \varphi_1(\vec{r}_k) + B_X \alpha_X^2 \varphi_1(\vec{r}_i) \right], \tag{2.51}$$

$$H^{(2)}_{ki,\mu} = f(r_{ki}) \bar{g}_1(r_{ki}) x^{(\mu)}_{ki} \left[B_A (1-\alpha_A)^2 + B_X (1-\alpha_X)^2 \right], \tag{2.52}$$

$$H^{(3)}_{ki,\mu} = 2\gamma_1(r_{ki}) x^{(\mu)}_{ki} \sum_{\nu=1}^{3} x^{(\nu)}_{ki} \left[B_A \alpha_A C_\nu(\vec{r}_k) - B_X \alpha_X C_\nu(\vec{r}_i) \right]$$

$$+ 2g_1(r_{ki}) \left[B_A \alpha_A C_\mu(\vec{r}_k) - B_X \alpha_X C_\mu(\vec{r}_i) \right], \tag{2.53}$$

and

$$H^{(4)}_{ki,\mu} = \gamma_2(r_{ki}) x^{(\mu)}_{ki} \sum_{\nu,\nu'=1}^{3} x^{(\nu)}_{ki} x^{(\nu')}_{ki} \left[B_A D_{\nu\nu'}(\vec{r}_k) + B_X D_{\nu\nu'}(\vec{r}_i) \right]$$

$$+ 2g_2(r_{ki}) \sum_{\nu=1}^{3} x^{(\nu)}_{ki} \left[B_A D_{\mu\nu}(\vec{r}_k) + B_X D_{\mu\nu}(\vec{r}_i) \right]. \tag{2.54}$$

Similarly, by replacing A by X and exchanging i and k, we can obtain the expression for the three-body force acting on the *i*th particle of species A.

It is easy to see from the above equations that only two-fold summations are involved. Therefore, the evaluation of the three-body potential energy and forces becomes equivalent to that of two-body interactions. Here we would like to point out that the above derivation for the separable three-body force calculation is independent of the form of the bond stretching term f(r). A different expression is given by Nakano et al.[94, 95].

2.2.3.2 Short-Range vs. Long-Range Potentials

For a short-range pair-wise interaction, it is customary to introduce a cutoff r_c beyond which the potential is taken to be zero. In order that the forces and potential energy vanish smoothly at r_c, one uses a shifted potential,

$$\mathcal{V}(r) \Rightarrow \mathcal{V}(r) - \mathcal{V}(r)\Big|_{r=r_c} - (r - r_c) \frac{d\mathcal{V}}{dr}\Big|_{r=r_c}. \tag{2.55}$$

Advances in software technology have resulted in many fast algorithms which employ multiple length scales. The link-cell-list method and the multiple-time-step scheme are the two widely used strategies. They exploit multiple scales in either space or time.

• Link-cell-list method

In a MD simulation, most of the time is spent in computing pair-wise interactions, a process which includes examining the complete set of $O(N^2)$ pairs, identifying a subset of those pairs separated by distances which are less than r_c, and computing the forces for this subset. Pairs of particles separated by distances greater than r_c do not contribute to the forces. The link-cell-list method [26], shown in Figure 2.3, speeds up the calculation significantly.

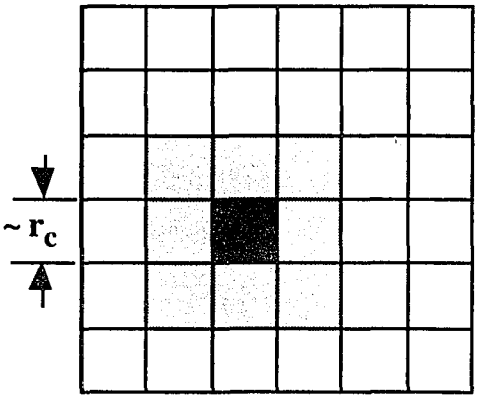

Figure 2.3 Link-cell-list method. The lightly shaded boxes are the nearest neighbor boxes of the darkened box.

In the link-cell-list method, the total volume (L^3) of an N-particle system is divided into n^3 cells of equal volume with edge L/n which is slightly larger than r_c. Particles residing in each cell are identified to construct a linked-cell-list using two integer arrays. The first integer array identifies particles at the top of the list in each cell, and the second integer array links particles belonging to the same cell. Since particles in a given cell will interact only with the particles in the nearest neighbor cells, a neighbor-list is then constructed for

each particle according to the linked-cell-list. At each MD step, forces are calculated within the neighbor-lists. The linked-cell-list and neighbor-list are updated after 10-15 time steps. If the maximum number of neighbors is N_b, then the number of operations will be proportional to N_bN. Therefore the complexity will be O(N).

• Multiple-time-step method

The multiple-time-step (MTS) approach is an efficient way to further speedup the calculation of short-range (with a cutoff radius at r_c) pairwise forces. The MTS method is based on the fact that the farther the distance between particles the slower is the change in forces [26]. Therefore, for different interparticle separations we use different time steps to compute forces. In the MTS method, the force $\vec{F}_i$ acting on the *i* th particle is divided into two groups. The primary force $\vec{F}_i^p$ arises from the interaction with particles lying in a sphere of radius r_a around the *i* th particle. The secondary force $\vec{F}_i^s$ is due to pairwise interactions in the range of $[r_a, r_c]$ around the *i* th particle, see Figure 2.4. Since the secondary force varies much slower than the primary force, we calculate $\vec{F}_i^p$ every MD time step while evaluate $\vec{F}_i^s$ every n steps. At the intermediate steps, $\vec{F}_i^s$ is extrapolated according to the Taylor series expansion,

$$\vec{F}_i^s(t + m\Delta t) = \sum_{l=0}^{l_{max}} \frac{(m\Delta t)^l}{l!} \frac{d^l \vec{F}_i^s(t)}{dt^l}, \qquad m=1, 2, ..., n-1, \tag{2.56}$$

where l_{max} is the cutoff of the Taylor series. For a fixed time step, the efficiency and accuracy of this method are very sensitive to the choice of r_a, n, and l_{max}. In many cases, r_a is slightly larger than $r_c/2$, n varies from 5-15, and l_{max} can be chosen from 2-4, depending on the requirement of energy conservation. With the MTS algorithm, one typically can achieve a 2- to 5-fold speedup.

Long-range forces, such as Columbic interaction, are a serious problem for the computer simulations since their ranges are greater than half the box length. Materials,

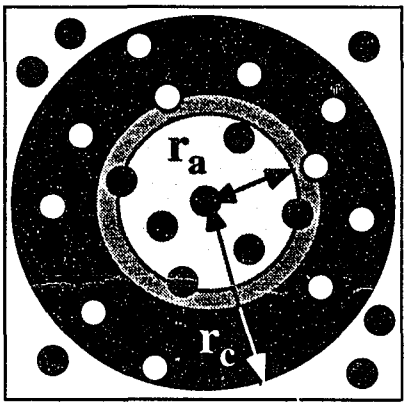

Figure 2.4 Multiple-time-step method. Forces acting on the centered particle are separated into two parts. Forces due to particles inside the sphere of radius r_a are updated every time step. Forces due to particles in the shell $[r_a, r_c]$ are calculated every n steps.

such as plasmas, electrolyte solutions, biological systems, gravitational many-body systems, and certain solids, have long-range interactions. Using periodic boundary conditions, the summation over infinitely repeated image charges must be carried out. Several algorithms have been designed to efficiently calculate long-range forces. The Ewald method is a technique to transform the sum into rapidly convergent sums in real and Fourier spaces. The Fast Multipole Method is based on the rapid decay of the multipole expansion of the Coulomb interaction. These two methods enable one to calculate the long-range interaction efficiently with a specific level of precision. In Chapter 3, we will discuss the implementation of the Fast Multipole Method on parallel architectures.

2.3 Evaluation of Physical Properties

The physical properties of a system can be calculated with the knowledge of the positions and velocities of particles. In the next sections, we will introduce structural properties such as the pair-distribution function g(r) and static structure factor S(q); time

correlation functions such as the velocity auto-correlation function and mean square-displacement; thermodynamical properties such as temperature, pressure, specific heat; and mechanical properties.

2.3.1 Structural Correlation Functions

For a system with two species α and β, the partial pair-distribution functions are defined as [96],

$$\langle n_{\alpha\beta}(r) \rangle = 4\pi r^2 \Delta r \, \rho \, c_\beta \, g_{\alpha\beta}(r), \tag{2.57}$$

where $n_{\alpha\beta}(r)$ denotes the number of particles of species β in the shell between r and r+Δr around a particle of species α. The angular brackets $\langle\,\rangle$ represent the ensemble average and an average over all the particles of species α. ρ is the total number density (= N/V, $N = N_\alpha + N_\beta$) and c_β is the concentration of species β ($= N_\beta/N$). The total pair-distribution function g(r) is defined as

$$g(r) = \sum_{\alpha,\beta} c_\alpha \, c_\beta \, g_{\alpha\beta}(r). \tag{2.58}$$

The static structure factors are related to pair-distribution functions as follows:

$$S_{\alpha\beta}(q) = \delta_{\alpha\beta} + 4\pi\rho(c_\alpha \, c_\beta)^{1/2} \cdot \int_0^R r^2 [\, g_{\alpha\beta}(r) - 1] \frac{\sin(qr)}{qr} \frac{\sin(\pi r / R)}{\pi r / R} \, dr, \tag{2.59}$$

where $\frac{\sin(\pi r / R)}{\pi r / R}$ is a window function. (The cutoff length R is chosen to be half the length of the cubic simulation box). The total static structure factor is given by

$$S(q) = \sum_{\alpha,\beta} (c_\alpha \, c_\beta)^{1/2} \, S_{\alpha\beta}(q). \tag{2.60}$$

The neutron-scattering static structure factor $S_N(q)$ can be obtained from the partial static structure factors by weighting them with coherent neutron-scattering length:

$$S_N(q) = \frac{\sum_{\alpha,\beta} b_\alpha b_\beta (c_\alpha c_\beta)^{1/2}[S_{\alpha\beta}(q) - \delta_{\alpha\beta} + (c_\alpha c_\beta)^{1/2}]}{\left[\sum_\alpha b_\alpha c_\alpha\right]^2}, \qquad (2.61)$$

where b_α denotes the coherent neutron-scattering length of species α.

2.3.2 Time Correlation Functions

The average value of a quantity A can be calculated from the time average,

$$< A > = \overline{A} = \lim_{t \to \infty} \frac{1}{t} \int_0^t dt' A(t'). \qquad (2.62)$$

The time correlation functions are of great interest in computer simulations because they often relate directly to macroscopic transport coefficients. For instance, the velocity autocorrelation function $Z_\alpha(t)$ is related to the constant of self-diffusion D_α through the relation,

$$D_\alpha = \frac{k_B T}{m_\alpha} \int_0^\infty Z_\alpha(t)\, dt, \qquad (2.63)$$

where

$$Z_\alpha(t) = \frac{\langle \vec{v}_i(0) \cdot \vec{v}_i(t) \rangle_\alpha}{\langle v_i^2(0) \rangle_\alpha}, \qquad (2.64)$$

and N_α and m_α are the number of particles and mass, respectively, of species α. Self-diffusion constants can also be calculated from the mean-square displacements,

$$D_\alpha = \lim_{t \to \infty} (\langle r^2 \rangle_\alpha / 6t), \qquad (2.65)$$

where

$$\langle r^2 \rangle_\alpha = \left\langle \frac{1}{N_\alpha} \sum_{j(\alpha)} [\vec{r}_j(t+s) - \vec{r}_j(s)]^2 \right\rangle. \qquad (2.66)$$

Again, the angular brackets $\langle\ \rangle$ represent the ensemble average and an average over all the particles of species α.

2.3.3 Thermodynamic Properties

In the microcanonical ensemble, the temperature of the system is calculated from the mean kinetic energy $< \mathcal{K} >$:

$$< \mathcal{K} >= \frac{3N}{2} k_B T. \tag{2.67}$$

The fluctuations in the kinetic energy K are related to the specific heat of the system [66, 97]:

$$\frac{\langle \delta K^2 \rangle}{\langle K \rangle} = k_B T \left[1 - \frac{3k_B}{2c_v}\right]. \tag{2.68}$$

The mean pressure, P, is calculated from the virial theorem:

$$PV = Nk_B T + \frac{1}{3}\left\langle \sum_{i=1}^{N} \vec{r}_i \cdot \vec{F}_i \right\rangle, \tag{2.69}$$

where N, V, T are number of particles, volume, and mean temperature of the system, respectively; $\vec{r}_i$ is the position vector of the *i* th particle and $\vec{F}_i$ is the total force acting on it due to all the other particles. If the N-body interaction is pairwise, it is more convenient to express the above equation in a form which is explicitly independent of the origin of coordinates:

$$PV = Nk_B T + \frac{1}{3}\left\langle \sum_{j>i}^{N} \vec{r}_{ij} \cdot \vec{F}_{ij} \right\rangle, \tag{2.70}$$

where $\vec{r}_{ij} = \vec{r}_i - \vec{r}_j$, and $\vec{F}_{ij}$ is force between *i*th and *j*th particle. It is essential to use (2.70) in a simulation that employs periodic boundary conditions.

For a solid bar of length L subject to a stretching force F along the length of the bar, we calculate tensile stress and strain as Stress = $\frac{F}{A}$ and Strain = $\frac{\Delta L}{L}$, where A, L, and ΔL represent cross section area, original length, and change of length in the object, respectively. The former is evaluated from the internal energy, $F = \frac{dE}{dL}$. The Young's modulus is obtained from $Y = \frac{L}{A} k$, where $k = \frac{d^2E}{dL^2}$ is the force constant.

CHAPTER 3

IMPLEMENTATION OF MOLECULAR-DYNAMICS SCHEME ON PARALLEL ARCHITECTURES

In many materials, such as semiconductor binary oxides (SiO_2, GeO_2), chalcogenides ($GeSe_2$, $SiSe_2$), III-V semiconductors (GaAs, InI, InSb), and fast-ion conductors (Ag_2S, Ag_2Se), the most dominant interaction is the Coulomb potential arising from charge-transfer effects. Because the Coulomb potential is long ranged, the computation time scales as N^2, where N is the number of particles in the system. For bulk systems, the Coulomb potential is calculated with the Ewald summation method which transforms the conditionally convergent 1/r interaction into rapidly convergent sums in real and Fourier spaces. The computational cost of the Ewald summation grows as $O(N^{3/2})$ [98]. Kalia et al. have designed parallel algorithms to implement this approach on distributed-memory MIMD machines [99].

Recently, several divide-and-conquer schemes have been developed for the long range Coulomb interaction. In these schemes the Coulomb potential is separated into near-field and far-field interactions. The near-field terms are evaluated directly, whereas the far-field interaction is calculated by grouping particles hierarchically. Many different approaches have been developed for the far-field interactions. Appel [100] and Barnes and Hut [101] used a hierarchical tree-based algorithm which reduces the computational complexity to O(NlogN). Fox and coworkers [102] used this algorithm to perform galaxy merger simulation on a distributed-memory parallel machine. Recently this algorithm was implemented on Caltech's Touchstone Delta machine. Simulations involving over 60 million particles were performed [103].

Greengard and Rokhlin have proposed the Fast Multipole Method (FMM) [51, 104-106]. The far-field contribution to the Coulomb interaction is calculated with the

multipole expansion for the Coulomb potential. On sequential machines, the complexity of the FMM is proportional to N. Schmidt and Lee evaluated the performance of this algorithm on a Cray 2 [107]. They also extended it to incorporate Ewald summation for bulk Coulombic systems. Zhao and Johnsson implemented the FMM for three dimensional systems on a Connection machine [108]. The multipole translation theory was further extended [109] and its computational performance was also improved [110, 111] during the last couple of years. Nakano et al. [112] have developed a multiresolution MD algorithm. The calculation of long-range Coulomb interaction in bulk systems is carried out with the reduced cell multipole method.

In this chapter, we describe a parallel implementation of FMM on distributed-memory MIMD machines. In section 3.1, we discuss the domain decomposition scheme. Section 3.2 briefly reviews the FMM formalism. The performance of the FMM on Intel's iPSC/i860 systems is discussed in section 3.3.

3.1 Domain Decomposition Scheme

For a system of N particles, a domain-decomposition algorithm is used to balance the computational load among p processors [46]. In this algorithm, the total system is divided into p subdomains of equal volume. These subdomains are geometrically mapped onto the p processors, see Figure 3.1. Coordinates of particles and other relevant data are assigned to a processor if the coordinates fall into the spatial domain of that processor. Relevant data for particles that move out of a subdomain boundary into a neighboring subdomain are transferred using message-passing technique (by subroutines *csend* and *crecv* on iPSC/860 systems).

The potential energy and forces are computed with the link-cell-list scheme and the multiple-time-step method. Interparticle interactions consist of intranode and internode contributions. For short-range interactions with a cutoff of r_c, the forces

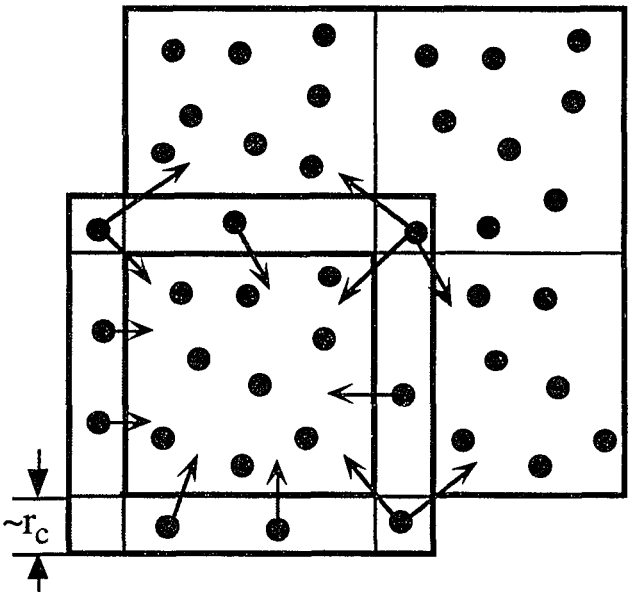

Figure 3.1 Domain decomposition on 4 processors. The arrows indicate the message-passing direction.

calculation in a subdomain requires the coordinates of the boundary particles in the neighboring subdomains. Here we distinguish between the primary- and secondary-boundary particles. In a subdomain, primary boundary particles to the *k*th neighboring (k=1, 2, ..., 26) subdomain are located within a distance $r_a+\Delta$ from the boundary with the *k*th neighbor, where Δ is a small positive value. Similarly, secondary boundary particles are those which are within a distance $r_c+\Delta'$ from the boundary but are not the primary particles, where Δ' is another small distance. Note that a particle can be a boundary particle to several neighboring subdomains. Using multiple-time-step method, the primary boundary particles are copied every step, and the secondary boundary particles are copied after n time steps.

It is important to design an efficient strategy for internode communication. For short-ranged interactions, communications involve 26 neighboring processors. Newton's third law is used to reduce the number of message-passing operations by a

factor of two. Each processor only communicate with its east (or west), left (or right) and upper (or lower) neighboring processors. Coordinates and other relevant data are sent forward to the destination processor. The calculated forces and potential are sent backward to the source processor.

For long-range interactions, we arrange the processors in a ring topology [113], see Figure 3.2.

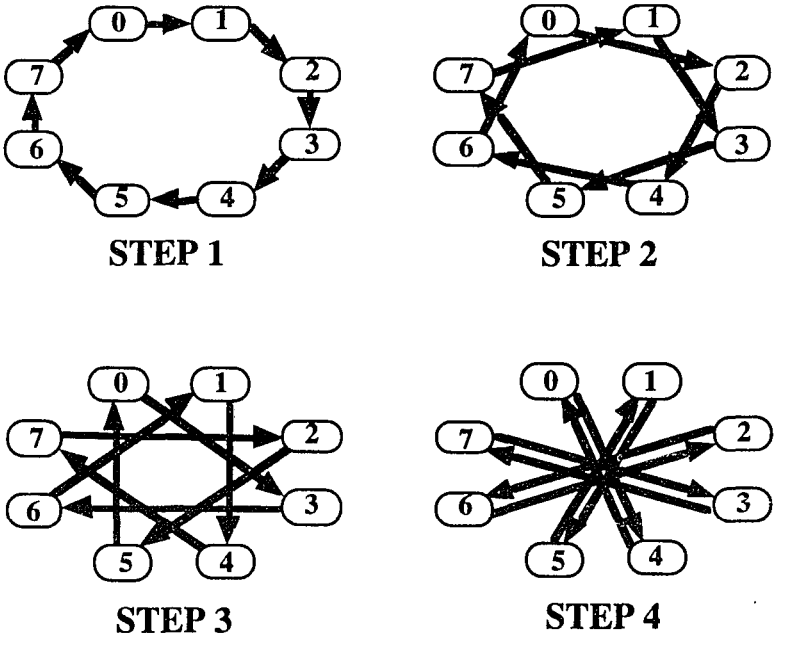

Figure 3.2 Internode communication strategy within eight processors. Arrows indicate the direction of message passing.

First the data from node 0 are sent to node 1, data from node 1 to node 2,..., and data from node p-1 to node 0, synchronously. Then, using the link-cell-list method, the primary and secondary contributions to forces and potential energy are calculated. Node 0 sends back the calculated contributions to node p-1 while receiving the contributions calculated at node 1. Similar message-passing of calculated contributions takes place synchronously at other nodes as well. Next node 0 receives data from node p-2, node 1

from node p-1, ..., and node p-1 from node p-3. The contributions to forces and potential energy are calculated synchronously and the results are sent back to the nodes from which the data had been received. This procedure is continued until all the necessary interactions have been computed. The entire communication process takes p/2 steps.

Parallel algorithms based on domain decomposition schemes have been developed to implement MD simulations on a distributed-memory 8-node Intel iPSC/860 machine. Using the link-cell-list method and the multiple-time-step scheme, the combined approach reduces computation time significantly. The total execution time scales linearly with the number of particles and is inversely proportional to the number of processors [46, 99, 113].

3.2 Fast Multipole Method (FMM)

Fast Multipole Method (FMM) is a divide-and-conquer scheme, in which the system is divided into a hierarchy of cubic subdomains. The interactions between distant charged regions are calculated with a truncated multipole expansion [104]. In spherical coordinates, $\vec{r} = (r, \Omega) = (r, \theta, \varphi)$, the multipole expansion for $1/r$ (when r_i is less than r_j) is

$$\frac{1}{r_{ij}} = \sum_{l=0}^{\infty} \frac{4\pi}{2l+1} \sum_{m=-l}^{l} \frac{r_i^l}{r_j^{(l+1)}} Y_{lm}(\Omega_i)\, Y_{lm}^*(\Omega_j), \tag{3.1}$$

where the terms $Y_{lm}(\Omega)r^l$ are spherical harmonics of degree l. The Coulomb potential experienced by particle i can be written as

$$\Phi_i = q_i \sum_{l=0}^{\infty} \frac{4\pi}{2l+1} \sum_{m=-l}^{l} [\, M_{lm} \frac{1}{r_i^{(l+1)}} + L_{lm}\, r_i^l \,]\, Y_{lm}(\Omega_i), \tag{3.2}$$

where the multipoles M_{lm} are defined as

$$M_{lm} = \sum_{r_j < r_i}^{N} q_j r_j^l Y_{lm}^*(\Omega_j), \tag{3.3}$$

and the local-poles L_{lm} are given by

$$L_{lm} = \sum_{r_j > r_i}^{N} q_j \frac{Y_{lm}^*(\Omega_j)}{r_j^{(l+1)}}. \tag{3.4}$$

The multipole expansion converges outside of a sphere with radius equal to the distance to the farthest charge. The local-pole expansion converges inside a sphere with radius less than the distance to the nearest charge. The rapid decay of the these expansions enables one to calculate the Coulomb interaction efficiently with a specific level of precision. Suppose there are two sets of point charges located in two 3-D boxes. A collection of *m* point charges (q_i, i=1, ..., m) are located inside box A ($\vec{r}_i$, i = 1, ..., m), and a collection of *n* point charges (q_j, j=1, ..., n) are located in box B ($\vec{r}_j$, j = 1, ..., n), see Figure 3.3.

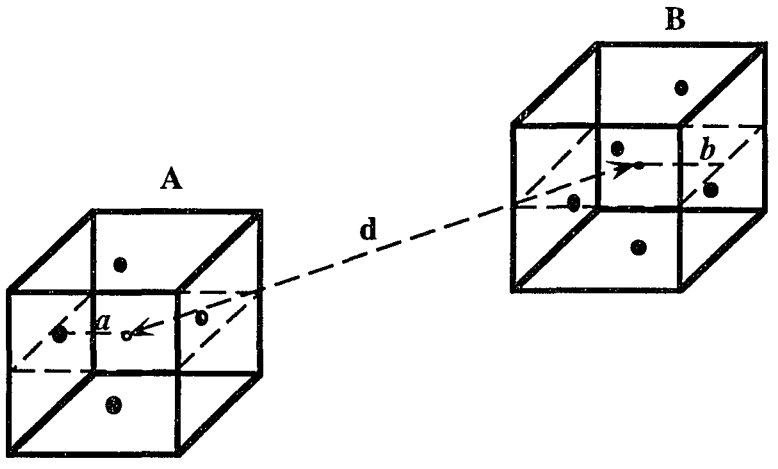

Figure 3.3 Interaction between two 'well-separated' sets of charges. Boxes A and B contain *m* and *n* charged particles, respectively.

In order to calculate the potential at each of the point charges in A due to charges in B, the straightforward evaluation needs mn/2 operations. On the other hand, if we first compute the coefficients of the L_{max} leading terms in multipole expansion, and then compute the potential from Eqs.(3.2)-(3.4), the number of operation is of the order $O(mL_{max}^2 + nL_{max}^2)$. The error in the potential is proportional to $2^{-(L_{max}+1)}$.

In the FMM approach, the potential is calculated through a hierarchical scheme. The entire computational box is divided into 8^L subboxes, where L (an integer) is called the refinement level. Figure 3.4 shows a schematic 2-D computational box with four levels (L=4) of refinement.

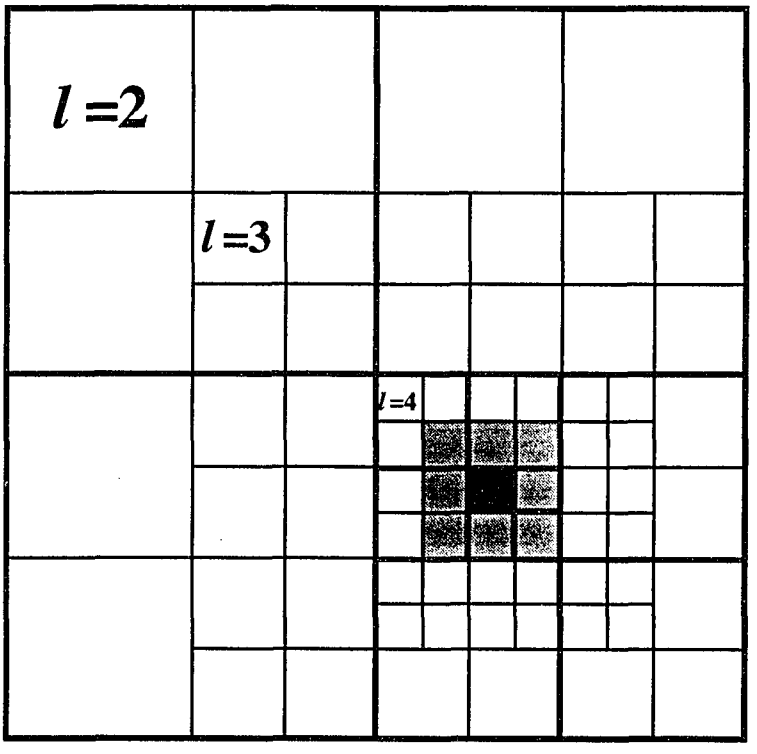

Figure 3.4 A 2-D computational box with 4 levels of refinement. The evaluation point is inside the dark box. The potential due to particles in unshaded boxes is computed with the multipole expansion. The potential due to particles in the shaded boxes is computed directly.

A domain decomposition scheme is used to assign charged particles into each subbox. The multipole expansions of the potential due to charges in each subbox are combined hierarchically. The potential felt by a particle is expressed as a direct interaction with particles in nearby boxes plus a multipole expansion of the field due to particles in all 'well-separated' subboxes. In the FMM method, the near-field contributions are calculated directly using the link-cell-list approach.

The far-field contributions are calculated through three transformations of the multipoles and local-poles. Starting from the highest refinement level L, one calculates the multipole moments M_{lm} for particles in each box using Eqs.(3.4) and (3.5). Next one needs M_{lm} at all levels less than L (l = L-1, L-2, ..., 2). This requires a M_{lm}-to-M_{lm} transformation from the center of a box at level l to the center of another box at level l -1 (upward pass). Using the recursion relations for spherical harmonics, one derives the transformation as

$$M_{lm}=\frac{4\pi(2l+1)}{a_{lm}}\sum_{l'=0}^{l}\sum_{m'=-l'}^{l'}\frac{a_{l'm'}a_{l-l',m-m'}}{(2l'+1)[2(l-l')+1]}r_t^{(l-l')}Y_{l-l'}^{*m-m'}(\Omega_t)M'_{l'm'}, \qquad (3.5)$$

where

$$a_{lm}=(-1)^{l+m}\sqrt{\frac{2l+1}{4\pi(l+m)!(l-m)!}}\,. \qquad (3.6)$$

The parameters r_t and Ω_t are the displacement for the translations, as shown in Figure 3.5. In addition to M_{lm}-to-M_{lm} transformations, one also needs transformations for M_{lm}-to-L_{lm} and L_{lm}-to-L_{lm} (downward pass):

$$L_{lm}=4\pi a_{lm}\sum_{l'=0}^{\infty}\sum_{m'=-l'}^{l'}\frac{(-1)^{l'+m'}a_{l'm'}}{(2l'+1)a_{l+l',m-m'}}\frac{Y_{l+l'}^{*m-m'}(\Omega_t)}{r_t^{(l+l'+1)}}M'_{l'm'}, \qquad (3.8)$$

and

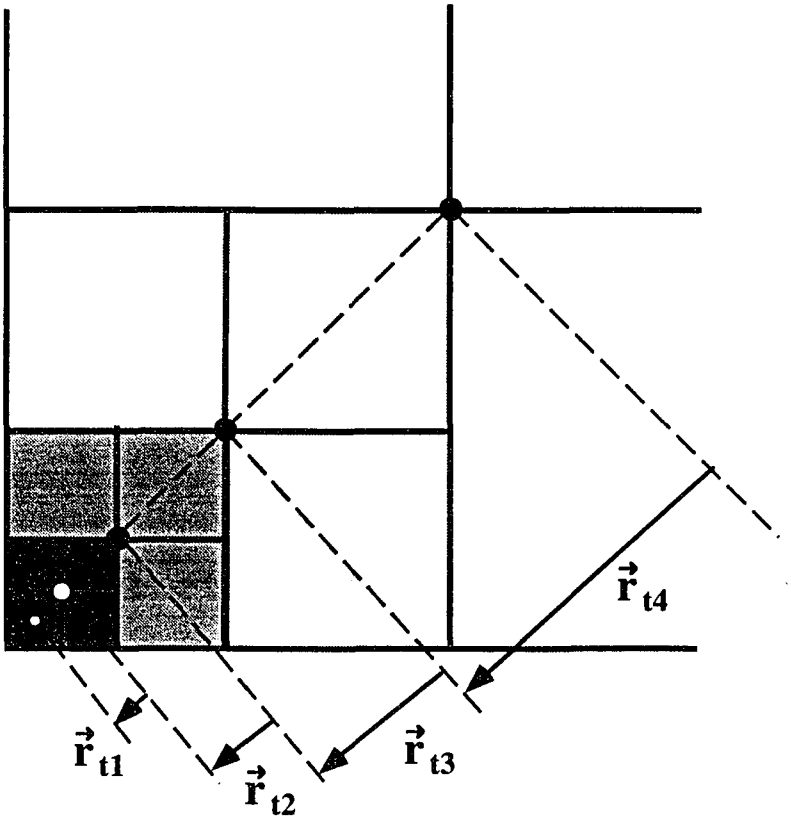

Figure 3.5 M_{lm}-to-M_{lm} transformation. The corresponding multipoles of a box at the lth level is transformed into the multipoles of the parent box (at the (l-1)th level) then the grandparent box (at the (l-2)th level), ..., and so on, through vectors $\vec{r}_{t1}$, $\vec{r}_{t2}$, $\vec{r}_{t3}$, $\vec{r}_{t4}$.

$$L_{lm}=4\pi a_{lm}\frac{a_{l'-l,m'-m}}{(2l'+1)a_{l'm'}}(-r_t)^{l'-l}Y_{l'-l}^{m'-m}(\Omega_t)L'_{l'm'}. \tag{3.9}$$

The M_{lm}-to-L_{lm} transformation is needed for translation from the center of a box at level l to the center of a 'well separated' box at the same level. The L_{lm}-to-L_{lm} transformation translates from the center of a box at level l to the center of a box at level $l+1$, see Figure 3.6.

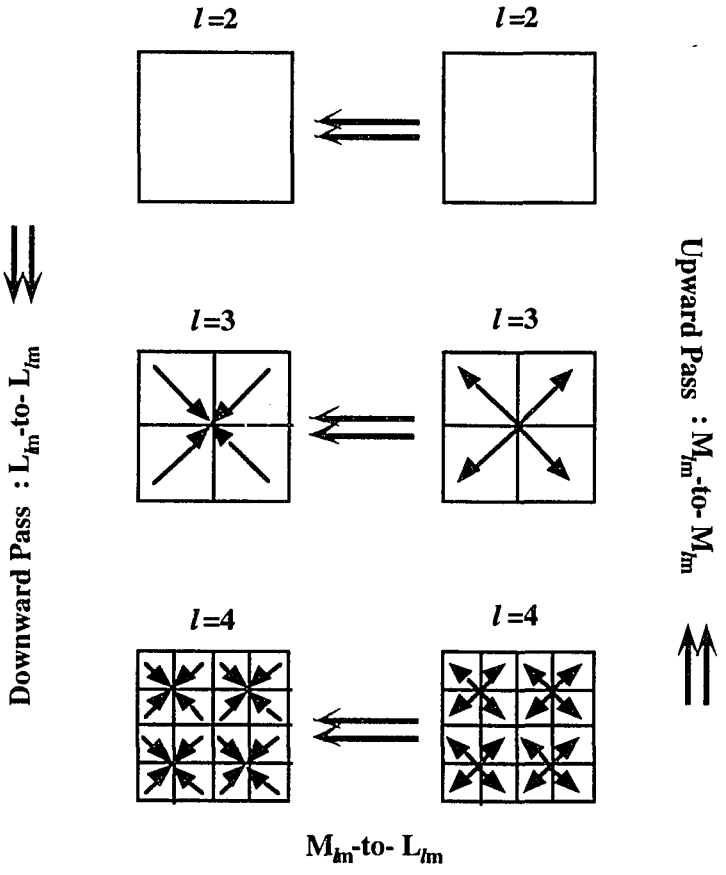

Figure 3.6 The far-field computation at the L=4 refinement box. Beginning from computing M_{lm} for the cells at l=4, the upward passing M_{lm}-to-M_{lm}, downward passing L_{lm}-to-L_{lm}, and the transformation M_{lm}-to-L_{lm} are used to compute multipoles for all the cells at all the levels.

This hierarchical combination of multipoles requires O(N) operations on a sequential machine if the level of refinement for an N particle system is L~$\log_8$N. For a large system, the implementation of FMM on a sequential machine is not practical. Therefore, we implement the FMM on a MIMD parallel machine.

In order to implement the FMM algorithm for bulk Coulombic systems, we need to introduce periodic boundary conditions. In the hierarchical refinement, the root of the

refinement corresponds to the simulation box. To calculate multipoles and local-poles that involve contributions from infinitely repeated image charges that are well-separated from the original simulation box, the reduced cell multipole method (RCMM) was recently suggested [114, 115]. The idea is to replace each well-separated image of multi-million particles by a small number of particles with the equivalent leading multipole expansions as the simulation box. In this way, the computation can be enormously reduced while the necessary accuracy is retained. Recently, a highly efficient MD algorithm based on multiresolution in both space and time has been developed in our lab by Nakano et al.[112]. The long range Coulomb potentials for periodic systems are computed with reduced cell multipole method (RCMM) and FMM.

3.3 Performance of FMM on Touchstone Delta machine

Using domain decomposition, the FMM method is implemented on the Intel iPSC/860 system at LSU (8 nodes) and Caltech (512 nodes). The cut-off for multipole moments and the definition of 'well-separated' interaction boxes (second or third nearest-neighbor boxes) are dictated by the level of precision desired for the potential-energy calculations. Because of the nature of domain decomposition, the internode communication in upward and downward passes is minimal. In the near-field calculation, communication is carried out with 13 neighboring processors by using the communication strategy described in Section 3.1.

3.3.1 Algorithm

Next we describe the implementation of the FMM on p processors. The number of particles on each processor is $N_p=N/p$. The level of refinement is L, and the cutoff level for multipole expansion is L_{max}.

Step 1: Initialization

- Divide the computational box into 8^L parts and determine the center of each box at each level;

- Set up a table for 1/r on r^2 mesh for the near-field direct calculation;
- Compute Y_{lm}'s for both M_{lm}-to-M_{lm} translation and M_{lm}-to-L_{lm} translation;
- Construct link-cell-list to locate particles in boxes at the finest level.

Step 2: Upward pass

- Compute multipoles M_{lm} for each box at level L;
- Use M_{lm}-to-M_{lm} translation to compute the multipoles for boxes at all the levels ≥ 2;
- Use message passing to gather information on multipoles for global memory;

Step 3: Downward pass

- For each box at level ≥ 2, use M_{lm}-to-L_{lm} translation to compute the local-poles due to all 'well-separated' boxes at the same level;
- Use L_{lm}-to-L_{lm} translation to compute local-poles for each box at higher level;
- Use the link-cell-list method to compute the far-field potential for each particle;

Step 4: Near field potential

- Send & receive messages for the positions of particles;
- Use link-cell-list and tables to compute pair-wise interaction.

3.3.2 Storage Requirement and Computation Complexity

We need to store the coordinates and forces of particles, as well as their contribution to the potential, multipoles and local-poles for all the boxes at all the levels ≥ 2, coordinates of the centers of boxes at all the levels, and the relative Y_{lm} for translations. The information about each individual particle is stored in the local memory of a processor, which is proportional to N_p. The information about multipoles is shared by all processors, and this is proportional to $8^L * L_{max}^2$. Therefore the total memory required on each processor is

$$a\,\frac{N}{p} + b\;8^{L}L_{max}^{2}.$$

The total number of operations has two major parts: M_{lm}-to-L_{lm} translation and direct calculation. Using the link-cell-list technique, the number of operations for direct calculation is proportional to N_p*N_b, where $N_b=N_p/8^L$, which is the number of particles per box at the finest level. If we determine the level of refinement by keeping N_b as a constant,

$$L = \text{int}\left[\log_8\left(\frac{N_p}{N_b}\right)\right], \tag{3.10}$$

where the function int[x] takes the maximum integer smaller than x. For an increase in N_p by a factor of 8, the level of refinement is upgraded by the same factor so that N_b remains constant. Therefore we can obtain a computational complexity for the direct calculation as O(N/p). On the other hand, the number of operations involved in M_{lm}-to-L_{lm} translation is approximately $8^L * L_{max}^4$. Therefore, upgrading the refinement level will dramatically increase the time for far-field calculation. The total computational time takes the form:

$$C[L(N/p),L_{max}] + D(L,p)\,N,$$

where $C[L(N/p),L_{max}]$ and $D(L,p)$ do not depend explicitly on the system size.

Note here, for small increases in N (by less than 8 times), we do not upgrade the level of refinement, therefore N_b increases with N. In this case, the algorithm will scale quadratically with the number of particles due to the calculation of local interactions through a direct $O(N^2)$ algorithm: $C'(L,L_{max}) + D'(L)\,N^2$). Thus, we always choose the refinement level in such a way that the far-field calculation dominates the near-field calculation. When the latter begins to dominate, we upgrade the refinement level by 1.

3.3.3 Results

Figure 3.7 shows the performance of the multiresolution MD algorithm involving FMM evaluation for long range Coulomb interaction. The physical system is SiO_2 modeled with a realistic interatomic potential. The number of particles is scaled linearly with the number of processors so that N_p=8232. The multipole moments are cut off at L_{max}=2. The relative error in the potential energy is about 10^{-3}. The machine used is the 512-node Touchstone Delta machine at Caltech. The execution time increases only slightly for large systems, which is mainly due to the increasing of communication time with number of processors. In other words, the execution time scales linearly with total number of particles in the system.

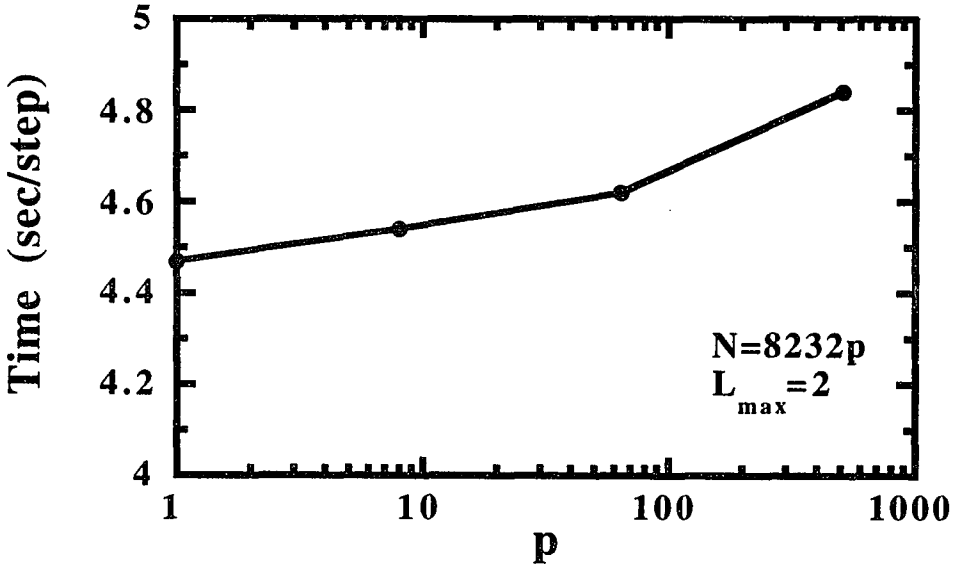

Figure 3.7 Execution time of the MRMD program involving FMM for long range Coulomb interaction. Work of Nakano et al. [112].

Next we show the potential calculation for systems with a uniform distribution of particles in a cubic box with free boundary conditions [116]. The system size is increased in a slow manner. The multipole moments are cut off at level L_{max}=4. Three

levels of refinement, L=2, 3, 4, are used according to the number of particles in the system. The relative precision of the total potential energy is at least 10^{-6}. The calculation is done with a single processor. Figure 3.8 shows a comparison between execution times for direct calculation and FMM.

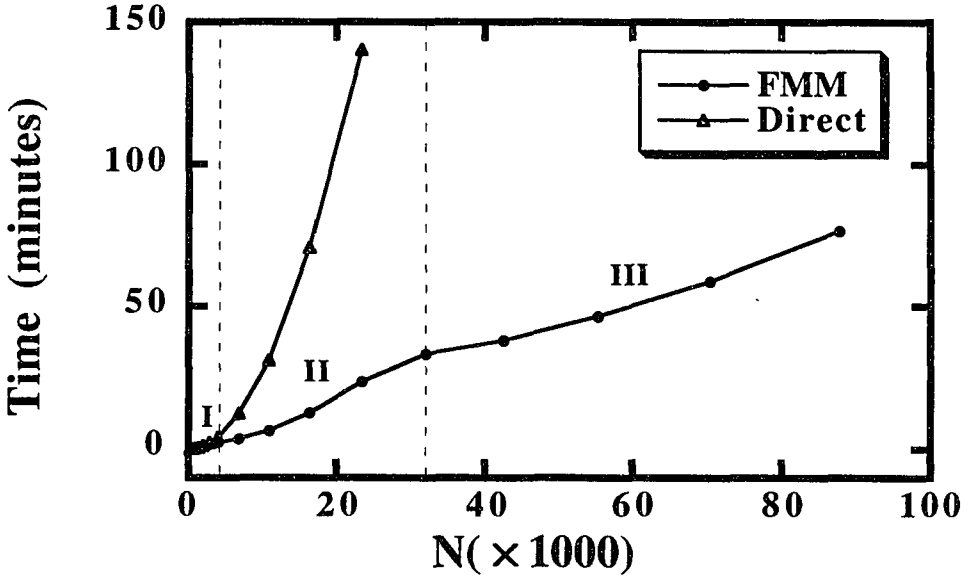

Figure 3.8 Performance of FMM (open circles) and direct calculation (open triangles) of potential. For FMM, the level of refinement is L=2 in region I, L=3 in region II, and L=4 in region III. Calculations are done on a single node.

Clearly, with each fixed level of refinement, the FMM shows local quadratic behavior due to the near-field calculation. But the overall computational time scales linearly with the system size. White and Head-Gordon have tested the performance of FMM on IBM RS/6000 Model 350 workstation [117]. They reported the similar system size dependence of the execution time.

The comparison between far-field and near-field calculations are done on 16 nodes. The level of refinement is chosen to be L=4. The multipoles are cut-off at level

L_{max}=5. The 'well-separated' boxes are those with distances at least 3 times the size of a subbox (boxes other than the first and second nearest-neighbor boxes). As a consequence, there are up to 875 (=10^3-5^3) boxes in the M_{lm}-to-L_{lm} transformation for each box. Table 3.1 lists the corresponding execution time for far-field and near-field calculation.

Table 3.1 Comparison of execution times for far-field and near-field potential energy calculation in FMM

N	far-field (sec)	near-field (sec)	total (sec)
13,824	97.3	1.8	101.0
32,768	97.3	3.5	102.8
46,656	97.4	5.2	104.7
64,000	97.4	8.2	107.8
110,592	97.4	19.8	119.6
175,616	97.4	46.4	146.9

It is clear that at this refinement level, the far-field contribution dominates the total execution time and remains constant. But the computational complexity is in order of $O(N^2)$ due to the quadratic scaling of the near-field potential calculation, as shown in Figure 3.9. When the cost in near-field calculation tends to dominate, it comes to the crossover point where the refinement level should be upgraded by 1. In practice, the limitation of storage capability on each node (16M bytes) is also a constraint for generating higher level refinement.

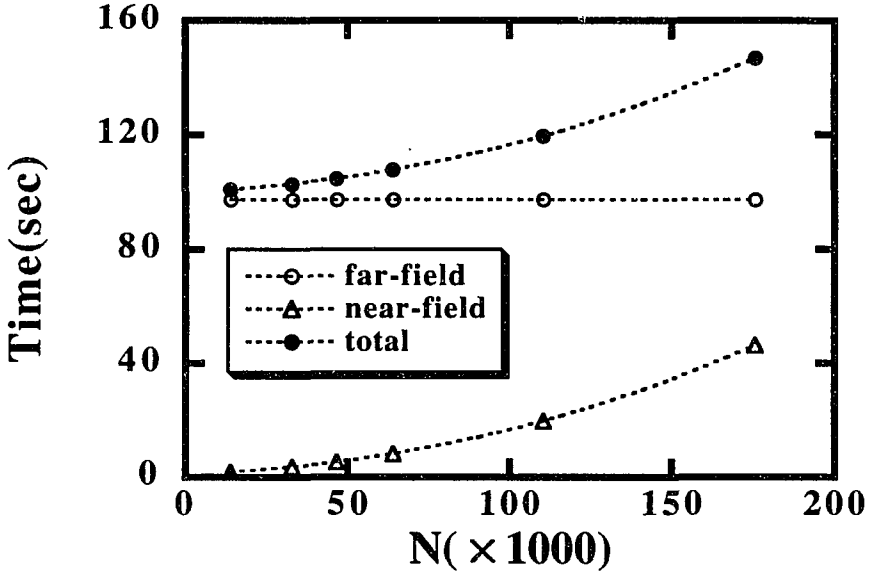

Figure 3.9 System size dependence of execution time for far-field and near-field potential evaluation in FMM. Calculations are done on 16 processors.

CHAPTER 4

STRUCTURE AND MECHANICAL PROPERTIES OF $SiSe_2$ NANOWIRES

In this chapter, we present the MD simulation results of silicon diselenide ($SiSe_2$) nanowires. In Figure 4.1 we show the two possible connectivities of tetrahedral units, namely edge-sharing and corner-sharing [118].

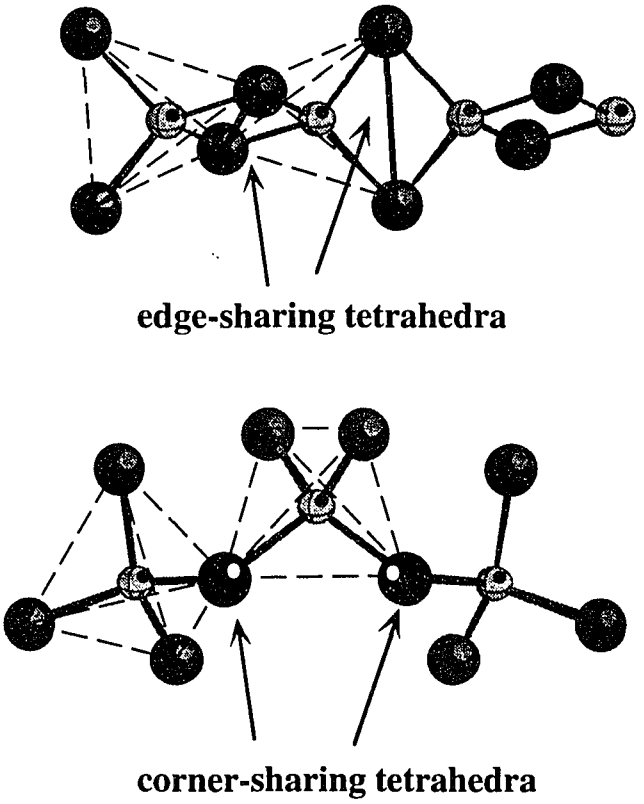

Figure 4.1 Two possible connectivities of tetrahedra: edge-sharing and corner-sharing configurations.

Crystalline SiO_2 is a three-dimensional network of only corner-sharing tetrahedra, while crystalline $GeSe_2$ consists of two-dimensional planes that are made up of both corner-sharing and edge-sharing tetrahedra. In contrast, crystalline $SiSe_2$ is built exclusively of edge-sharing tetrahedra, which leads to a one-dimensional network of chain-like structure. The present work is the first molecular-dynamics (MD) study on $SiSe_2$ nanowires. It provides insight into the mechanical behavior and glass-forming tendency of crystalline $SiSe_2$. Since bulk $SiSe_2$ is extremely sensitive to hydrolysis in moist air, it always requires special care in materials preparation and handling. We do not expect it to be an easy task to experimentally synthesize crystalline or amorphous $SiSe_2$ nanowires. However, understanding their structural, mechanical, and dynamical properties can provide helpful information for engineering design and material selection.

This chapter is organized as follows. In Section 4.1, we briefly describe the structural information of crystalline $SiSe_2$. The interatomic potentials that we have used for the simulations are given in Section 4.2. Section 4.3 describes the procedure for the preparation of $SiSe_2$ nanowires. The simulation results for structural properties and mechanical behavior are discussed in Section 4.4.

4.1 Crystalline Structure of $SiSe_2$

Crystalline silicon diselenide is orthorhombic with four $SiSe_4$ tetrahedra per unit cell [57]. At room temperature, T=293K, the lattice constants are a=9.669Å, b=5.998Å, and c=5.851Å. Crystalline density is 3.64g/cm^3. The non-intersecting chains are along the c-axis, see Figure 4.2.

The interatomic distances and bond angles of crystalline $SiSe_2$ are listed in Table 4.1. The coordination number for Si atoms is 4. For an ideal tetrahedron, the Se-Si-Se angle is 109^o. In c-$SiSe_2$, the three values of Se-Si-Se angle indicates the distortion of tetrahedra in c-$SiSe_2$. Among these angles, <Se-Si-Se=100^o is an intra-tetrahedral angle, which along with the Si-Se-Si angle forms a planar two-fold ring. In c-$SiSe_2$,

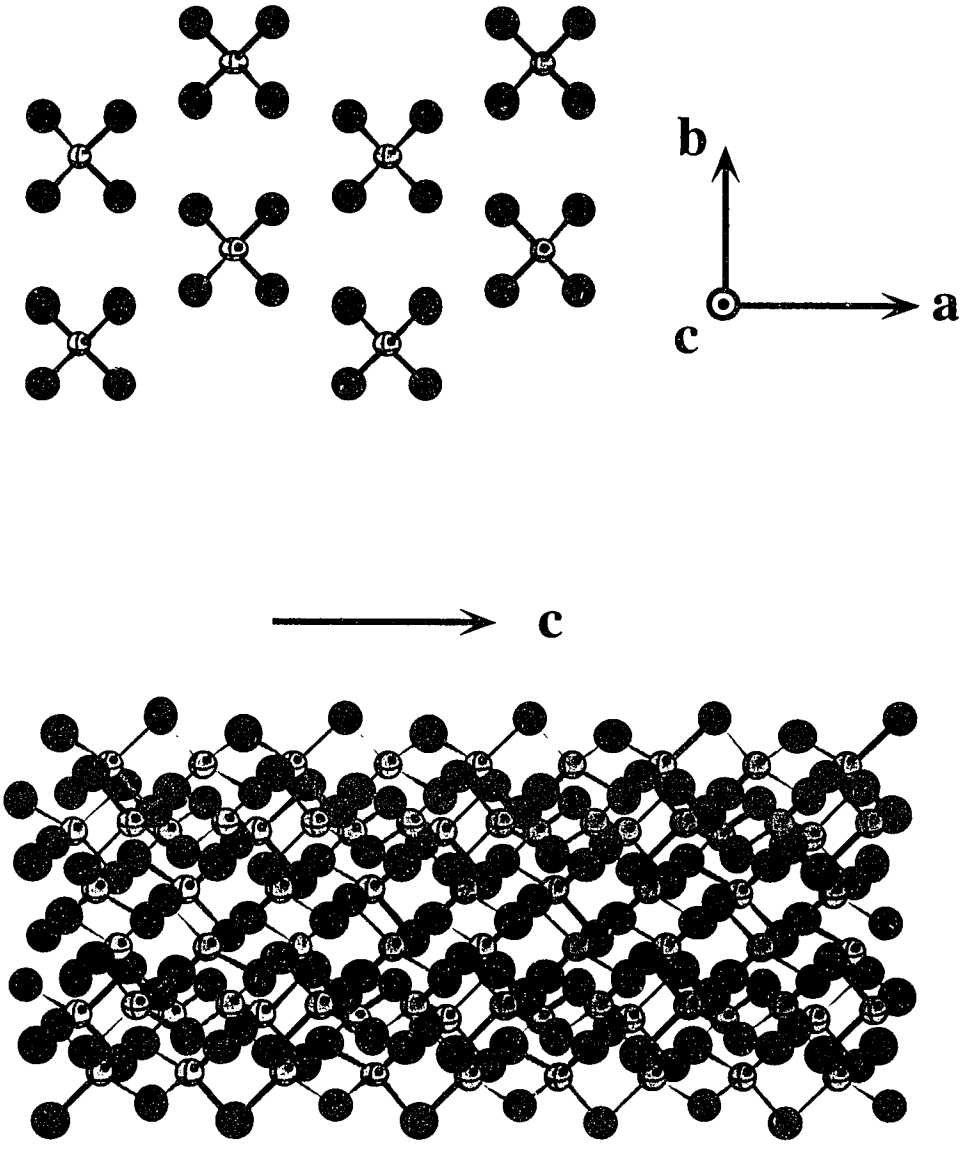

Figure 4.2 A segment of an 8-chain nanowire. Si atoms are represented by smaller and Se atoms by larger spheres. Each Si atom is connected with four Se atoms.

each Si atom has only two two-fold rings, which implies that the chains are non-intersecting.

Table 4.1 Interatomic distances and bond angles in crystalline $SiSe_2$

Si-Se	2.275Å
Si-Si	2.926Å (along a chain)
	5.689Å (between chains)
Se-Se	3.484~4.530Å
Si-Se-Si	80°
Se-Si-Se	100.0°
	112.2°
	116.7°

4.2 Interatomic Potential

Our simulations are based on an effective interatomic potential which includes both 2-body and 3-body interactions. The 2-body potential function consists of steric repulsion due to atomic sizes, screened Coulomb interaction caused by the charge-transfer effect, and charge-dipole interaction resulting from the large electronic polarizability of Se^{2-}. The 3-body covalent contribution takes into account the bond-bending effect, shown schematically in Figure 4.3.

For a system with N particles, the 2-body interaction has the form:

$$\mathcal{V}_2 = \sum_{i<j}^{N} \mathcal{V}_{ij}^{(2)}, \tag{4.1}$$

where

$$\mathcal{V}_{ij}^{(2)} = \frac{H_{ij}}{r_{ij}^{\eta_{ij}}} + \frac{Z_i Z_j}{r_{ij}} e^{-r_{ij}/r_{1s}} - \frac{P_{ij}}{r_{ij}^4} e^{-r_{ij}/r_{4s}}, \tag{4.2}$$

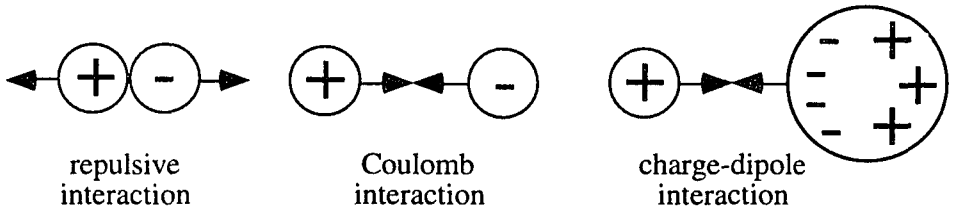

(a) two-body interaction

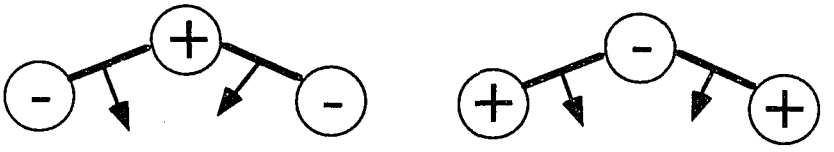

(b) three-body interaction

Figure 4.3 Schematic diagram of interatomic interactions.

$$H_{ij} = A_{ij}(\sigma_i + \sigma_j)^{\eta_{ij}}, \tag{4.3}$$

$$P_{ij} = (\alpha_i Z_j^2 + \alpha_j Z_i^2)/2, \qquad \text{i, j = 1, 2, ..., N.} \tag{4.4}$$

The 2-body potential has a cutoff radius r_c. Figure 4.4 shows the 2-body potential.

The 3-body interaction has the form:

$$\mathcal{V}_3 = \sum_{i<j<k}^{N} \mathcal{V}_{jik}^{(3)}, \tag{4.5}$$

where

$$\mathcal{V}_{jik}^{(3)} = B_{jik}(\cos\theta_{jik} - \cos\bar{\theta}_{jik})^2, \tag{4.6}$$

and

$$\cos\theta_{jik} = \frac{\vec{r}_{ik}\cdot\vec{r}_{ij}}{r_{ik}r_{ij}}, \qquad r_{ij}, r_{ik} < r_{c3}. \tag{4.7}$$

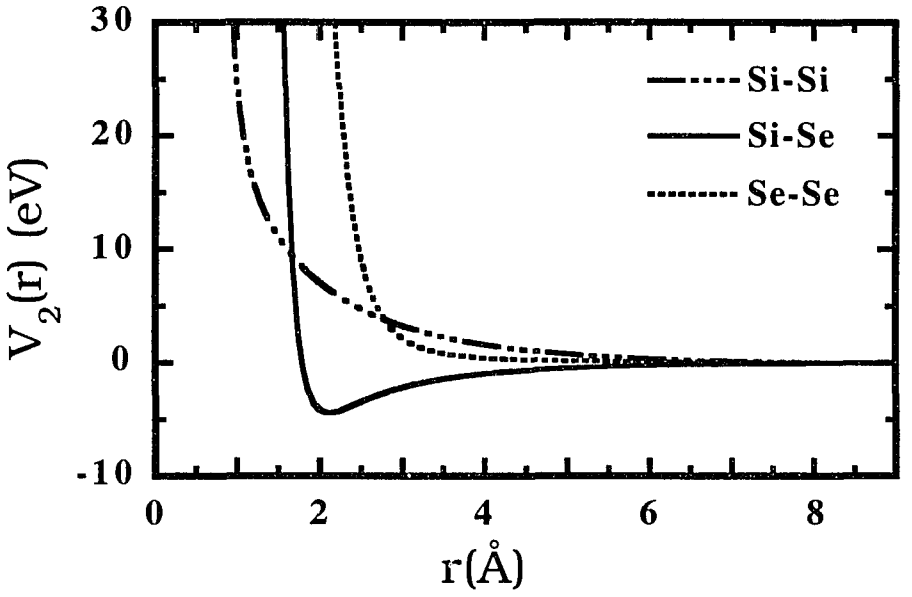

Figure 4.4 Si-Si, Si-Se, and Se-Se contribution to the 2-body part of the interaction potentials, Eq.(4.2), for $SiSe_2$. The cutoff is at r_c=9.0Å.

The parameters defined in the potential, such as, ionic radii σ_i, repulsive exponents η_{ij}, repulsive strength A_{ij}, effective charges Z_i, polarizabilities α_i, strength of 3-body interaction B_{jik}, average bond angles $\bar{\theta}_{jik}$, and the cut-off distances for 2-body and 3-body interactions are given in Table 4.1.

The potential function used in this paper is different from the potential proposed in reference [96]. In reference [96], the 3-body interaction contains not only a bond-bending term but also a bond-stretching term:

$$V_{jik}^{(3)} = B_{jik}\, f(r_{ij}, r_{ik})\, (\cos\theta_{jik} - \cos\bar{\theta}_{jik})^2, \tag{4.8}$$

where

$$f(r_{ij}, r_{ik}) = \exp\left(\frac{l}{r_{ij} - r_{c3}} + \frac{l}{r_{ik} - r_{c3}}\right), \qquad r_{ij}, r_{ik} < r_{c3}. \tag{4.9}$$

Table 4.2 Parameters in the interaction potential for $SiSe_2$.

$A_{ij}(erg)$	$r_{s1}(Å)$	$r_{s4}(Å)$	$r_c(Å)$	$r_{c3}(Å)$
$1.610e^{-12}$	4.43	4.43	9.0	3.0

	$\sigma_i(Å)$	$Z_i(e)$	$\alpha_i(Å^3)$
Si	0.675	1.3456	0.00
Se	2.045	-0.6728	7.00

	η_{ij}
Si-Si	13
Si-Se	11
Se-Se	9

	B_{jik} (erg)	$\bar{\theta}_{jik}$
Si-Se-Si	1.9728e-11	80.00
Se-Si-Se	0.9864e-11	109.47

This potential has been used in molecular-dynamics simulations to study structural correlations and dynamical properties of many ionic covalent materials at various densities and temperatures [77, 96, 119-122]. The simulation results for static structure factors and phonon density-of-states are in good agreement with experiments. Now we compare the MD results for $SiSe_2$ with experiments. (The MD simulations for $SiSe_2$ employ Eq.(4.6) for 3-body interaction.) For example, we have calculated the neutron static structure factor, $S_n(q)$ for the 3-D bulk system with 13,824 particles. Simulations are done with the variable-shape MD method (isoenthalpy ensemble). The coherent neutron-scattering length for Si and Se are $b_{Si} = 0.4149 \times 10^{-14}$ m and $b_{Se} = 0.7970 \times 10^{-14}$ m [65]. Figure 4.5 shows the MD results along with the experimental data. Clearly, the results of the MD simulation are in good agreement with the diffraction data [65] for amorphous $SiSe_2$. Figure 4.6 shows the constants of self-diffusion of Si and Se as functions of temperature.

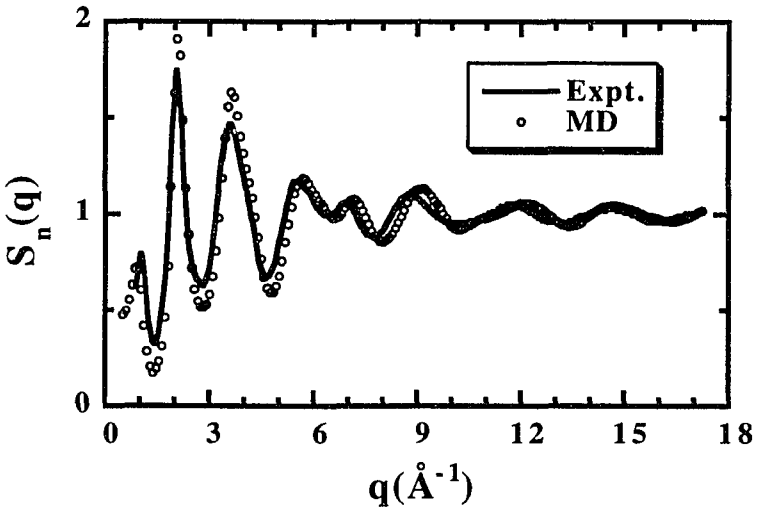

Figure 4.5 Neutron static structure factor for $SiSe_2$ glass at 200K.

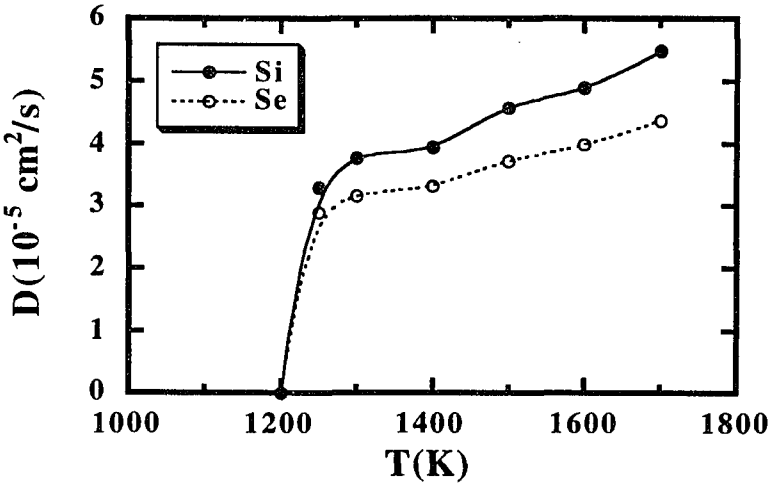

Figure 4.6 Constants of self-diffusion for silicon and selenium vs. temperature. MD results for melting temperature is T_m=1250±50K.

These results and the temperature dependence of the total energy suggest that the melting temperature is, T_m=1250K±50K, which agrees very well with the experimental result T_m=1233K± 5K [67].

4.3 Preparation of $SiSe_2$ Nanowires

$SiSe_2$ nanowires with m (m = 1, 2, 3, 4, 5, 8, 12, 16, 17, 32 and 64) adjacent chains were obtained from the three-dimensional crystalline structure. The number of particles in a nanowire is $m \times 3600$, which varies from 3,600 to 230,400. All of the nanowires we have simulated are of length 3,510.6Å. The diameters of these nanowires range from 10 to 60Å. Periodic boundary conditions are applied only along the c-axis, while the systems are free to move along the other two directions.

Simulations are done in the microcanonical ensemble. During the simulations, a time step of $\Delta t=1.45\times10^{-15}$ second is used, which conserves the energy to one part in 10^6. The MD simulation schedule is described schematically in Figure 4.7. Starting from the crystalline $SiSe_2$, each nanowire is heated gradually to a temperature of 100K over a period of 20,000Δt. The nanowires are then equilibrated for 30,000Δt at 100K. A temperature control of ±5K is used during these simulations. The long simulations are necessary to assure that the nanowires are well thermalized at finite temperatures. To bring nanowires into local minimum-energy configurations, we apply the Steepest Descent Quench (SDQ) scheme [92] using the conjugate gradient approach [94, 123] after an MD quench. The conjugate gradient method is briefly described in Appendix B. To determine the mechanical behavior of nanowires, we apply an uniaxial strain, ε_{zz}, along the c-axis. This is done by uniformly scaling the c-coordinates of all particles by a constant 1.01 (for stretching) or 1/1.01 (for releasing). Subsequently the nanowires are thermalized for 4,000 times steps at 100K and a SDQ is applied to obtain the corresponding minimum energy configurations. We repeat this procedure until the strain reaches the critical value for fracture.

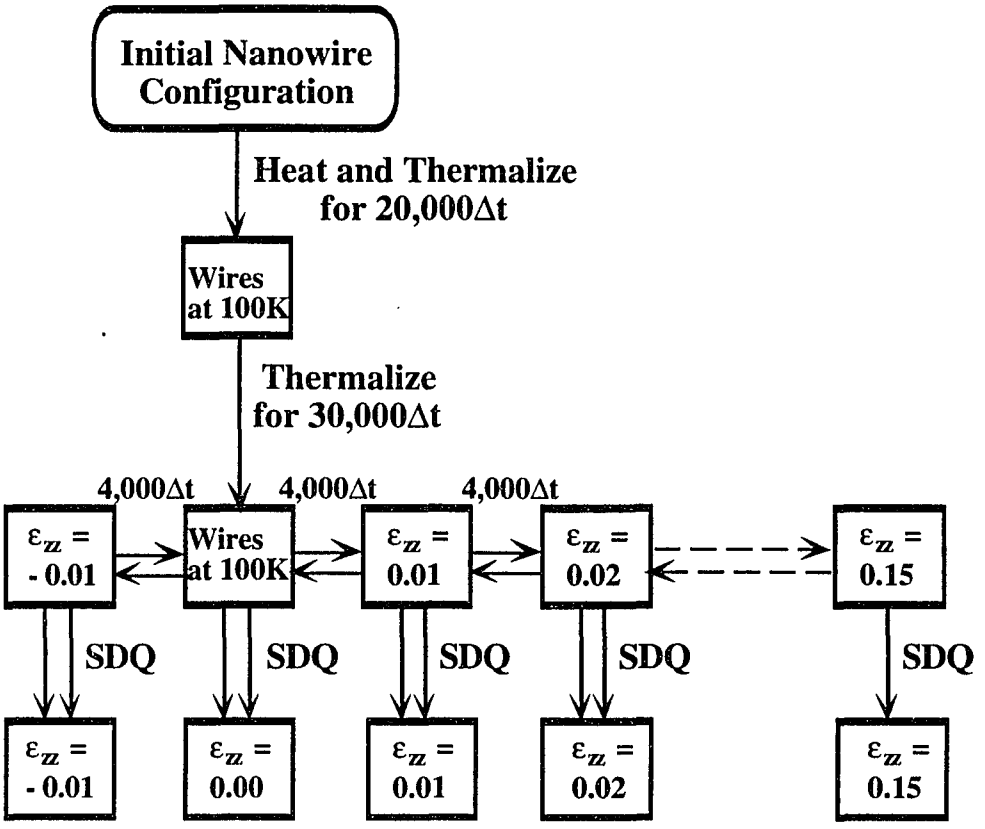

Figure 4.7 Schematic diagram of MD schedule used in preparing $SiSe_2$ nanowires. SDQ stands for Steepest Descent Quench.

4.4 Simulation Results

Nanowires that we have simulated have several common features. Under zero strain, the nanowires have wiggles. Below the critical strain, the nanowires remain highly crystalline and stay in the elastic deformation regime. In the next two subsections we present the results for structural properties and mechanical behavior of nanowires.

4.4.1 Structural Properties

• Structural Correlations

Atomic structures of nanowires are obtained from partial pair-distribution functions $g_{\alpha\beta}(r)$, nearest-neighbor coordinations, bond-angle distributions, and ring

statistics [124, 125]. It is found that the non-intersecting chain-like structures remain intact in nanowires under small uniaxial strain. The pair-distribution functions for all nanowires with different number of chains show some common features. For example, each silicon atom in a nanowire is connected to four selenium atoms and each selenium atom has two silicon atoms as nearest neighbors. In terms of rings, each silicon atom has only two two-fold rings, which indicates that there is no cross-linking between chains. Figures 4.8 and Figure 4.9 show the changes in structural correlation functions and coordination numbers of Si in an 8-chain nanowire during the stretching process. In a nanowire without any external strain, the Si-Se bond length (2.235Å) and the Si-Si distance between chains (5.335Å) are slightly less than those in the crystalline system (2.275Å and 5.689Å). In other words, the structure of chains is slightly more compact than that of c-$SiSe_2$. When a nanowire is stretched, the Si-Se bond length and the Si-Si distance along a single chain (the first peak in $g_{Si-Si}(r)$) increase and the Si-Si distance between adjacent chains (the second peak in $g_{Si-Si}(r)$) decreases. Figure 4.10 shows bond-angle distributions during the stretching process in an 8-chain nanowire. The bond angle Si-Se-Si increases from the ideal crystalline value of 80° to 91°, whereas the intra-tetrahedra Se-Si-Se angle decreases from 100° to 88°. These features are results from the Possion effect [126]. Since the main peaks in bond angle distributions are sharp, it indicates that there is no cross-linking between chains. This is also confirmed by the analysis of rings. The above statements for an 8-chain nanowire hold for all of the nanowires that we have simulated.

• Oscillatory Behavior

Depending on the number of chains in a nanowire, we find wiggles of amplitudes ~0.5Å and wavelengths ~100Å. The wiggles in nanowires give rise to sharp features in the static structure factors S(q). In the present study, we have used the following equation to calculate S(q) for small q's:

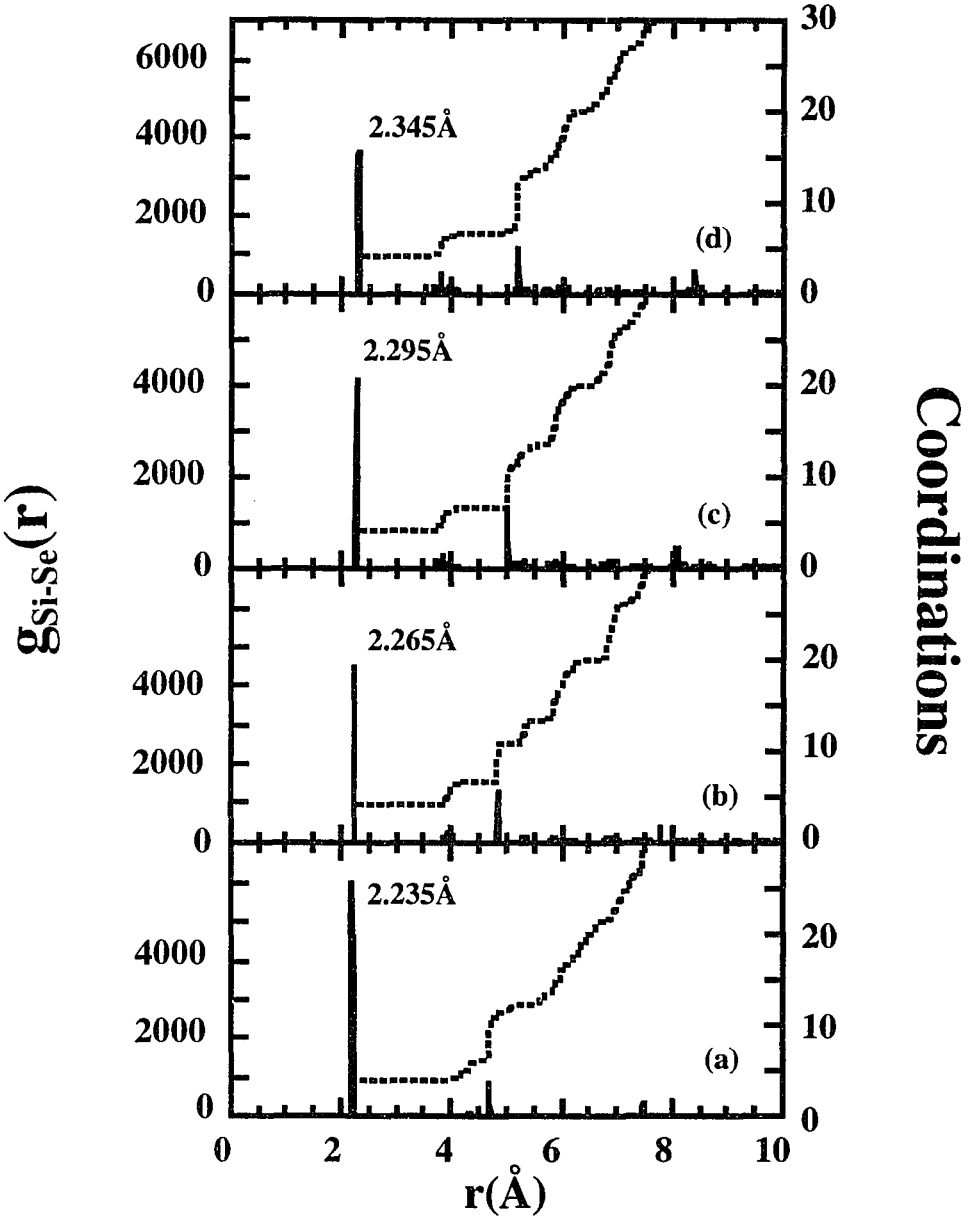

Figure 4.8 Partial pair distribution functions $g_{Si\text{-}Se}(r)$. (a) ε_{zz}=0.00; (b) ε_{zz}=0.04; (c) ε_{zz}=0.08; and (d) ε_{zz}=0.12.

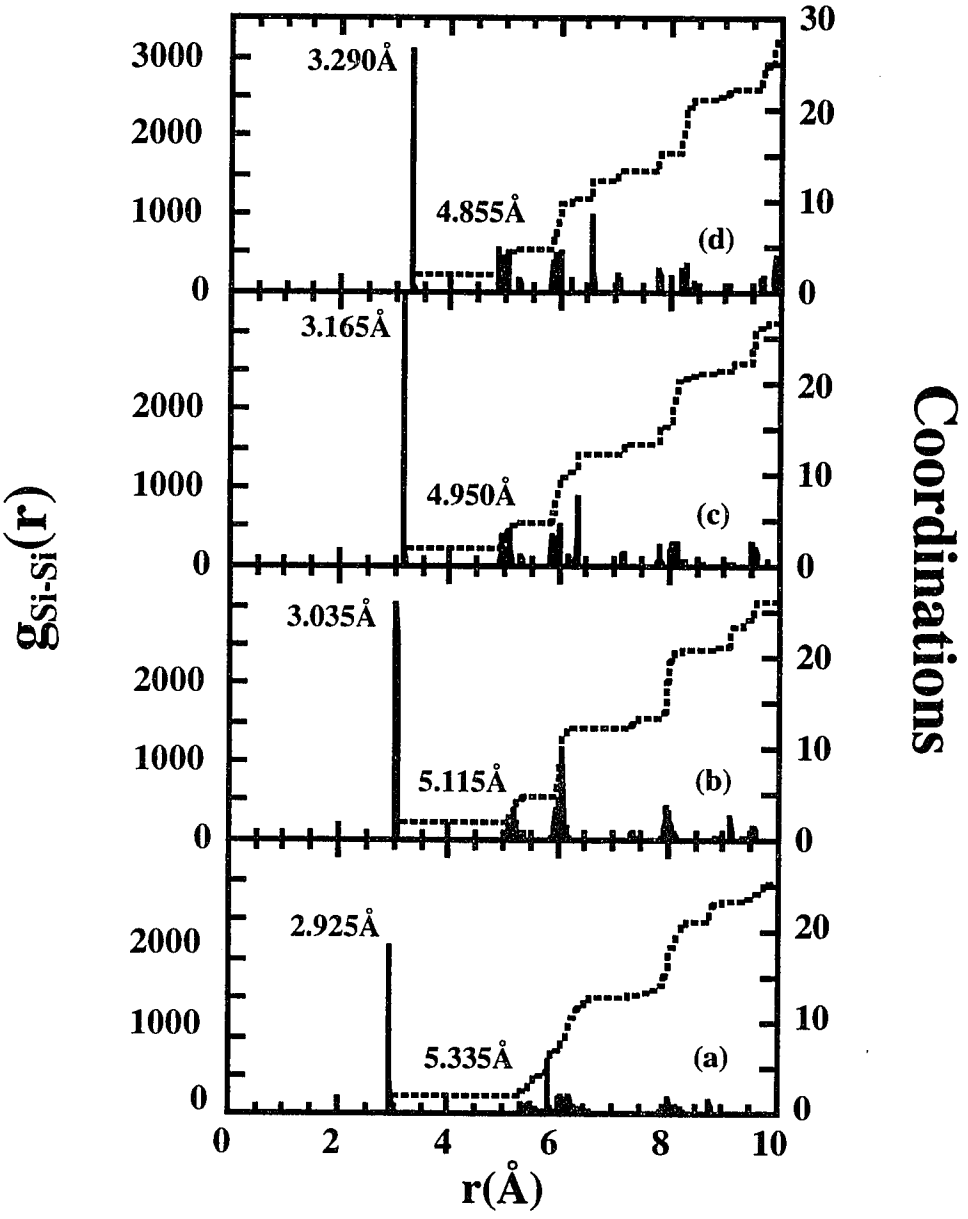

Figure 4.9 Partial pair distribution functions $g_{Si\text{-}Si}(r)$. (a) ε_{zz}=0.00; (b) ε_{zz}=0.04; (c) ε_{zz}=0.08; and (d) ε_{zz}=0.12.

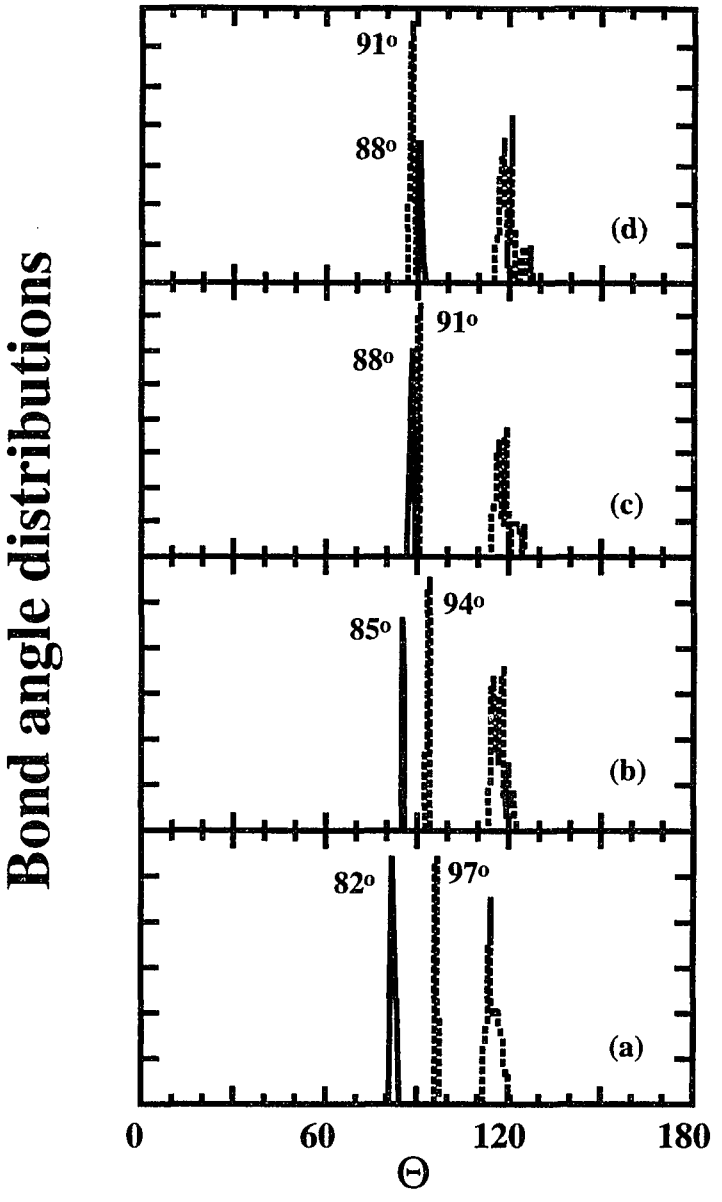

Figure 4.10 Bond angle distributions. Solid and dotted lines are Si-Se-Si and Se-Si-Se distributions, respectively. (a) ε_{zz}=0.00; (b) ε_{zz}=0.04; (c) ε_{zz}=0.08; and (d) ε_{zz}=0.12.

$$S(q) = \left| [\sum_{i=1}^{N} \exp(i\,\vec{q}\cdot\vec{r}_i)] \right|^2 / N, \tag{4.10}$$

where,

$$\vec{q} = (0,0,q), \tag{4.11}$$

$$q = N_q \times dq, \tag{4.12}$$

$$dq = 2p / L_0. \tag{4.13}$$

N_q is a positive integer which has been chosen to be 100. L_0 is the size of a nanowire in the c direction ($L_0=(1+\varepsilon_{zz})\times 3510.6$Å). At 100K, the unstrained nanowires are thermalized for 10,000Δt. We evaluate S(q) from Eq.(4.10) at regular intervals (after 10 time steps). The final results for S(q) are obtained from an average over 1,000 configurations. We repeat this schedule for nanowires under a strain of $\varepsilon_{zz} = \pm 0.02$. The static structure factors for a 2-chain nanowire are shown in Figure 4.11. We find that the main oscillatory peaks are considerably enhanced under compression (ε_{zz}=-0.02) and suppressed under tension (ε_{zz}=+0.02).

The linear density of Si atoms is calculated to schematically show the oscillatory pattern. A nanowire can be treated as a one-dimensional network of Si atoms. In a $SiSe_2$ crystal, the silicon atoms are uniformly distributed along the c-axis. Therefore, the linear density of Si atoms is constant in the crystalline structure. We have examined the linear densities of nanowires by counting the number of silicon atoms every two tetrahedral units along the c-axis. For instance, the density of a 5-chain nanowire should be 20 (number of Si atoms per two unit cells) in its initial crystalline configuration. If the wiggles make the distributions non-uniform, it should manifest itself in the linear density. On the other hand, when a nanowire is stretched beyond a certain value of the strain, a sudden reduction in the local density indicates the breaking of edge-sharing

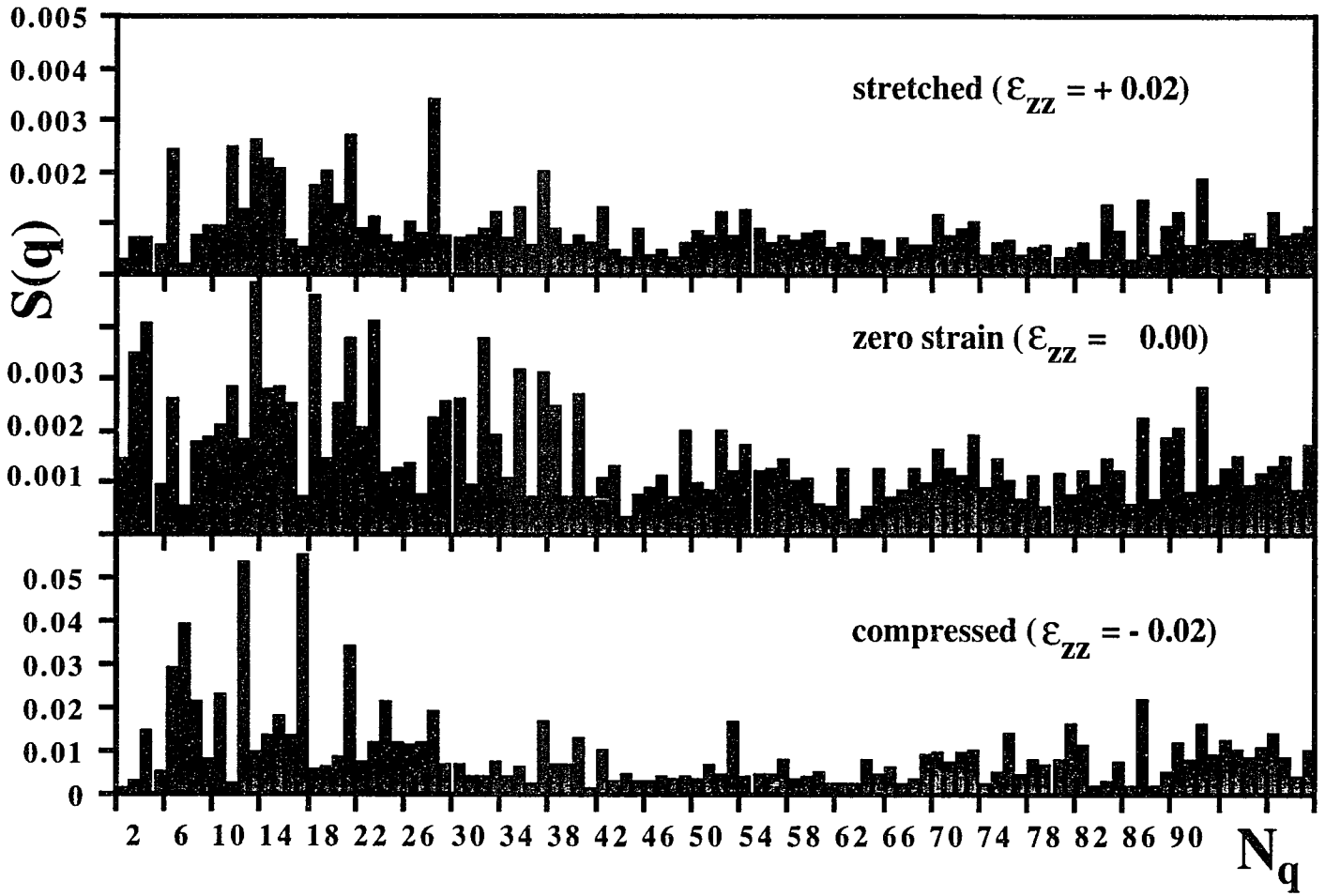

Figure 4.11 Static structure factor for a 2-chain nanowire. Major peaks are greatly enhenced when nanowire is compressed and weakened when nanowire is stretched.

bonds. Figure 4.12 depicts the linear density of Si atom during the stretching process for a 5-chain nanowire. It is evident that the unstrained nanowire has wiggles. When the nanowire is stretched to ε_{zz}=0.05 the wiggles tend to disappear, and at ε_{zz}=0.15 the nanowire breaks. Other nanowires display similar behavior.

4.4.2 Mechanical Properties

• Energy vs. Displacement

As expected, in the elastic deformation regime the internal potential energy of a nanowire depends quadratically on the net displacement along the c-axis, see Figure 4.13. When we scale the coordinates of atoms by a factor of 1.01, the nanowire is stretched to a length of L_0+dL. Here L_0 is the original length of the nanowire and dL is the total displacement. The nanowire is thermalized for 4,000Δt. The potential energy per particle $E_{stretching}$ is calculated after we apply an SDQ to obtain the minimum energy configuration. At the time when we calculate $E_{stretching}$, we scale the coordinates of all atoms by a factor of 1/1.01 and then compute the potential energy per particle $E_{releasing}$ after applying the SDQ. We repeat the above schedule until the strain reaches the critical value for fracture. Clearly, the nanowires remain in the elastic deformation regime and there is no noticeable plastic deformation up to the critical strain.

• Force Constant vs. Number of chains

The restoring force on a nanowire is calculated from the first derivative of the energy with respect to the displacement. We first fit the energy-displacement to:

$$E_{stretching} = m_0 + m_1\, dL + m_2\, dL^2 + m_3\, dL^3, \tag{4.14}$$

where m_0, ..., m_3 are the fitting coefficients. Next $F_{restoring}$ is calculated from

$$\begin{aligned} F_{restoring} &= -N \frac{\partial E_{stretching}}{\partial L} \\ &= -N\,(m_1 + 2m_2\, dL + 3m_3\, dL^2), \end{aligned} \tag{4.15}$$

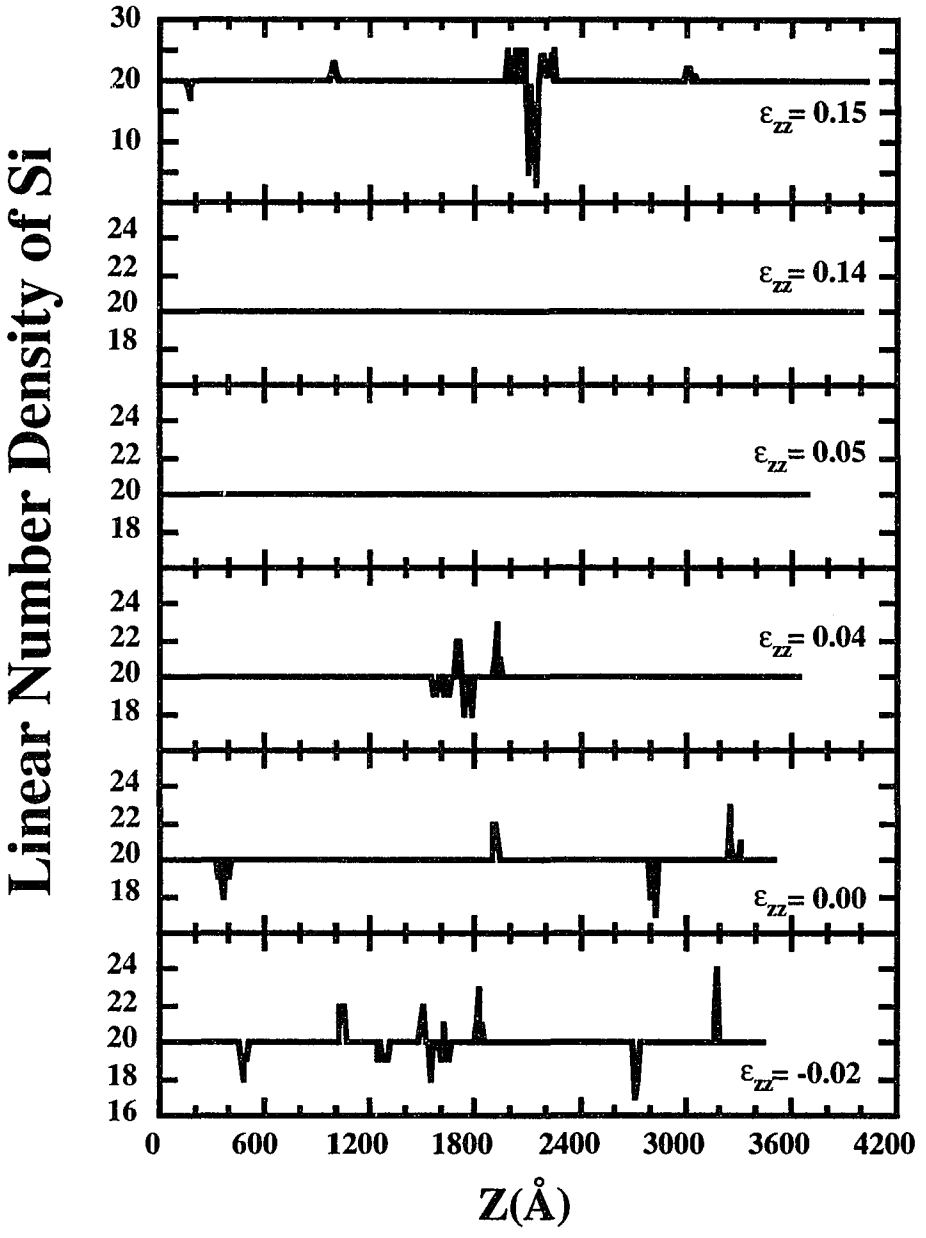

Figure 4.12 Linear number density of Si for a 5-chain nanowire. The density of the initial crystalline configuration gives a constant of 20 per two tetrahedral units.This nanowire breaks at 15% stretching, which is indicated by the sudden change of local density at about z=2200Å.

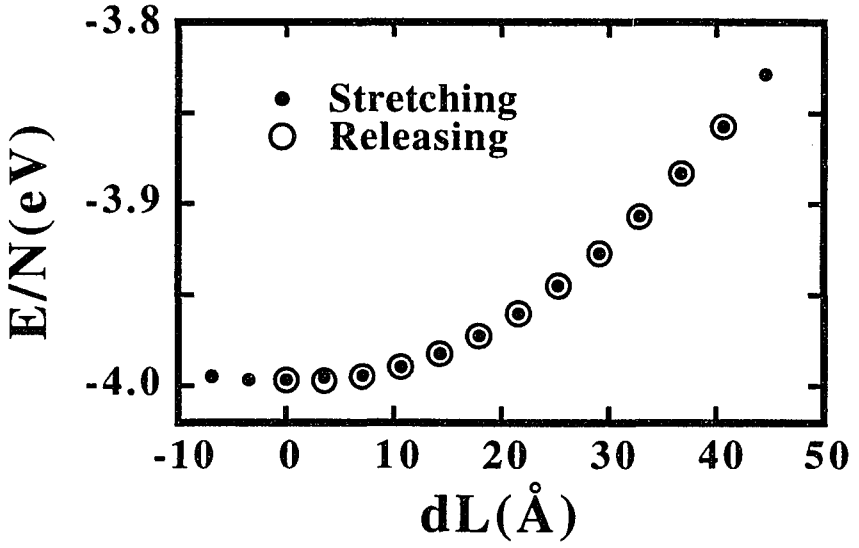

Figure 4.13 Internal potential energy vs. net displacement for an 8-chain nanowire during stretching (solid dots) and after releasing (open circles). The stretching process is clearly reversible.

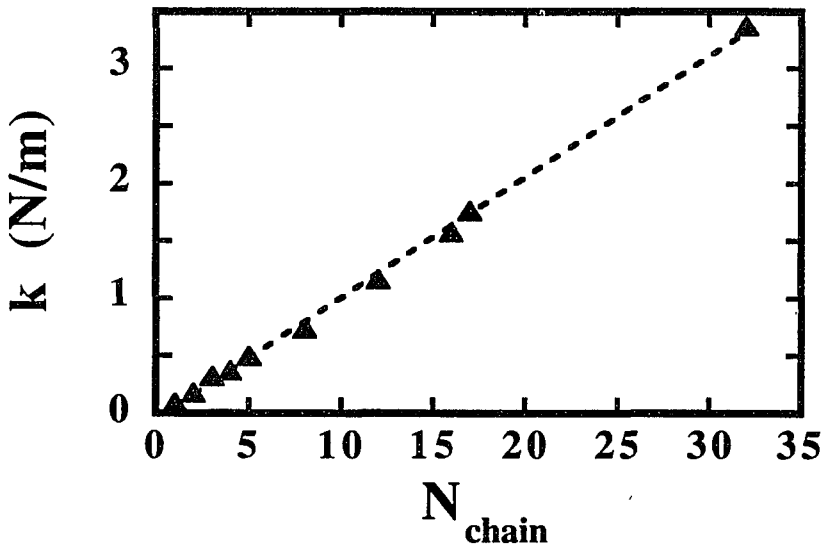

Figure 4.14 Force constant vs. the number of chains in a nanowire.

where N is the total number of particles in a nanowire. Since the nanowires remain in the elastic deformation regime, the forces scale linearly with the displacement and then the force constants k are obtained. In Figure 4.14 we plot the force constant as a function of number of chains. Clearly, the force constant scales linearly with the number of chains. This suggests that intra-chain interactions in nanowires are strong and responsible for the macroscopic mechanical behavior of nanowires. Inter-chain interactions are weak, but they contribute to the binding of chains.

• Stress vs. Strain

To determine stress on nanowires we need to estimate their cross-section area. We slice the nanowires along the c-axis and project each slice onto the a-b plane. For each slice, we use the Convex Hull algorithm [127] to determine the outermost selenium atoms $A_i(x_i,y_i)$ (i=1, 2, ...,k) that form a polygon, see Figure 4.15. The average ionic radius of Se^{-2} is taken to be 1.98Å [128], which is added to the polygon.

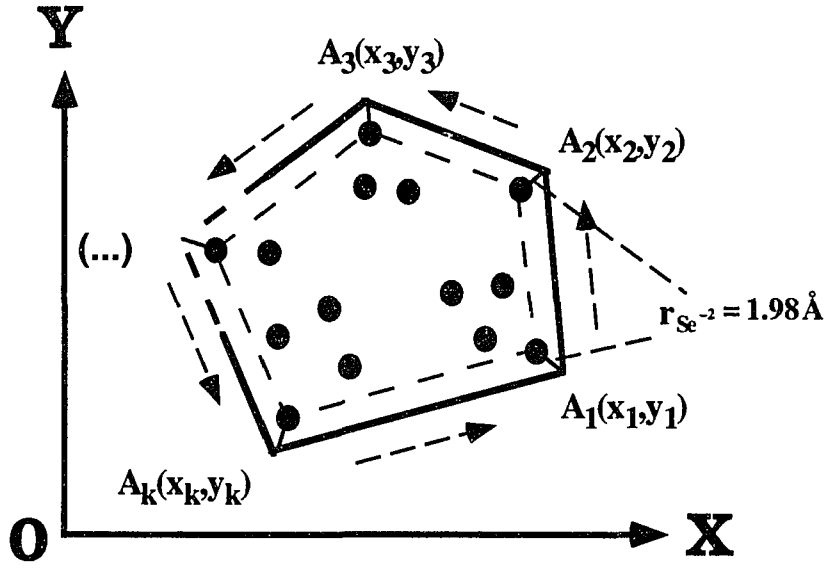

Figure 4.15 Estimation of cross section area. The outermost selenium atoms $A_i(x_i,y_i)$ (i=1, 2, ...,k) form a counter-clock contour.

The mean area of all of the polygons is then taken as an estimate of the average area of the nanowire:

$$S = \frac{1}{2}\left(\begin{vmatrix} x_1 & y_1 \\ x_2 & y_2 \end{vmatrix} + \begin{vmatrix} x_2 & y_2 \\ x_3 & y_3 \end{vmatrix} + \ldots + \begin{vmatrix} x_k & y_k \\ x_1 & y_1 \end{vmatrix} \right). \tag{4.17}$$

Figure 4.16 shows the stress-strain curves for nanowires containing 8, 16, and 32 chains. We do not find a significant difference in the Young's modulus for $SiSe_2$ nanowires with different number of chains. The Young's modulus for c-$SiSe_2$ nanowires is on the order of 100-130 Gpa. For comparison, Table 4.2 lists Young's modulus for some other materials [129]. To the best of our knowledge, there are no experimental results available for the Young's modulus or bulk modulus of $SiSe_2$.

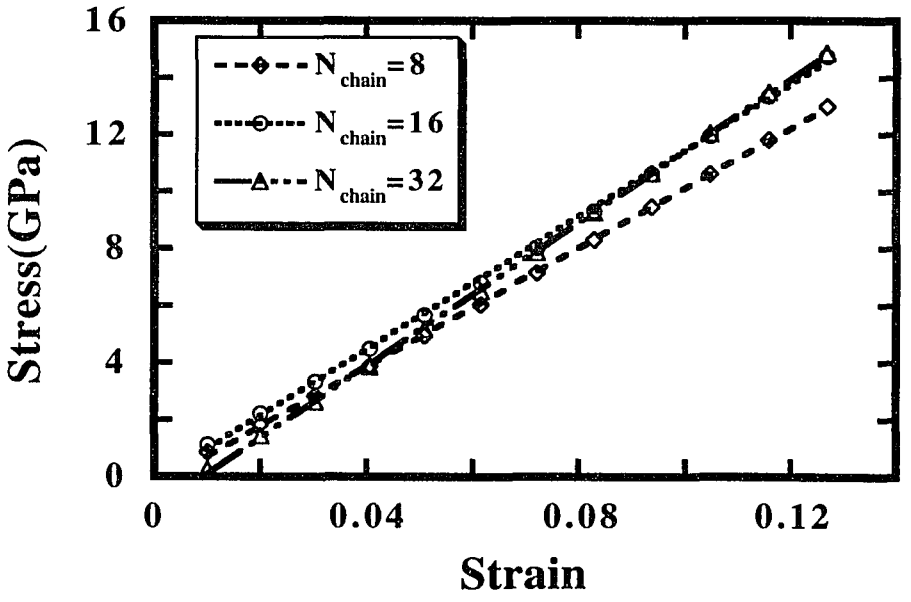

Figure 4.16 Stress vs. strain for nanowires containing 8, 16, and 32 chains. Young's modulus are obtained from the linear fit.

Table 4.3 Young's modulus Y of various materials

Material	Y(Gpa)
Aluminum	70
Brass	90
Copper	110
Steel	200
c-$SiSe_2$ nanowire (along the c-axis)	100-130

CHAPTER 5

AMORPHIZATION AND FRACTURE OF $SiSe_2$ NANOWIRES

In this chapter, we report the results of MD simulations on amorphization and fracture in silicon diselenide nanowires. These nanowires contain a finite number (1-64) of chains of edge-sharing tetrahedra. We have found that fracture in $SiSe_2$ nanowires is preceded by an amorphization process. Breaking of edge-sharing bonds results in the formation of corner-sharing tetrahedra. This causes local cross-linking of chains and initiates the propagation of local amorphization in the nanowires. Nanowires fracture at the amorphous-crystalline boundaries.

The simulation results are presented in three parts. We first describe the time sequence of fracture in $SiSe_2$ nanowires in Section 5.1. The analyses of amorphization, crack propagation, and dynamical fracture in nanowires are discussed in Section 5.2.

5.1 Nanowires Under Critical Strain

One interesting feature of $SiSe_2$ nanowires is that they all have the same critical value of strain (ε_{zz} =15%). Figures 5.1(a)-5.1(f) show a series of snapshots of a 64-chain nanowire projected onto the a-b plane. The number of particles in this nanowire is 230,400. (In these figures, only Si atoms are shown.) The elapsed time is measured from the moment when the critical strain is reached. At t=6.5 ps, we observe disorder in one of the chains in the outermost layer. As time evolves, the disorder spreads over an increasing number of chains. At t=10.9 ps, all of the chains in the nanowire become disordered. Figures 5.2(a)-5.2(f) show the same series of snapshots projected onto the b-c plane. In these snapshots, we zoom into the disordered structure (about one fifth of the whole nanowire). We observe that disorder is localized along the c-axis and it expands longitudinally with time. A sandwich-like structure is formed with the

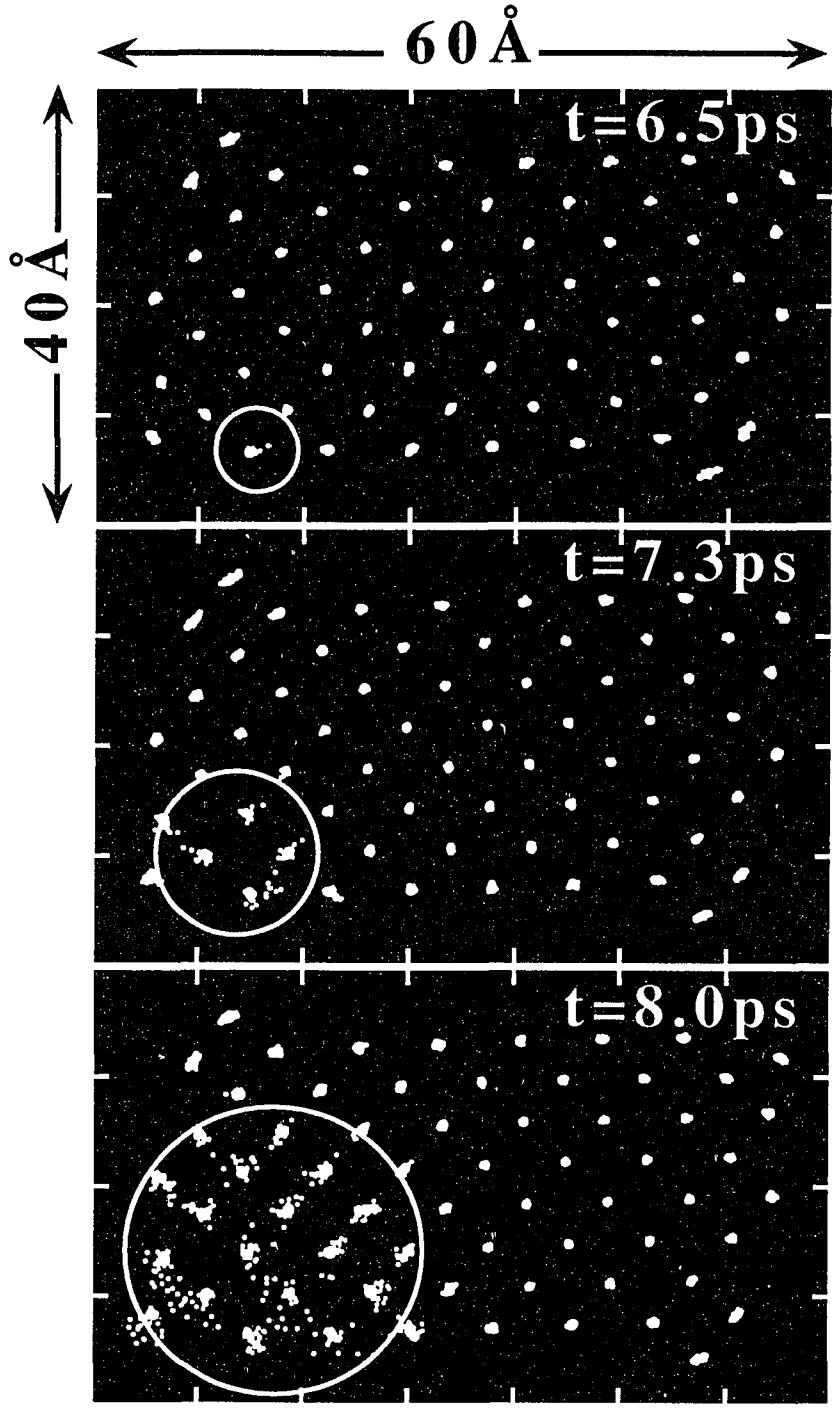

Figure 5.1 Snapshots (a)-(f) of a 64-chain nanowire projected onto the a-b plane. Only Si atoms are shown

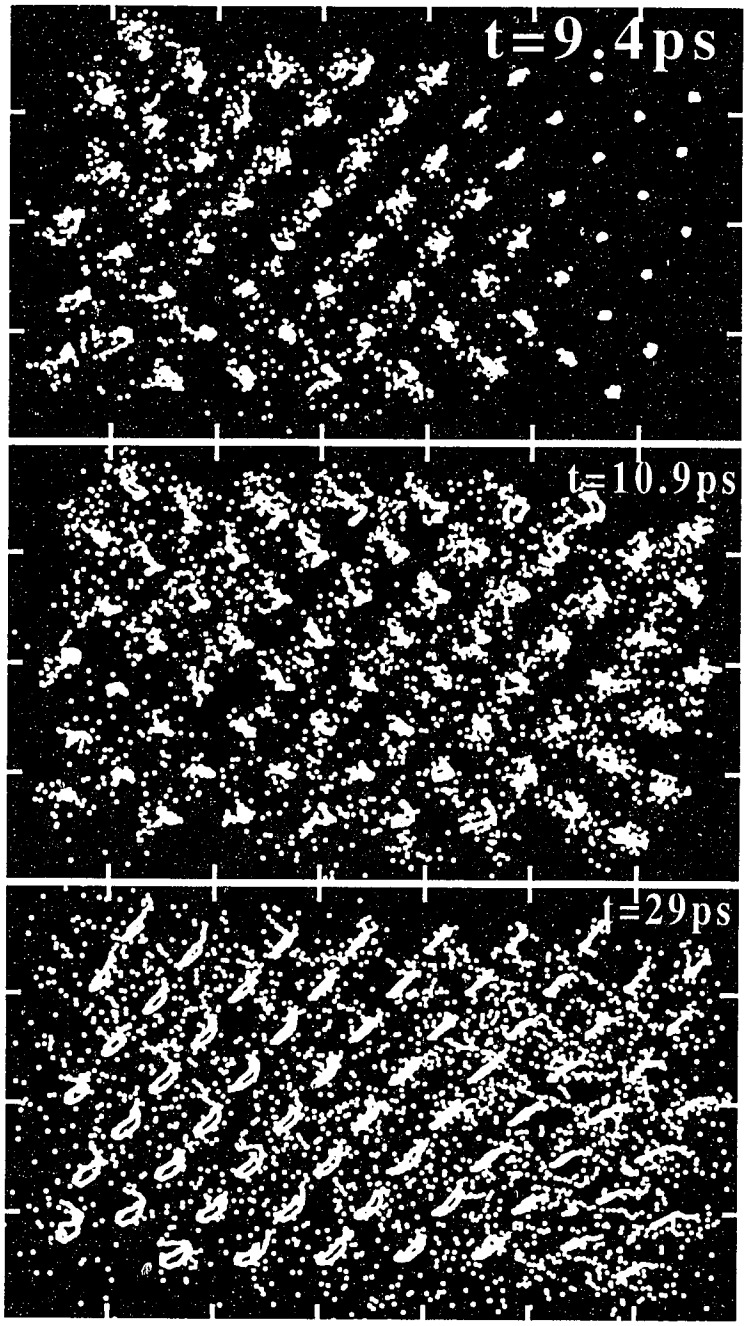

Figure 5.1(d)-(f)

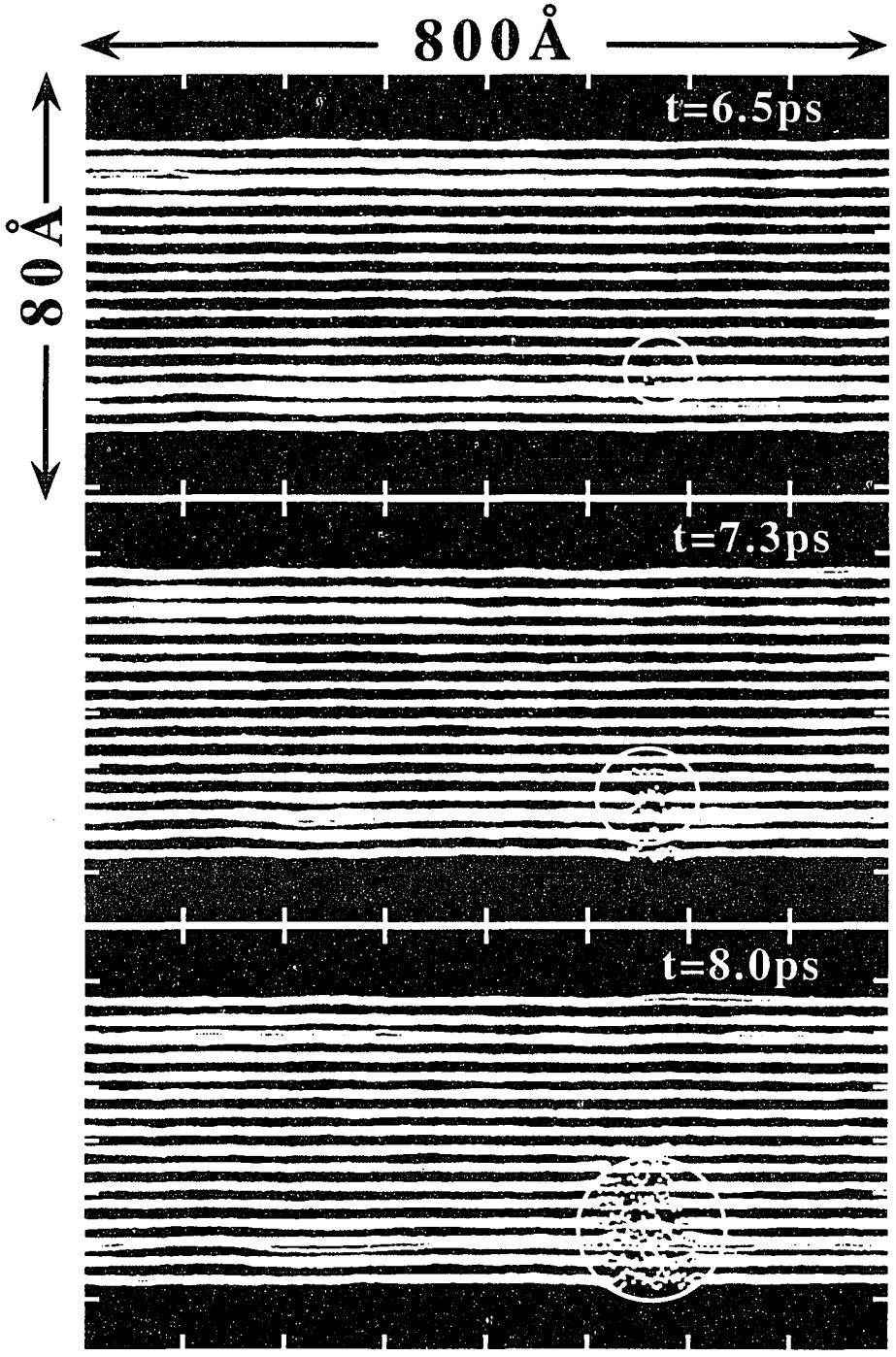

Figure 5.2 Snapshots (a)-(f) of a 64-chain nanowire projected onto the b-c plane. Only Si atoms are shown.

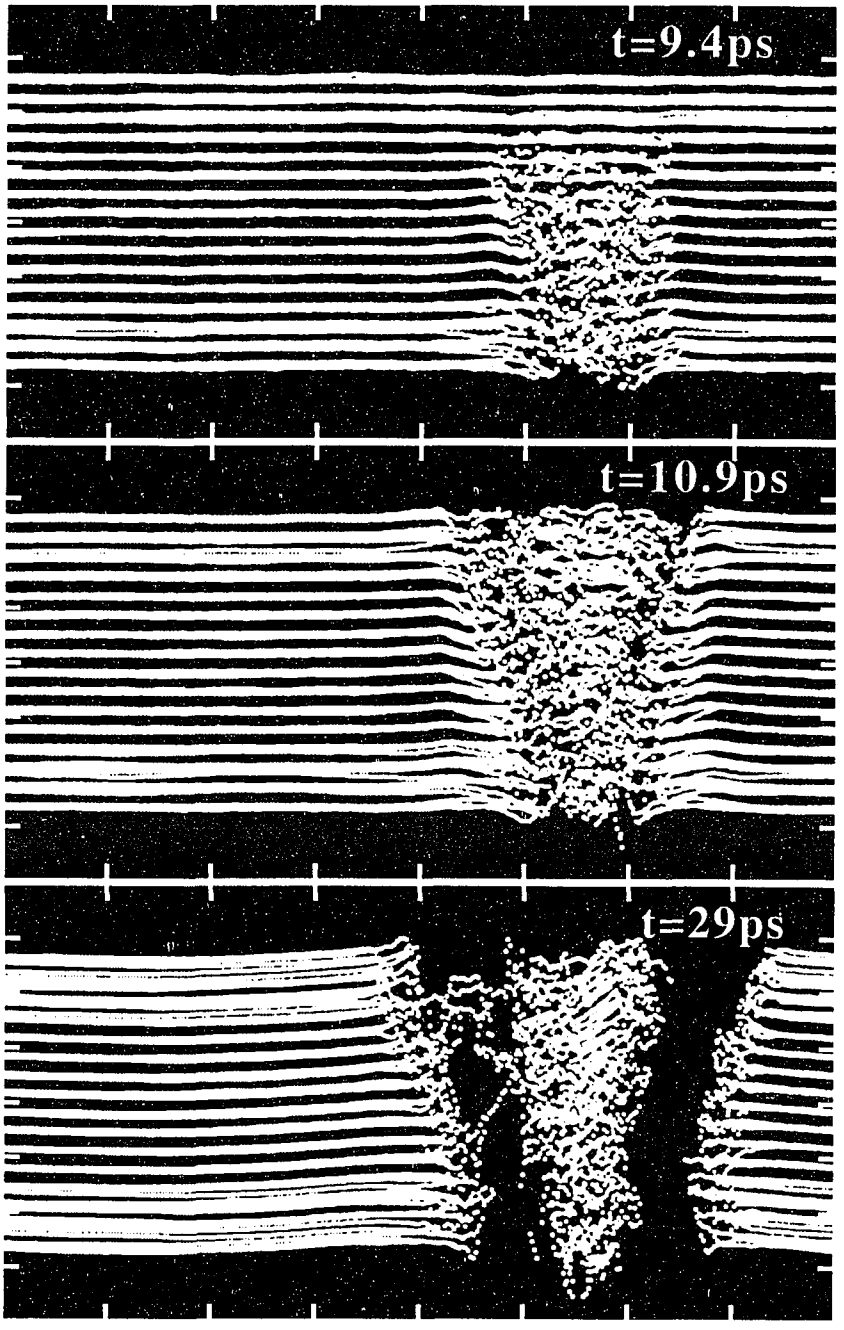

Figure 5.2(d)-(f)

disordered region in the middle. After t=19.6 ps, the nanowire fractures at one of the two boundaries of this region.

5.2 Dynamical Fracture in Nanowires

In order to understand the mechanism of dynamical fracture in $SiSe_2$ nanowires, we have investigated the time evolution of temperature and density. The nanowires are divided into cells of dimensions 10Å × 10Å × 13.5Å, see Figure 5.3(a). There are 4 × 7 cells in the a-b projection, and we label them by their positions: (i, j) (i=1,...,4 and j=1,...,7). Along the c-axis there are 300 cells. The cells with indices (1, 2, k; k=1,...,300) include the site where we first observe the disordered structure. For each cell, we calculate the local "temperature" from the kinetic energy. Figure 5.3(b) shows the "temperature" of the cells with indices (1,2). We find a thermal spike at the site where disordered structure was first observed. The thermal spike is due to the release of energy from broken bonds.

In Chapter 4 we stated that crystalline $SiSe_2$ contains exclusively edge-sharing tetrahedra, and corner-sharing tetrahedra can only be found in molten and glassy states. Here we plot the MD results for bond-angle distributions in crystalline, molten, and glassy $SiSe_2$, see Figure 5.4. In molten and glassy states, the second peaks in the Si-Se-Si bond-angle distribution around 110° arise from corner-sharing tetrahedra. Now let us examine the local bond-angles for a segment of the nanowire near the thermal spike. This segment shown in Figure 5.3(b) is divided into three parts, namely A, B and C. Part B includes the cell with the thermal spike, while parts A and C include several neighboring cells. In Figure 5.5 showing the Si-Se-Si distributions in part B, we observe significant height at large angles due to corner-sharing tetrahedra. These large angles arise when edge-sharing bonds are broken in one of the chains at the outermost layer, see Figure 5.6.

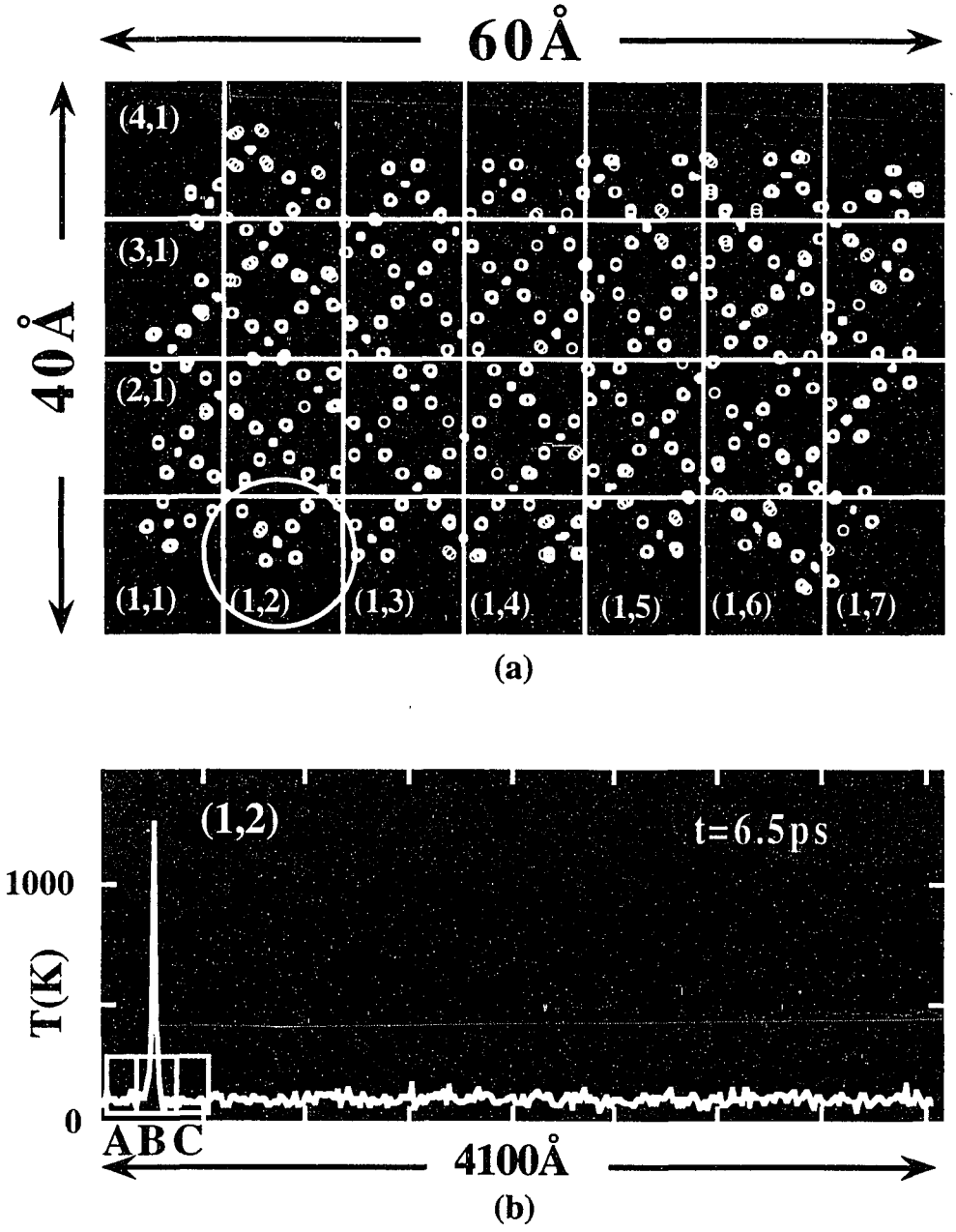

Figure 5.3 (a) Snapshot of a segment of the 64-chain nanowire projected onto the a-b plane showing Si atoms (solid dots) and Se atoms (open dots). The nanowire is divided into 4x7x300 cells. (b) temperature profiles for cells with index (1, 2, k=1, ..., 300).

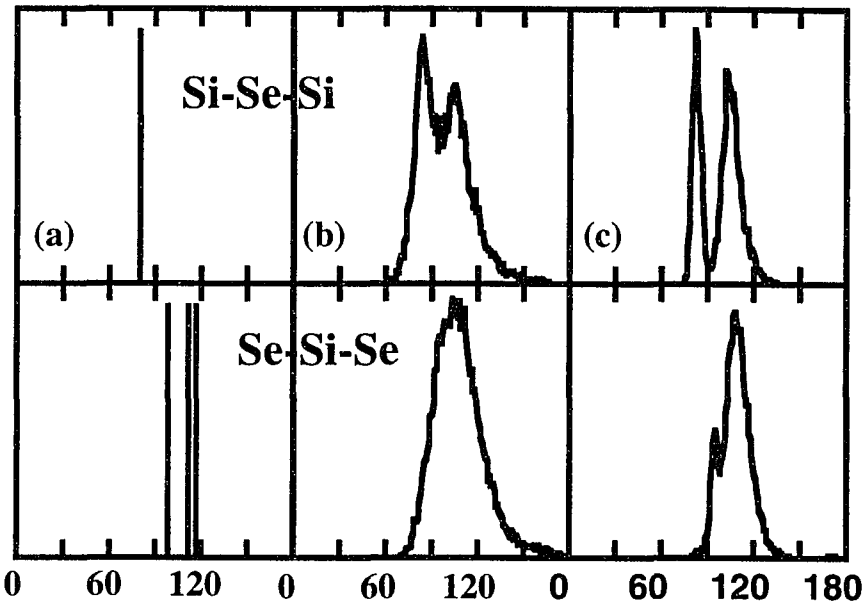

Figure 5.4 Bond-angle distributions for (a) crystalline, (b) molten, and (c) glassy $SiSe_2$.

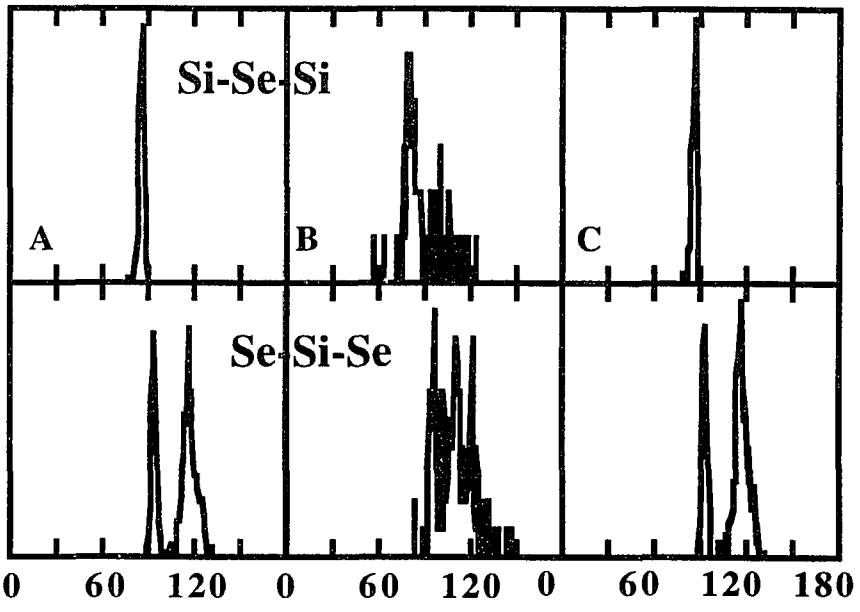

Figure 5.5 Local bond-angle distributions for particles in the three regions A, B, and C of the 64-chain nanowire.

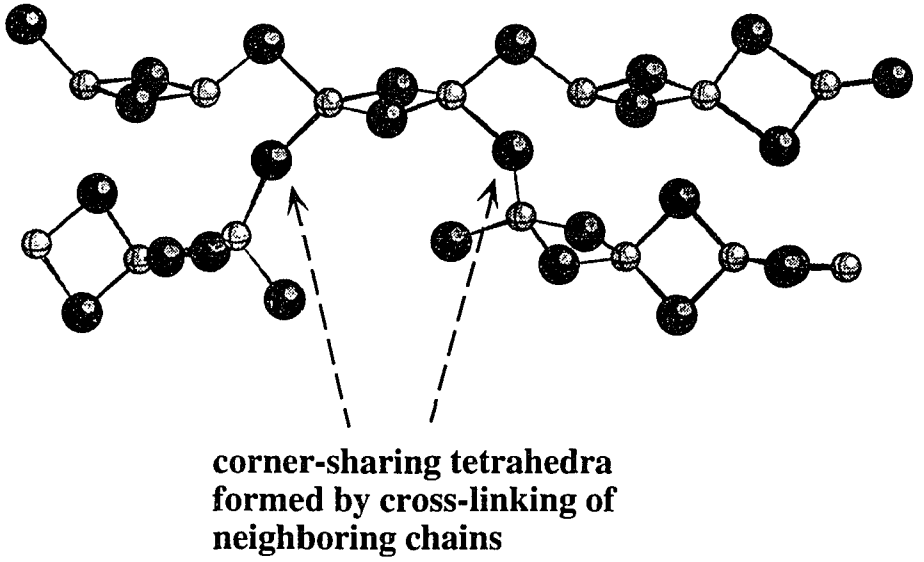

Figure 5.6 Snapshot of a segment from the 64-chain nanowire at t=6.5ps. Arrows indicate the place where edge-sharing bonds break to form corner-sharing tetrahedra by cross-linking with neighboring chains.

Therefore, the disordered structure can be attributed to local amorphization. The rest of the nanowire remains highly crystalline, as evident from the bond-angle distributions in parts A and C.

Figure 5.7 shows temperature profiles of the 64-chain nanowire during the course of local amorphization. (Here, lighter shading represents higher temperature regions.) Evidently, at t=6.5ps, a thermal spike (a narrow line shows in the top figure) appears from the surface of the nanowire. It then propagates across the nanowire while the high-temperature amorphous region expands along the c-direction. In Figure 5.8, we zoom into the local amorphous region to examine the change in "temperature". The nanowire is sliced into blocks of equal thickness of 13.5Å along the c-direction, and the "temperature" is averaged over each block. The x- and y-axes correspond to the time and the c-coordinates along the 64-chain nanowire, respectively. The z-axis represents the average local "temperature". Again, the high "temperature" is denoted by lighter

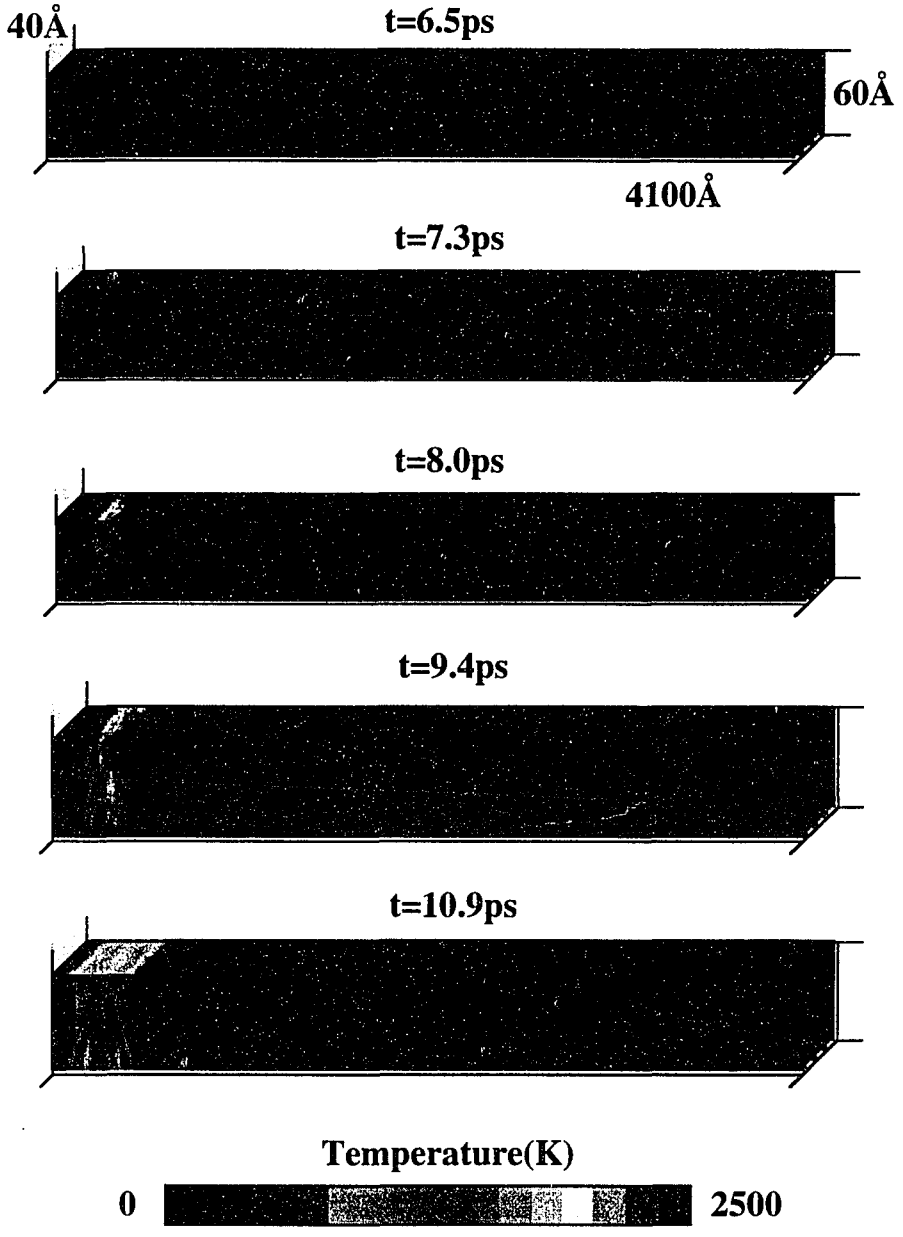

Figure 5.7 Temperature profiles for a 64-chain nanowire. Time is measured from the moment when the critical strain is reached. "Temperature" is estimated from the kinetic energy of each cell.

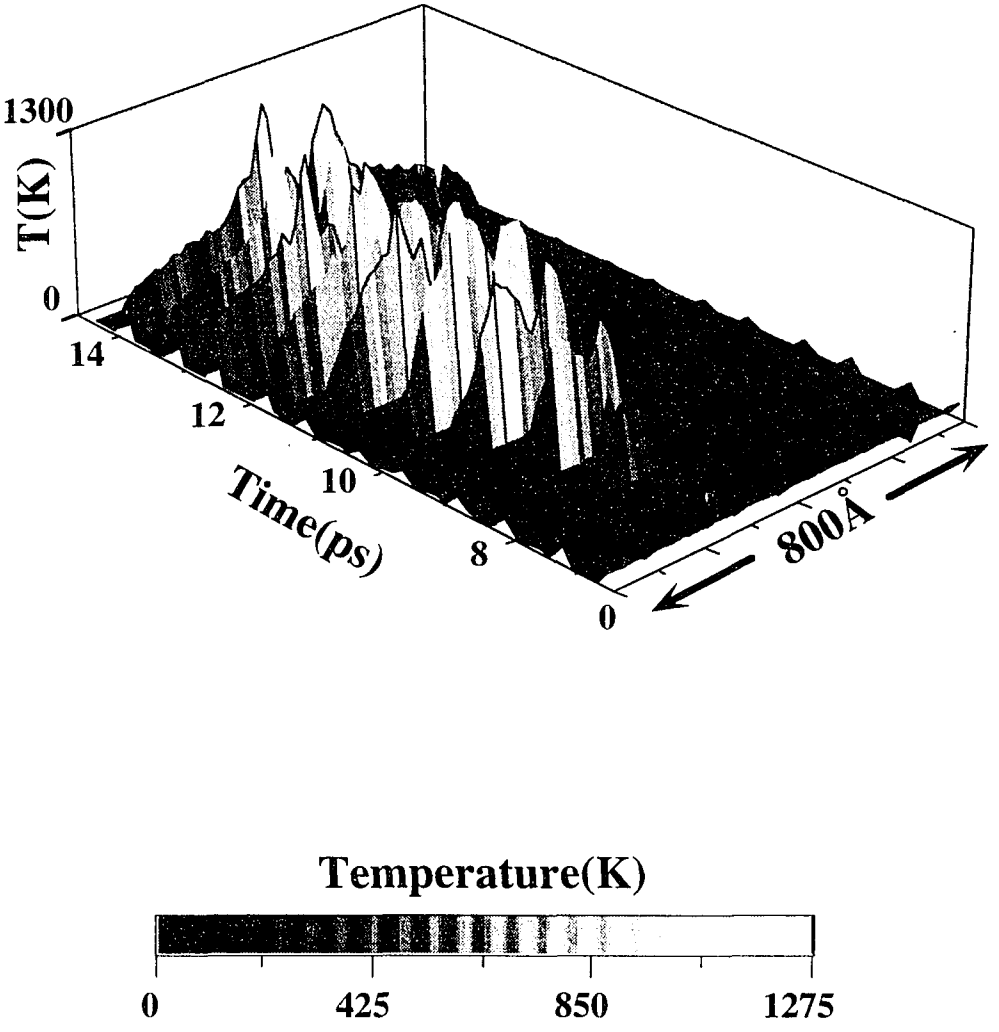

Figure 5.8 Time evolution of temperature profiles for the 64-chain nanowire. Height and shading represent the average "temperature" over each bock along the nanowire. Only one segment of the nanowire is shown.

shading. We have found that the high-temperature region is localized at the fracture site. As time evolves, this region expands along the nanowire and the temperature increases. From the local bond-angle distribution, we find that up to about 10ps the nanowire in the high-temperature region is in an amorphous state. The rest of the nanowire remains crystalline. We can estimate the speed of propagation of the thermal spike along the c-direction and perpendicular to c-axis. We have found that the longitudinal speed is v_L=2.7±0.5 km/s and the transversal speed is v_T=1.1±0.5 km/s.

We have examined the local density of each individual cell as well as each block at different time intervals. Figure 5.9 shows the time evolution of the local density. Here darker colors represent regions of lower density. We define a crack when the local density in a cell becomes zero. It is observed that up to about 10 ps, there is no crack in the nanowire. At t=10.9ps, we observe several dark sections in the high-temperature regions. This means that many cracks nucleate around nanowires, and all of them are at the boundaries of the amorphous region. These cracks propagate inward from the surface layer until the nanowire fractures. Again in Figure 5.10 we zoom into the amorphous region. Here the z-axis represents the local density averaged over each block. The x- and y-axes correspond to the time and the c-coordinate along the 64-chain nanowire, respectively. At t=10ps, we observe a drop in the local density at the two boundaries. The local density vanishes at the boundaries when the nanowire completely fractures at t=19.6ps.

Amorphization and fracture have also been observed in MD simulations for nanowires with 16 and 32 chains. Thinner nanowires (with number of chains < 16) undergo mechanical failure when all of the chains break within a short time (< 1ps).

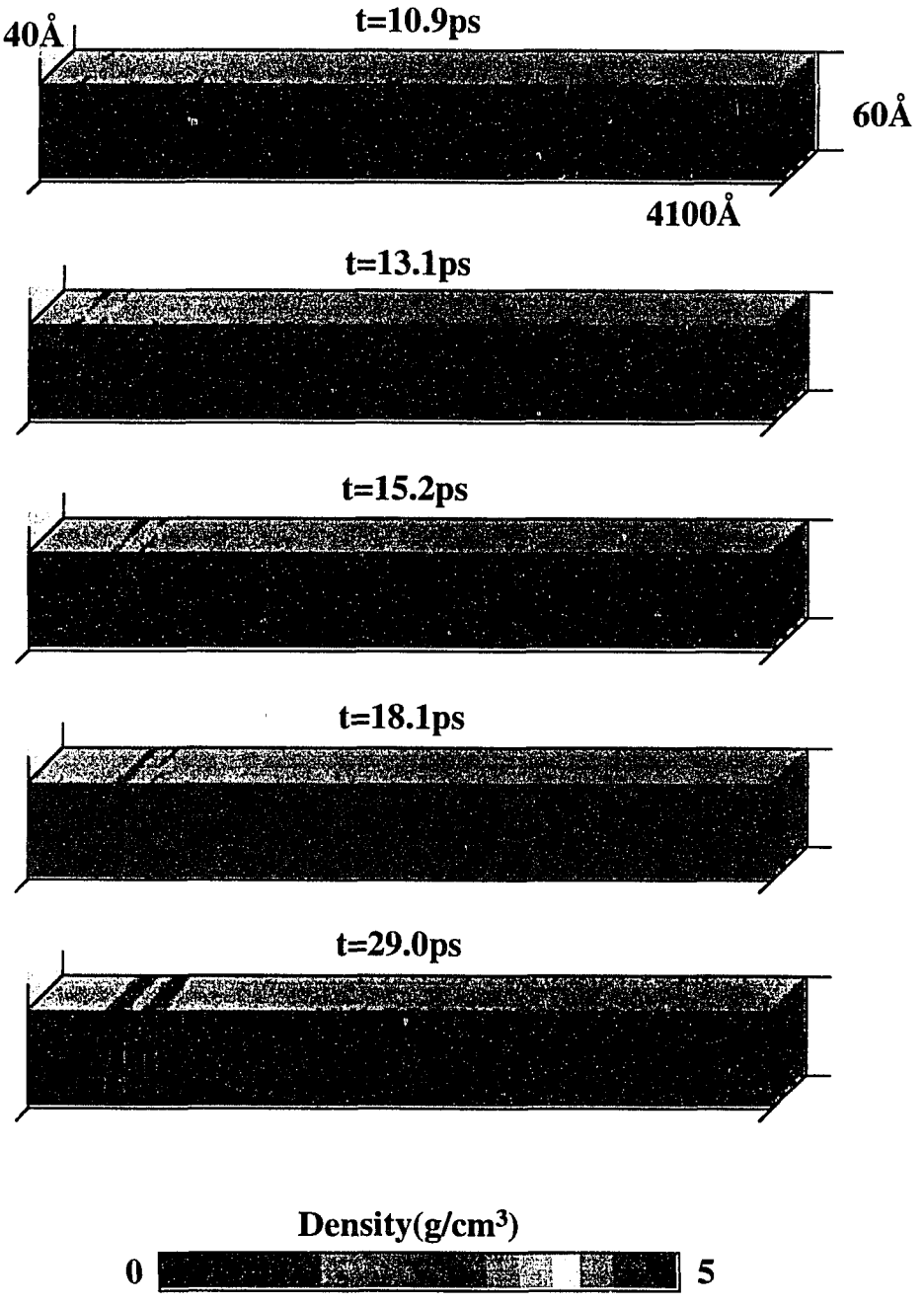

Figure 5.9 Mass density profiles for the 64-chain nanowire.

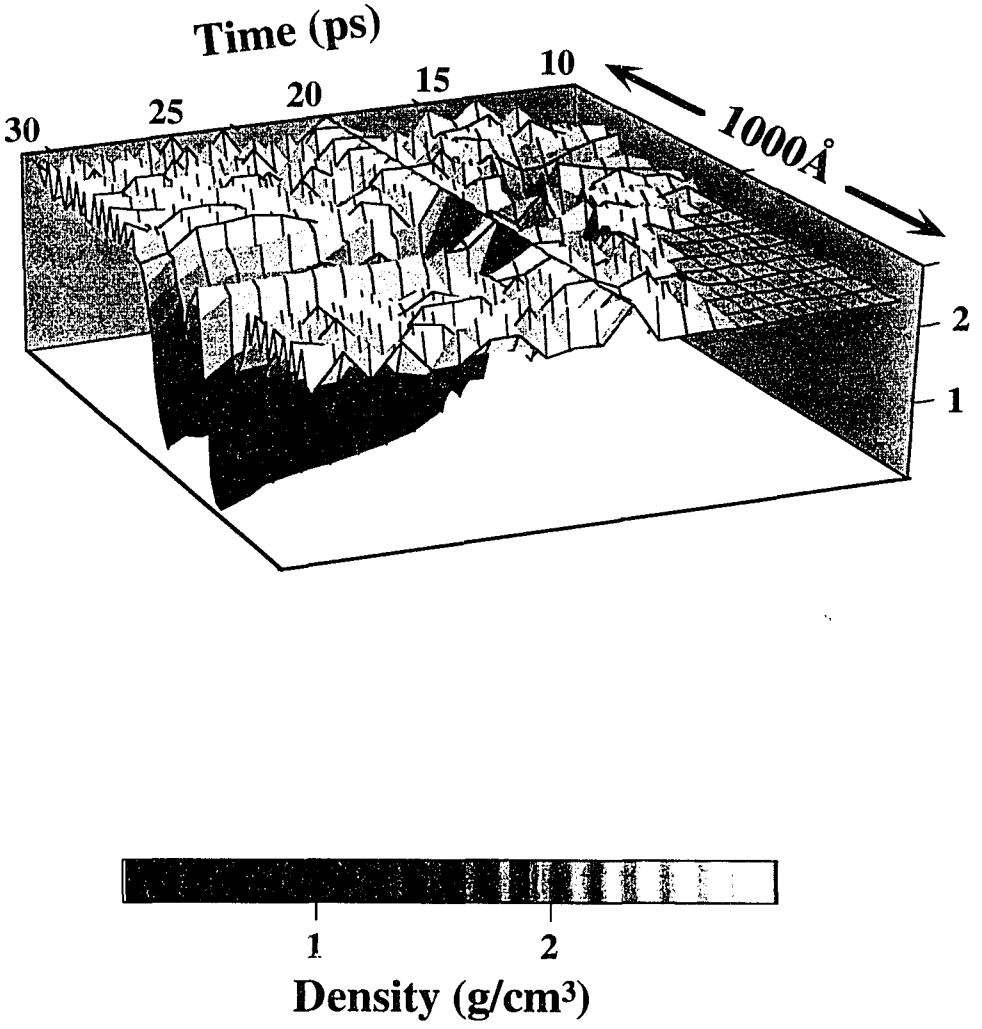

Figure 5.10 Time evolution of the mass density profile for the 64-chain nanowire. Height and color represent average density over each block along the nanowire. Only a segment of the nanowire is shown.

CHAPTER 6

CONCLUSION

6.1 Summary

In this dissertation, we have presented the molecular-dynamics (MD) simulation results for the implementation of the Fast Multipole Method on distributed memory MIMD machines, investigation of structural and mechanical properties of $SiSe_2$ nanowires under small uniaxial strain, and amorphization and fracture in $SiSe_2$ nanowires under large uniaxial strain. This is the first study of crack initiation and propagation in $SiSe_2$ nanowires, and most importantly, the first observation of the phenomena of local amorphization in materials prior to fracture.

We have developed a parallel algorithm for the Fast Multipole Method. The performance of the algorithm has been tested on the in-house 8-node Intel iPSC/i860 machine and the 512-node Touchstone Delta machine at Caltech. This algorithm reduces the overall computational complexity from $O(N^2)$ to $O(N)$.

Structural and mechanical properties of $SiSe_2$ nanowires under uniaxial strain are studied with the MD simulation technique. The nanowires contain a finite number (1-64) of chains with edge-sharing tetrahedra. The calculations are based on an effective potential consisting two- and three-body terms. With this potential we have obtained a melting temperature for bulk $SiSe_2$ that agrees very well with experimental result. Our results for the static structure factor are also in good agreement with neutron-diffraction experiments for glassy $SiSe_2$.

We have investigated structural correlations in $SiSe_2$ nanowires. Under a small uniaxial strain along the chain direction (the c-axis), the nanowires develop wiggles even though they remain crystalline. We observe the response of internal energy of the

nanowires on the external strain. The force constants for nanowires scale linearly with number of chains in the nanowires. This is an indication that the intra-chain interaction is responsible for the macroscopic mechanical behavior of nanowires. The Young's modulus of nanowires is estimated to be 100-130Gpa.

We have also investigated the dynamics of amorphization and fracture in $SiSe_2$ nanowires under large uniaxial strain. It is found that the critical strain of fracture is independent of the number of chains in the nanowires. Temperature and density profiles, and local bond-angle distributions are examined. The simulation results reveal that fracture in $SiSe_2$ nanowires is preceded by amorphization. At first, edge-sharing bonds break in the chains at the outermost layer. These broken chains then form corner-sharing tetrahedra by cross-linking with neighboring chain. Local amorphization propagates across nanowires to form a sandwich-like structure with an amorphous region in the middle. Cracks are then nucleated at the boundaries of the amorphous region. These cracks propagate inward from the nanowire surface.

The MD simulations for $SiSe_2$ nanowires were performed on the 40-node Digital Alpha system based on two Gigaswitches in the Concurrent Computing Laboratory for Materials Simulations (CCLMS) at LSU.

6.2 Future Work

• Internal Stress Analysis

To gain further insight into the microscopics of local amorphization in $SiSe_2$ nanowires and understand the underlying mechanism, we intend to do the local stress distribution analysis for nanowires subject to different strains. The internal stress can be calculated using the well-known virial expression Eq.(2.19) or a mechanical approach suggested by Yip [41]. For nanowires in thermal equilibrium, the internal stress should be uniformly distributed along the c-axis. However, when nanowires are subjected to

large strain, we expect the local instability to manifest through the internal stress distribution. This may be the cause for local amorphization.

• Simulation of Nanowires Containing Multimillion Particles

In the present work, the cross-section of nanowires is < 100Å. This is relatively small for the characterization of crack propagation. It is necessary to perform multimillion atom MD simulations for nanowires with a diameter exceeding 200Å. These nanowires will contain up to 1,024 chains. We plan to calculate the crack propagation speed and determine the morphology of the fractured surface. In addition, the experiences of simulating $SiSe_2$ nanowires can be extended to simulate ceramic nanowires such as Si_3N_4 nanowires and SiC nanowires.

REFERENCES

1. L.B. Freund, *Dynamics Fracture Mechanics*l, (Cambridge University Press, Cambridge, New York, Port Chester, Melbourne, Sydney, 1990).

2. M. Marder, Phys. Rev. Lett., **66**, 2484 (1991).

3. M. Marder and X. Liu, Phys. Rev. Lett., **71**, 2417 (1993).

4. M. Marder and S. Gross, J. the Mechanics and Physics of Solids, **43**, 1 (1995).

5. E. Kaxiras and M.S. Duesbery, Phys. Rev. Lett., **70**, 3752 (1993).

6. Y.-m. Juan, Y. Sun and E. Kaxiras, Phil. Mag. Lett., **in press**, (1996).

7. E. Bouchaud and J.-P. Bouchaud, Phys. Rev., **B50**, 17752 (1994).

8. E. Bouchaud and S. Navéos, J. Phys. I France, **5**, 547 (1995).

9. P. Daguier, E. Bouchaud and G. Lapasset, Europhys. Lett., **31**, 367 (1995).

10. E. Sharon, S.P. Gross and J. Fineberg, Phys. Rev. Lett., **74**, 5096 (1995).

11. K.J. Måløy, A. Hansen, E.L. Hinrichsen and S. Roux, Phys. Rev. Lett., **68**, 213 (1992).

12. N. Binggeli, J.R. Chelikowsky and R.M. Wentzcovitch, Phys. Rev., **B49**, 9336 (1994).

13. N. Binggeli, N.R. Keskar and J.R. Chelikowsky, Phys. Rev., **B49**, 3075 (1994).

14. M.B. Kruger and R. Jeanloz, Science, **249**, 647 (1990).

15. L.E. McNeil and M. Grimsditch, Phys. Rev. Lett., **68**, 83 (1992).

16. K.J. Kingma, R.J. Hemley, H.-k. Mao and D.R. Veblen, Phys. Rev. Lett., **70**, 3927 (1993).

17. J.S. Tse and D.D. Klug, Phys. Rev. Lett., **67**, 3559 (1991).

18. J.S. Tse and D.D. Klug, Science, **255**, 1559 (1992).

19. J.S. Tse and D.D. Klug, Phys. Rev. Lett., **70**, 174 (1993).

20. S.L. Chaplot and S.K. Sikka, Phys. Rev., **B47**, 5710 (1993).

21. R.G. Hoagland, M.S. Daw and J.P. Hirth, J. Mater. Res., **6**, 2565 (1991).

22. G.J. Dienes and A. Paskin, in *Atomistics of Fracture* R.M. Latanision and J.R. Pickens, Eds. (Plenum Press, New York, 1983) pp. 671.

23. V. Vitek, Materials Science and Engineering, **94**, 5 (1987).

24. R.W. Smith and D.J. Srolovitz, Modelling and Simulation in Materials Science and Engineering, **2**, 1153 (1994).

25. G. Ciccotti and W.G. Hoover, in International School of Physics, Course XCVII (1985),

26. M.P. Allen and D.J. Tildesley, *Computer Simulation of Liquids*l, (Clarendon Press, Oxford, 1987).

27. H. Gould and J. Tobochnik, *An Introduction to Computer Simulation Methods: Applications to Physical Systems*l, (Addison-Wesley, Reading, MA, 1987), vol. Part 1 and 2.

28. S. Nosé, J. Chem. Phys., **81**, 511 (1984).

29. S. Nosé, Molecular Physics, **52**, 255 (1984).

30. S. Nosé and M.L. Klein, Molecular Physics, **50**, 1055 (1983).

31. S. Nosé and M.L. Klein, J. Chem. Phys., **78**, 6928 (1983).

32. S. Nosé and M.L. Klein, Phys. Rev. Lett., **50**, 1207 (1983).

33. H.C. Andersen, J. Chem. Phys., **72**, 279 (1980).

34. J.M. Haile and H.W. Graben, J. Chem. Phys., **73**, 2412 (1980).

35. M. Parrinello and A. Rahman, J. Appl. Phys, **52**, 7182 (1981).

36. W.T. Ashurst and W.G. Hoover, Phys. Rev., **B14**, 1465 (1976).

37. K. Sieradzki, G.J. Dienes, A. Paskin and B. Massoumzadeh, Acta Metallurgica, **36**, 651 (1988).

38. K. Sieradzki and R. Li, Phys. Rev. Lett., **67**, 3042 (1991).

39. T.F. Soules and R.F. Busbey, J. Chem. Phys., **78**, 6307 (1983).

40. J. Kieffer and C.A. Angell, J. Non-Crystalline Solids, **106**, 336 (1988).

41. K.S. Cheung and S. Yip, Phys. Rev. Lett., **65**, 2804 (1990).

42. R. Ochoa, T.P. Swiler and J.H. Simmons, J. Non-Crystalline Solids, **128**, 57 (1991).

43. F.F. Abraham, D. Brodbeck, R.A. Rafey and W.E. Rudge, Phys. Rev. Lett.,

73, 272 (1994).

44. J. Belak, D.B. Boercker and I.F. Stowers, MRS Bulletin, **XVIII**, 55 (1993).

45. P. Vashishta, R.K. Kalia, S.W.d. Leeuw, D.L. Greenwell, A. Nakano, W. Jin, J. Yu, L. Bi and W. Li, Computational Materials Science, **2**, 180 (1994).

46. R.K. Kalia, A. Nakano, D.L. Greenwell and P. Vashishta, Supercomputer 54, **X**, 11 (1993).

47. B.L. Holian and D.E. Grady, Phys. Rev. Lett., **60**, 1355 (1988).

48. B.L. Holian, A.F. Voter, N.J. Wagner, R.J. Ravelo, S.P. Chen, W.G. Hoover, C.G. Hoover, J.E. Hammerberg and T.D. Dontje, Phys. Rev., **A43**, 2655 (1991).

49. B.L. Holian and R. Ravelo, Phys. Rev., **B51**, 11275 (1995).

50. A. Nakano, R.K. Kalia and P. Vashishta, Phys. Rev. Lett., **75**, 3138 (1995).

51. L. Greengard and V. Rokhlin, J. Computational Physics, **73**, 523 (1987).

52. C. Guerret-Piecourt, Y.L. Bouar, A. Loiseau and H. Pascard, Nature, **372**, 761 (1994).

53. T.M. Whitney, J.S. Jiang, P.C. Searson and C.L. Chien, Science, **261**, 1316 (1993).

54. C.M. Knoedler, J. Appl. Phys., **68**, 1129 (1990).

55. A. Agraït, G. Rubio and S. Vieira, Phys. Rev. Lett., **74**, 3995 (1995).

56. L. Brus, J. Phys. Chem., **98**, 3575 (1994).

57. J. Peters and B. Krebs, Acta Cryst., **B38**, 1270 (1982).

58. S. Susman, R.W. Johnson, D.L. Price and K.J. Volin, in Defects in Glasses, F.L. Galeener, D.L. Griscom and M.J. Webers, Eds., Mat. Res. Soc. Symp. Proc. (1986), vol. 61, pp. 91.

59. M. Tenhover, M.A. Hazle and R.K. Grasselli, Phys. Rev. Lett., **51**, 404 (1983).

60. M. Tenhover, M.A. Hazle, R.K. Grasselli and C.W. Tompson, Phys. Rev., **B28**, 4608 (1983).

61. M. Tenhover, R.S. Henderson, D. Lukco, M.A. Hazle and R.K. Grasselli, Solid State Communications, **51**, 455 (1984).

62. M. Tenhover, R.D. Boyer, R.S. Henderson, T.E. Hammond and G.A. Shreve, Solid State Communications, **65**, 1517 (1988).

63. J.E. Griffiths, M. Malyj, G.P. Espinosa and J.P. Remeika, Phys. Rev., **B30**, 6978 (1984).

64. R.W. Johnson, S. Susman and D.L. Price, J. Non-Crystalline Solids, **75**, 57 (1985).

65. R.W. Johnson, D.L. Price, S. Susman, M. Arai, T.I. Morrison and G.K. Shenoy, J. Non-Crystalline Solids, **83**, 251 (1986).

66. R.W. Johnson, J. Non-Crystalline Solids, **88**, 366 (1986).

67. R.W. Johnson, S. Susman, J. McMillan and K.J. Volin, Mat. Res. Bull., **21**, 41 (1986).

68. S. Susman, D.L. Price, K.J. Volin, R.J. Dejus and D.G. Montague, J. Non-Crystalline Solids, **106**, 26 (1988).

69. M. Arai, D.L. Price, S. Susman, K.J. Volin and U. Walter, Phys. Rev., **B**, (1987).

70. S. Sugai, Phys. Rev. Lett., **57**, 456 (1986).

71. S. Sugai, Phys. Rev., **B35**, 1345 (1987).

72. L.F. Gladden and S.R. Elliott, J. Non-Crystalline Solids, **109**, 211 (1989).

73. L.F. Gladden and S.R. Elliott, J. Non-Crystalline Solids, **109**, 223 (1989).

74. L.F. Gladden, J. Non-Crystalline Solids, **123**, 22 (1990).

75. G.A. Antonio, R.K. Kalia and P. Vashishta, J. Non-Crystalline Solidds, **106**, 305 (1988).

76. G.A. Antonio, R.K. Kalia and P. Vashishta, Solid State Ionics, **32/33**, 950 (1989).

77. G.A. Antonio, R.K. Kalia, A. Nakano and P. Vashishta, Phys. Rev., **B45**, 7455 (1992).

78. R. Bhadra, S. Susman, K.J. Volin and M. Grimsditch, Phys. Rev., **B39**, 1378 (1989).

79. M.S. Chandrasekharaiah and J.L. Margrave, J. Phys. Chem. Ref. Data, **23**, 499 (1994).

80. I. Tomaszkiewicz, S. Susman, K.J. Volin and P.A.G. O'Hare, J. Chem. Thermodynamics, **26**, 1081 (1994).

81. A. Pradel, V. Michel-Lledos, M. Ribes and H. Eckert, Chem. Mater., **5**, 377 (1993).

82. M. Parrinello and A. Rahman, J. Chem. Phys., **76**, 2662 (1982).

83. J.R. Ray and H.W. Graben, Molecular Physics, **43**, 1293 (1981).

84. J.R. Ray, J. Appl. Phys., **53**, 6441 (1982).

85. J.R. Ray and A. Rahman, J. Chem. Phys., **80**, 4423 (1984).

86. J.R. Ray and A. Rahman, J. Chem. Phys., **82**, 4243 (1985).

87. J.R. Ray, M.C. Moody and A. Rahman, Phys. Rev., **B32**, 733 (1985).

88. J.R. Ray, M.C. Moody and A. Rahman, Phys. Rev., **B33**, 895 (1986).

89. J.R. Ray, Computer Physics Reports, **8**, 109 (1988).

90. M. Tuckerman and B.J. Berne, J. Chem. Phys., **97**, 1990 (1992).

91. L. Verlet, Phys. Rev., **159**, 98 (1967).

92. F.H. Stillinger and T.A. Weber, Phys. Rev., **A28**, 2408 (1983).

93. W. Li, R.K. Kalia and P. Vashishta, in *Solid State Ionics III*, G.-A. Nazri, J.-M. Tarascon and M. Armands, Eds., Mat. Res. Soc. Symp. Proc. (1992), vol. 293, pp. 256.

94. A. Nakano, L. Bi, R.K. Kalia and P. Vashishta, Phys. Rev., **B49**, 9441 (1994).

95. A. Nakano, P. Vashishta and R.K. Kalia, Computer Physics Communications, **77**, 303 (1993).

96. P. Vashishta, R.K. Kalia, J.P. Rino and I. Ebbsjo, Phys. Rev., **B41**, 12197 (1990).

97. J.L. Lebowitz, J.K. Percus and L. Verlet, Phys. Rev., **153**, 250 (1967).

98. S.W.d. Leeuw, J.W. Perram and E.R. Smith, Proc. R. Soc. London, **A373**, (1980).

99. R.K. Kalia, S.d. Leeuw, A. Nakano and P. Vashishta, Computer Physics Communications, **74**, 316 (1993).

100. A.W. Appel, SIAM J. Sci.Stat. Comput, **6**, 85 (1985).

101. J. Barnes and P. Hut, Nature, **324**, 446 (1986).

102. G.C. Fox, P. Hipes and J. Salmon, in I.C.S.a.A. SIGARCHs, Eds., Supercomputing '89 (1989), pp. 58.

103. M. Warren and J. Salmon, CSCC Update, **13**, 1 (1992).

104. L. Greengard, *The Rapid Evaluation of Potential Fields in Particle Systems*l, (The MIT Press, Cambridge, Massachusetts, London, England, 1987).

105. L. Greengard and W.D. Gropp, in G. Rodrigues, Eds., Parallel Processing for Scientific Computing (1989),

106. L. Greengard, Computers in Physics, **4**, 142 (1990).

107. K.E. Schmidt and M.A. Lee, J. Statistical Physics, **63**, 1223 (1991).

108. F. Zhao and S.L. Johnsson, SIAM J. Sci. Stat. Comput, **12**, 1420 (1991).

109. M.A. Epton and B. Dembart, SIAM J. Sci. Comput., **16**, 865 (1994).

110. H.G. Petersen, D. Soelvason and J.W. Perram, J. Chem. Phys., **101**, 8870 (1994).

111. H.G. Petersen, E.R. Smith and D. Soelvason, Proc. R. Soc. Lond., **A448**, 401 (1995).

112. A. Nakano, R.K. Kalia and P. Vashishta, Computer Physics Communication, **83**, 197 (1994).

113. R.K. Kalia, W. Jin, S.W.D. Leeuw, A. Nakano and P. Vashishta, International Journal of Quantum Chemistry: Quantum Chemistry Symposium, **27**, 781 (1993).

114. H.-Q. Ding, N. Karasawa and I. William A. Goddard, J. Chem. Phys., **97**, 4309 (1992).

115. H.-Q. Ding, N. Karasawa and W.A.G. III, Chem. Phys. Lett., **196**, 6(1992).

116. W. Li, R.K. Kalia, S.d. Leeuw, A. Nakano, D. Greenwell and P. Vashishta, in *Materials Theory and Modeling*, P.D. Bristowe, J. Broughton and J.M. Newsams, Eds., Mat. Res. Soc. Symp. Proc. (1992),

117. C.A. White and M. Head-Gordon, J. Chem. Phys., **101**, 6593 (1994).

118. P. Vashishta, R.K. Kalia, G.A. Antonio, J.P. Rino, H. Iyetomi and I. Ebbsjo, Solid State Ionics, **40/41**, 175 (1990).

119. A. Nakano, L. Bi, R.K. Kalia and P. Vashishta, Phys. Rev. Lett., **71**, 85 (1993).

120. W. Jin, R.K. Kalia, P. Vashishta and J.P. Rino, Phys. Rev. Lett., **71**, 3146 (1993).

121. W. Jin, P. Vashishta, R.K. Kalia and J.P. Rino, Phys. Rev., **B48**, 9359 (1993).

122. C.-K. Loong, P. Vashishta, R.K. Kalia and I. Ebbsjö, Europhys. Lett., **31**, 201 (1995).

123. W.H. Press, S.A. Teukolsky, W.T. Vetterling and B.P. Flannery, *Numerical Recipes in FORTRAN*l, (Cambridge University Press, Cambridge, 1992).

124. W. Li, R.K. Kalia and P. Vashishta, in *Materials Theory, Simulations and Parallel Algorithms*, E. Kaxiras, J. Joannopoulos, P. Vashishta and R.K. Kalias, Eds., Mat. Res. Soc. Symp. Proc. (1996), vol. 408,

125. W. Li, R.K. Kalia and P. Vashishta, Europhysics Lett., (1996) inpress.

126. L.D. Landau and E.M. Lifshitz, *Theory of Elasticity*l, (Pergamon Press, 1986).

127. R. Sedgewick, in *Algorithms in C* (Addison-Wesley, Reading, MA, 1990) pp. 359.

128. G. Bergerhoff, B. Kilger, C. Witthauer, R. Hundt and R. Sievers, ICSD - CRYSTIN: Inorganic Crystal Structure Database/Crystal Structure Information System, (Institut Fuer Anorganische Chemie der Universitaet, 1986)

129. P.A. Tipler, *Physics for Scientists and Engineers*l, (Worth Publishers, 1991).

APPENDIX A

COMPUTER FACILITIES IN CCLMS

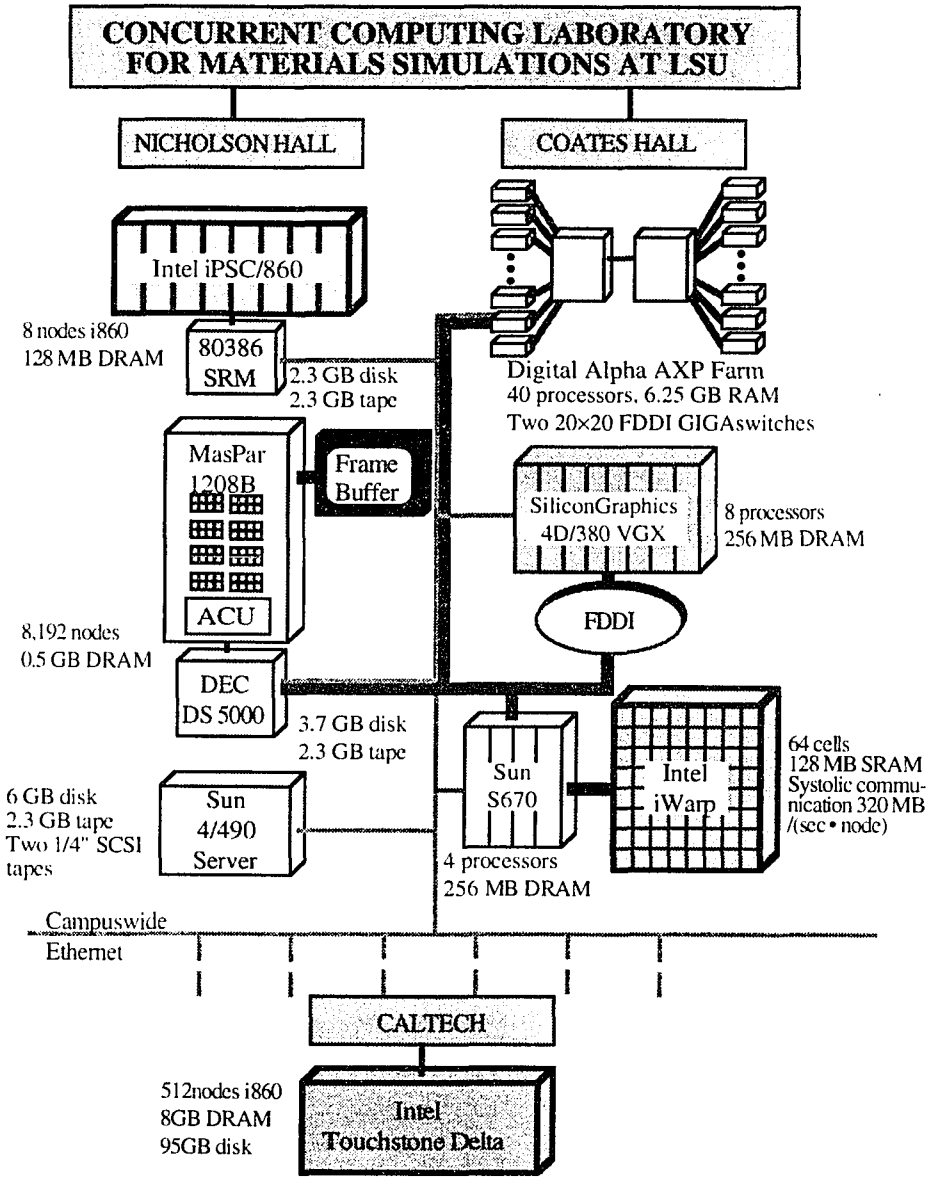

Figure A.1 Computer facilities in Concurrent Computing Laboratory for Materials Simulations at Louisiana State University.

APPENDIX B

CONJUGATE GRADIENT METHOD

In MD simulations, stable configurations of the particle systems are determined by a minimum energy condition of the atomic arrangements. To do this, we apply conjugate gradient (CG) approach.

In the CG algorithm, the total potential energy $\mathcal{V}(\{\vec{r}_i\})$ is expressed as a function of particle coordinates $\{\vec{r}_i\}$ with i=1, 2, ..., N. Starting from a given MD configuration $\{\vec{r}_i^{(0)}\}$, refined configurations $\{\vec{r}_i^{(n)}\}$ are generated iteratively as follows:

(i) Calculate the gradient $\vec{g}_i^{(n)}$ for the *i* th particle at the *n* th iteration according to

$$\vec{g}_i^{(n)} = -\frac{\partial \mathcal{V}}{\partial \vec{r}_i^{(n)}}. \tag{B.1}$$

(ii) Calculate the conjugate-gradient direction $\vec{h}_i^{(n)}$ as

$$\vec{h}_i^{(n)} = \begin{cases} \vec{g}_i^{(n)} + \gamma_{n-1}\vec{h}_i^{(n-1)} & (n \geq 1) \\ \vec{g}_i^{(0)} & (n = 0) \end{cases} \tag{B.2}$$

where

$$\gamma_{n-1} = \frac{\sum_{i=1}^{N} [(\vec{g}_i^{(n)} - \vec{g}_i^{(n-1)}) \cdot \vec{g}_i^{(n)}]}{\sum_{i=1}^{N} |\vec{g}_i^{(n-1)}|^2}. \tag{B.3}$$

(iii) Minimize the potential energy along the conjugate-gradient direction, i.e., find $\lambda = \lambda_{min}$ which minimizes $\mathcal{V}(\{\vec{r}_i^{(n)} + \lambda\vec{h}_i^{(n)}\})$. The refined configuration is then given by $\vec{r}_i^{(n+1)} = \vec{r}_i^{(n)} + \lambda_{min}\vec{h}_i^{(n)}$.

Structural and mechanical properties are usually examined for these relaxed configurations. Density of states are also evaluated based on these 'ground states'.

VITA

Wei Li was born on September 27, 1961 in Beijing, China, to Weigan Li and Weiling Chen. She attended the Second Ding Fuzhuang Highschool in Beijing.

She studied in Beijing University in China from 1979 to 1983, and graduated with a bachelor of science degree in Electrical Engineering.

In 1983 she began her graduate study in the Institute of Biophysics of the Chinese Academy of Sciences. She received her master's degree in Biophysics in 1986.

She joined the Institute of Psychology of the Chinese Academy of Sciences from 1986 to 1989 and worked there as an research assistant professor.

Wei Li started her doctoral program with the Department of Physics and Astronomy at Louisiana State University in 1989. She is currently involved in the Concurrent Computing Laboratory for Materials Simulations at LSU as a candidate for the degree of Doctor of Philosophy. Her advisors are Drs. Rajiv. K Kalia and Priya Vashishta.

DOCTORAL EXAMINATION AND DISSERTATION REPORT

Candidate:
Wei Li

Major Field:
Physics

Title of Dissertation:
Amorphization and Fracture in $SiSe_2$ Nanowires: Molecular-Dynamics Simulations on Parallel Computers Architectures

Approved:

Priya Vashishta
Major Professor and Chairman

Dean of the Graduate School

EXAMINING COMMITTEE:

Rajiv K. Kalia

Fuchs Abe

J. C. Phillips

John M. Tyler

Alex Travesset

Date of Examination:

March 8, 1996